LUND UNIVERSITY

Single-Electron Tunneling Spectroscopy in Magnetic Nanoparticles and Molecular Magnets

Michalak, Lukasz

2010

Single-Electron Tunneling Spectroscopy in Magnetic Nanoparticles and Molecular Magnets

ŁUKASZ MICHALAK

LUNDS UNIVERSITET

Division of Solid State Physics
Lund Institute of Technology
LUND UNIVERSITY
Lund, Sweden 2010

ISBN 978-91-7473-071-5
Printed in Sweden by Media-Tryck, Lund 2010

Rodzicom (to my Parents)

Abstract

This thesis deals with single-electron tunneling in transistor-like devices in which the central electrode is either a metal nanoparticle (possibly ferromagnetic) or a molecular magnet. The investigated systems split into two different categories, depending on the size of the central island. The smaller islands, such as ultrasmall magnetic metal nanoparticles and Mn_{12} molecular magnets, are studied in the first part of the thesis (Papers I-III). The larger metal islands, both ferromagnetic and nonmagnetic, are studied in the second part (Papers IV-V). Different size regimes result in different types of energy spectra (discrete for the small and continuous for the large islands), and thus in different ways of calculating the electric current through the system. All the systems are investigated within the regime of weak coupling to the external leads. In this regime, quantum transport is characterized by the physics of Coulomb blockade and can be described theoretically by sequential-tunneling rate equations. Papers I-III are purely theoretical, while Papers IV-V consist both of experimental and theoretical parts, the theoretical ones belonging explicitly to this thesis.

In Paper I we present a theory of quantum transport through a small ferromagnetic nanoparticle in which particle-hole excitations are coupled to spin collective modes. For strong electron-magnon coupling, we find that the tunneling conductance as a function of bias voltage is characterized by a large and dense set of resonances. Their magnetic field dependence in the large-field regime is linear, with slopes of the same sign. Both features are in agreement with tunneling experiments on similar nanoparticles.

Papers II and III deal with transport through a Mn_{12} molecule. The many-body energy spectrum (composed of spin multiplets) and spin-dependent inter-level transition matrix elements used in transport calculations are determined by means of spin density-functional theory (SDFT). This theory provides several other properties of the molecular magnet, such as the magnetic moment and magnetic anisotropy energy of its charged states, anion and cation. In transport calculations, we compare the results obtained by the SDFT with those based on a phenomenological giant-spin model. The tunneling conductance at finite bias is characterized by peaks representing transitions between spin multiplets, separated by an energy on the order of the magnetic anisotropy. We find that the orbital degrees of freedom, included in SDFT and absent in the spin model, play an important role in transport and can lead to negative differential conductance.

In Paper IV we investigate spin accumulation in a Ni/Au/Ni single-electron transistor assembled by atomic force microscopy. Transport measurements in magnetic field at 1.7 K reveal no clear spin accumulation in the device (that is, no tunneling-magnetoresistance (TMR) signal is observed), which can be attributed to fast spin relaxation in the Au disk caused by strong spin-orbit interaction. From numerical simulations using the rate-equation approach of orthodox Coulomb-blockade theory, we can put an upper bound of a few nanoseconds on the spin-relaxation time for electrons in the Au disk.

The focus of Paper V is on magnetic-field dependent transport in nanoscaled ferromagnetic Co/Ni/Co single-electron transistors. Magnetotransport measurements carried out at 1.8 K reveal TMR traces with negative coercive fields, which we interpret in terms of a switching mechanism driven by the shape anisotropy of the central wire-like Ni island. A large TMR of about 18% is observed within a finite source-drain bias regime. A numerical simulation within the Coulomb-blockade theory gives a TMR which is on the order of magnitude of the experimental signal. The TMR decreases rapidly with increasing bias. The vanishing of the TMR with bias is tentatively ascribed to excitations of magnons in the central island, which cause a fast decrease of the island spin polarization.

List of publications

I Electron-Magnon Coupling and Nonlinear Tunneling Transport in Magnetic Nanoparticles
Ł. Michalak, C. M. Canali and V. G. Benza
Physical Review Letters, vol. 97, p. 096804, 2006
Contribution: I participated in the planning of this study, I did all the calculations. I participated in the analysis of the results and in writing the paper.

II Theory of Tunneling Spectroscopy in a Mn_{12} Single-Electron Transistor by Density-Functional Theory Methods
Ł. Michalak, C. M. Canali, M. R. Pederson, M. Paulsson and V. G. Benza
Physical Review Letters, vol. 104, p. 017202, 2010
Contribution: I planned and carried out the transport part of the calculation, and played a major role in its analysis. I participated in the analysis of the DFT part of the calculation and its results, as well as in discussing and writing the whole paper.

III Giant-Spin Hamiltonian versus First-Principles Approach in the Theory of Tunneling Transport in Single-Molecule Magnets
Ł. Michalak, C. M. Canali and M. R. Pederson
in manuscript
Contribution: I planned and carried out the transport part of the calculation, and played a major role in its analysis. I participated in the analysis of the DFT part of the calculation and its results. I wrote the paper.

IV Probing Spin Accumulation in Ni/Au/Ni Single-Electron Transistors with Efficient Spin Injection and Detection Electrodes

R. S. Liu, H. Pettersson, Ł. Michalak, C. M. Canali and L. Samuelson

Nano Letters, vol. 7, p. 81, 2007

Contribution: I planned and carried out all the theoretical simulations. I participated in the planning of this study, in the analysis of the experimental and theoretical data and in writing the paper.

V Large Magnetoresistance in Co/Ni/Co Ferromagnetic Single-Electron Transistors

R. S. Liu, H. Pettersson, Ł. Michalak, C. M. Canali, D. Suyatin and L. Samuelson

Applied Physics Letters, vol. 90, p. 123111, 2007

Contribution: I planned and carried out the transport part of the numerical calculations. I participated in the planning of this study, in the analysis of the experimental and theoretical data and in writing the paper.

The following publication is not included in the dissertation:

VI Tunneling Anisotropic Magnetoresistance in Co/AlOx/Au Tunnel Junctions

R. S. Liu, Ł. Michalak, C. M. Canali, L. Samuelson and H. Pettersson

Nano Letters, vol. 8, p. 848, 2008

I participated in the discussion of several physics issues connected with this project.

Populärvetenskaplig sammanfattning

Elektronen har, bortsett från sin massa, två grundläggande fysikaliska egenskaper som är av största vikt för denna avhandling i synnerhet och världen i allmänhet: laddning och spinn. Den förra egenskapen har i tiotals decennier använts inom det framgångsrika området elektronik. Den andra ger nu framför våra ögon upphov till det nya och fascinerande området spinntronik, minst lika tekniskt revolutionerande som elektronik var i sin tid. Elektronspinnet har redan tillämpats i skriv- och läshuvuden i moderna hårddiskar, men det finns mer kvar att hämta. Det övergripande målet med spinntronik är att få elektronikkomponenter som är ännu mindre till storlek och som förbrukar mindre energi än de komponenter som är tillgängliga idag.

Ja, just elektronspinnet är nyckelstorheten inom spinntronik och för denna avhandling. Men vad är spinn för något? Förenklat sett kan spinnet tänkas som den egenskap som beskriver elektronens rotation kring sin egen axel. Denna rotation kan ske i två riktningar: med- och moturs, varför man talar om spinnets två möjliga riktningar: upp och ned. "Upp" och "ned" anges med relation till det magnetfält vari elektronen befinner sig, alternativt till materialets magnetisering. "Upp" betyder längs fältets (magnetiseringens) riktning, "ned" mot fältets (magnetiseringens) riktning. Det finns en djupare anledning för att välja spinnets riktning på detta sätt. Nämligen står spinnet och magnetism i nära samband till varandra. Det är bara i magnetfält som elektronspinnet "syns" och utan spinnet

hade man i sin tur inte haft magnetism i materia (den andra nödvändiga ingrediensen är här elektrisk laddning). Man kan även säga att en elektron beter sig som en liten magnet när den rör sig i ett magnetfält eller i ett magnetiserat material.

Problemet med praktiska användningar för elektonspinnet är att en viss elektrons spinn bara bevarar samma riktning över mycket korta avstånd, sedan blir spinnet av ett antal elektroner slumpmässigt fördelat. Spinnet är alltså oväsentligt i vanliga elektronikkomponenter, vars dimensioner är relativt stora. Detta problem överkoms med nanoteknikens uppkomst. Den har gett oss redskap för att tillverka nanometersmå system i vilka elektronspinnets riktning hålls konstant.

Ett för nanotekniken typiskt och för denna avhandling grundläggande system är en en-elektron-transistor. Denna liknar en vanlig transistor och består i stort sett av två makroskopiska elektroder och en "ö" mitt emellan dem; ön är skild från elektroderna med hjälp av tunna lager av isolerande material. Ett visst antal elektroner finns på ön, vars storlek tillhör nanometerskalan. Öns och hela transistorns små dimensioner innebär att spinnet (oftast) är bevarad när elektroner passerar genom systemet och att även andra kvantmekaniska fenomen börjar spela in.

Om isolatorlagren mellan elektroderna och ön är tillräckligt tunna kan elektroner tunnla genom lagren, tack vare sina vågegenskaper. (Hade elektroner varit som biljardkulor, hade tunnling varit omöjligt och de hade stannat kvar där de befinner sig.) Två andra kvantmekaniska fenomen uppstår ur öns lilla storlek. De elektroner som är instängda i ön kan endast anta vissa, diskreta energinivåer, precis som elektroner i en atom eller i en molekyl. Ju färre elektroner i ön, desto större avstånd mellan energinivåerna. Dessutom blir elektrisk växelverkan mellan elektronerna stor p.g.a. de korta avstånden dem emellan. Detta leder till att det kommer att kosta energi (en s.k. laddningsenergi) när man vill lägga en elektron till ön, för de andra elektronerna, som redan befinner sig där, kommer att repellera denna starkt. Detta fenomen kallas Coulomb-blockad. Coulomb-blockaden leder till att elektronerna tunnlar genom ön en i sänder.

Antalet elektroner i ön kan vara olika. Innehåller ön många elektroner (som

t.ex. en metallpartikel), blir Coulomb-blockaden viktigare än de nu relativt små energinivåavstånden. Har den få elektroner (som t.ex. en molekyl eller en s.k. kvantprick), blir energiavstånden större än laddningsenergin, och energikvantiseringen viktigare än Coulomb-blockaden. Därför är det lämpligt att dela upp en-elektrontransistorer i två kategorier: kvantprickar (där energi är diskret) och metallpartiklar (där energi är nästan kontinuerlig). De tre första artiklar som denna avhandling bygger på studerar just (små) kvantprickar, medan de två sista artiklarna undersöker (större) metallpartiklar.

I den första artikeln undersöks en liten magnetisk metallpartikel, som har sin egen magnetisering och vars diskreta elektrontillstånd kopplas till en s.k. magnon. En magnon kan också kallas spinnvåg och är en sorts samspel av partikelelektronernas spinn. Den liknar ljudvågar i fasta ämnen som i sin tur kan tänkas som samspel av enskilda atomers vibrationer. Växelverkan mellan elektrontillstånden och magnonen påverkar transport av elektroner (eller, med andra ord, elektrisk ström) genom partikeln och gör den mer komplicerad på ett sätt som även har observerats i experiment.

Artiklarna II och III handlar om elektrontransport i en molekylär magnet Mn_{12}-acetat. Mn_{12} är en stor molekyl med ett mycket stort totalt spinn (summan av alla elektroners spinn i molekylen är alltså stor) som dessutom är mycket stabilt över tiden. Vi har visat bl.a. att addition eller subtraktion av en elektron till eller från molekylen höjer respektive minskar molekylens spinn. Transport genom molekylen påverkar alltså dess magnetiska tillstånd, vilket skulle kunna leda till en tillämpning som minnescell (en s.k. qubit) för framtidens kvantdatorer.

Artiklarna IV och V diskuterar transport genom större metallpartiklar. Dessa två artiklar består både av experimentella och teoretiska delar; det är de teoretiska delarna som direkt hör till denna avhandling. Här är de externa elektroderna magnetiska, av nickel i artikel IV och av kobolt i artikel V, och deras magnetiseringar kan ha olika riktningar i relation till varandra. Metallpartikeln kan vara både omagnetisk, som guldpartikeln i artikel IV, eller magnetisk, som nickelpartikeln i artikel V.

I omagnetiska material är antalet elektroner med spinn upp och spinn ned lika stort. När ett material har en viss magnetisering, som t.ex. järn eller kobolt, har balansen ändrats och majoriteten av elektronerna har den ena riktningen på sitt spinn, medan minoriteten har den andra. Om vi nu injicerar ström av elektroner med, t.ex., spin upp från den ena elektroden till den omagnetiska partikeln i artikel IV, kan en spinn-obalans i princip byggas i partikeln om spinnen inte förlorar sin ursprungliga riktning. Denna obalans i partikelelektronernas spinnfördelning gör att strömmen genom vår en-elektron-transistor beror av de externa elektrodernas magnetiseringsorientering relativt varandra. Är magnetiseringarna parallella blir strömmen större än i det antiparallella fallet. Fenomenet att strömmen, eller resistansen, beror av elektrodernas relativa magnetiseringsorientering kallas magnetoresistans och tillämpas redan i hårddiskars skriv- och läshuvuden.

Magnetoresistans definieras som en relativ differens mellan den resistans som motsvarar antiparallell magnetiseringsorientering och resistansen för de parallellt orienterade magnetiseringarna. När fenomenet orsakas av tunnlande elektroner, som i just vårt fall, heter det tunnelmagnetoresistans (TMR). I experimentet (artikel IV) har vi dock inte sett en tydlig TMR, vilket tyder på att de injicerade elektronerna förlorar sitt spinn ganska snabbt när de tunnlat in i guldpartikeln. Med hjälp av teoretiska modelleringar har vi uppskattat tiden för denna "spinn-förlust" till högst några nanosekunder.

I det experimentella försöket som tillhör artikeln V har vi undersökt en ferromagnetisk transistors resistans i olika externa magnetfält. Olika riktningar på magnetfälten motsvarar olika riktningar på elektrodernas magnetiseringar. Experimentet har gett en TMR på ca. 18% och de teoretiska beräkningarna visar på en TMR av samma storleksordning. TMR avtar snabbt som funktion av elektrisk spänning tillämpad genom systemet, vilket vi tillskriver exciteringar av magnoner, vilket i sin tur minskar partikelns magnetisering.

Fortsatta studier inom avhandlingens område kommer troligtvis att leda till synnerligen praktiska och viktiga tekniska tillämpningar i extremt kompakta, strömsnåla komponenter, som t.ex. sensorer, minnesenheter och magnetiska logikkret-

sar.

Avhandlingens första kapitel innehåller en konceptuell inledning till de studerade systemen. Det andra kapitlet diskuterar metoden för teoretiska beräkningar (masterekvation). De två sista kapitlen handlar om elektrontransport i nanomagneter och magnetoresistanseffekter i ferromagnetiska en-elektron-transistorer.

Contents

1

Conceptual background

Two leitmotivs continue to recur and interweave throughout this thesis: magnetism and electron transport. Their meeting point is the realm of small systems, nanophysics. The aim of this introductory chapter is to give a flavor of these two themes.

1.1 Magnetism in matter

1.1.1 Basic ideas

In principle all the magnetic properties of matter can be derived from the relativistic Dirac equation which describes the time evolution of an electron wave function

$\psi(\vec{r},t)$ in an external electromagnetic field

$$H\psi(\vec{r},t) = i\hbar\frac{\partial\psi(\vec{r},t)}{\partial t}, \tag{1.1}$$

where the Hamiltonian H is given by a relativistic formula

$$H = c\,\hat{\alpha}\cdot\left(\vec{p}-\frac{e}{c}\vec{A}\right)+\hat{\beta}mc^2+e\phi. \tag{1.2}$$

For Eq. (1.1) to make sense with the Hamiltonian defined as above, the coefficients can be written [1] as

$$\hat{\beta} = \begin{pmatrix} \hat{1} & 0 \\ 0 & -\hat{1} \end{pmatrix} \text{ and } \hat{\alpha} = \begin{pmatrix} 0 & \vec{\sigma} \\ \vec{\sigma} & 0 \end{pmatrix}, \tag{1.3}$$

where the components of $\vec{\sigma}$ are the Pauli matrices according to the following

$$\vec{\sigma} = (\hat{\sigma}_x,\hat{\sigma}_y,\hat{\sigma}_z) = \left(\begin{pmatrix} 0 & 1 \\ 1 & 0 \end{pmatrix}, \begin{pmatrix} 0 & -i \\ i & 0 \end{pmatrix}, \begin{pmatrix} 1 & 0 \\ 0 & -1 \end{pmatrix}\right) \tag{1.4}$$

and $\hat{1}$ is a 2×2 identity matrix. Obviously, Eq. (1.1) is a four-dimensional problem and $\psi(\vec{r},t)$ has four components. Two of them describe an electron (positive energies), while the other two correspond to positron holes (negative energies). The two electronic components are in a direct relationship to the electron spin and the very concept of electron spin comes out here automatically, without any prior assumptions. In the nonrelativistic limit, it is possible to decouple the Dirac Hamiltonian (1.2) into the positive and negative solutions [1]. When this is done, we obtain a row of terms, each corresponding to a different single-electron interaction.

In particular, one of the terms, known as the Zeeman Hamiltonian and resulting from the aforementioned decoupling procedure, describes the influence of an external magnetic field $\vec{B}$ on the electron orbital motion

$$H_{\text{Zee}} = -\vec{m}\cdot\vec{B} = -\frac{\mu_B}{\hbar}\vec{B}\cdot\left(\vec{l}+2\vec{s}\right), \tag{1.5}$$

where the electron magnetic moment $\vec{m} = -\mu_B \left(\vec{l} + 2\vec{s}\right)/\hbar$ includes the contribution both from the orbital angular momentum $\vec{l}$ and the spin $\vec{s}$. The Zeeman interaction aligns the orbital and spin magnetic moments with the field $\vec{B}$. Without the Zeeman interaction it would be impossible to magnetize materials at a macroscopic scale. This interaction is also responsible for the splitting of spectroscopic lines, since the external magnetic field affects through it the electronic levels of the system in question.

Before we turn our attention to another interaction that can be deduced from the Dirac equation, let us first ponder a little on the situation that arises when we put together a certain number of electrons; this is quite a typical case if we study atoms, molecules, nanostructures or bulk. The electrons will interact with each other and we are now facing a vast variety of collective phenomena that all stem from the electron-electron interaction. Understanding "correlation", as electron-electron interactions are sometimes referred to, has been one of the major challenges of solid state physics and is yet to be fully accomplished. The key ingredients in the electron-electron interaction are the Coulomb repulsion and the Pauli exclusion principle that leads to the symmetrization postulate imposed on the electron wave function. These two contributions give rise to a so-called *exchange* interaction that couples the spins of interacting electrons. This spin-spin coupling is directly visible in the Heisenberg Hamiltonian, which constitutes an approximate, effective model for studying exchange. The Heisenberg model for a system of N spins can be stated as follows

$$H_{\text{Heis}} = -\sum_{i \neq j}^{N} J_{ij} \vec{s}_i \cdot \vec{s}_j. \tag{1.6}$$

Here the spins $\vec{s}_i$, $\vec{s}_j$ are coupled pairwise by the coupling constant J_{ij}. This coupling occurs via the orbital parts of the electron wave functions and the electrostatic interaction. The sign of the coupling constant determines how the spins will be aligned with each other. Its positive value gives a ferromagnetic (parallel) alignment, while its negative value yields an antiferromagnetic (antiparallel)

configuration. The exchange integral J_{ij} vanishes quickly with the distance between the interacting electrons, which means that the exchange is a short-range interaction. Nevertheless, it is the strongest magnetic interaction and the one responsible for the occurrence of spontaneous magnetization (that is, a collective spin moment) at a microscopic scale. Roughly speaking, exchange can be inter- or intra-atomic, or itinerant.

Let us now go back to the Dirac equation (1.1). Another important term that can be deduced from Eq. (1.2) is the *spin-orbit* interaction. Essentially, the spin-orbit interaction couples the spin $\vec{s}$ with the orbital angular momentum $\vec{l}$, and for an electron in a central electrostatic field (akin the field felt by electrons in an atom), it takes a simple form of

$$H_{\mathrm{s-o}} = \xi(r)\vec{s}\cdot\vec{l}, \tag{1.7}$$

where the expectation value $\zeta = \langle\xi(r)\rangle$ is positive and is called the spin-orbit coupling constant; its dimension is that of energy. The moments $\vec{s}$ and $\vec{l}$ can both represent single-electron angular momenta or be collective moments of a number of electrons (e.g., a whole atom or a nanoparticle).

The orbital motion of an electron is affected by its crystal environment, that is, the electric field created by the lattice. This ligand field, highly dependent on the system symmetry, can deform the electron orbital motion and even quench it. Since the orbital angular momentum is coupled to the electron spin by means of the spin-orbit interaction, the ligand field can succeed in locking the spin (or the macroscopic magnetization, which in many ways may be perceived as a giant spin angular momentum) in a certain direction. Such direction, called an *easy axis*, will be energetically favorable, and the energy gain is referred to as the *magnetic anisotropy energy*. It is important to note that there would be no magnetocrystalline anisotropy, i.e., magnetic anisotropy caused by the crystal (or ligand) field, were it not for the spin-orbit interaction. The exchange interaction alone is in itself isotropic (cf. Eq. (1.6)) and, furthermore, it does not include the effect of the ligand field (or the orbital motion, for that matter). The magnetocrystalline

anisotropy is a crucial phenomenon when designing new, both micro- and macroscopic, devices, as it is present in molecules, nanostructures and bulk.

However, the magnetocrystalline anisotropy is not the only contribution to the magnetic anisotropy of a system. Another kind of anisotropy, also arising from the influence of the ligand field, is the surface anisotropy, which can appear in small systems, where the surface is relatively large when compared with the volume part of the system (nanoparticles are a good example here). The mere existence of a reduced symmetry at the surface does not automatically imply a surface anisotropy though [2]. In thin films or elongated systems, such as nanowires, the shape anisotropy is important. This kind of anisotropy stems out of the magnetostatic dipole-dipole interaction between the atomic magnetic dipoles $\vec{m}$ which minimizes the energy for the direction parallel to the geometric axis of the system.

Irrespective of the microscopic origin of the magnetic anisotropy, the energy dependence on the magnetization direction is usually expressed with the use of a phenomenological model, the starting point of which is the following second-order uniaxial approximation

$$E_1/V = K_1 \sin^2 \vartheta, \tag{1.8}$$

where V is the volume of the sample and K_1 denotes the second-order uniaxial anisotropy constant. This simple model can be extended to higher-order, uniaxial or of a more reduced symmetry, terms. The Mn_{12}-acetate molecular magnet, which I discuss in Chapter 3 (and Papers II-III), is a beautiful example of a highly symmetric system with almost uniaxial anisotropy and a very large value of magnetic anisotropy energy ($4 - 5$ meV). Otherwise, the ferromagnetic single-electron transistors discussed in Chapter 4 (Papers IV-V) involve the use of shape anisotropy for aligning the magnetizations of their elongated electrodes.

1.1.2 3*d* transition metals

Transition metals of the iron series (Mn, Fe, Co and Ni) are of particular importance for the work done for this thesis. The average spin moment per atom is

noninteger in these elements (e.g., 1.73 μ_B for Co [3], where μ_B is the Bohr magneton), which suggests an itinerant nature of their magnetic properties. Namely, it is the electron gas, grouped in energy bands, that is responsible for the magnetism of these materials. The valence electrons in the iron-series elements belong to

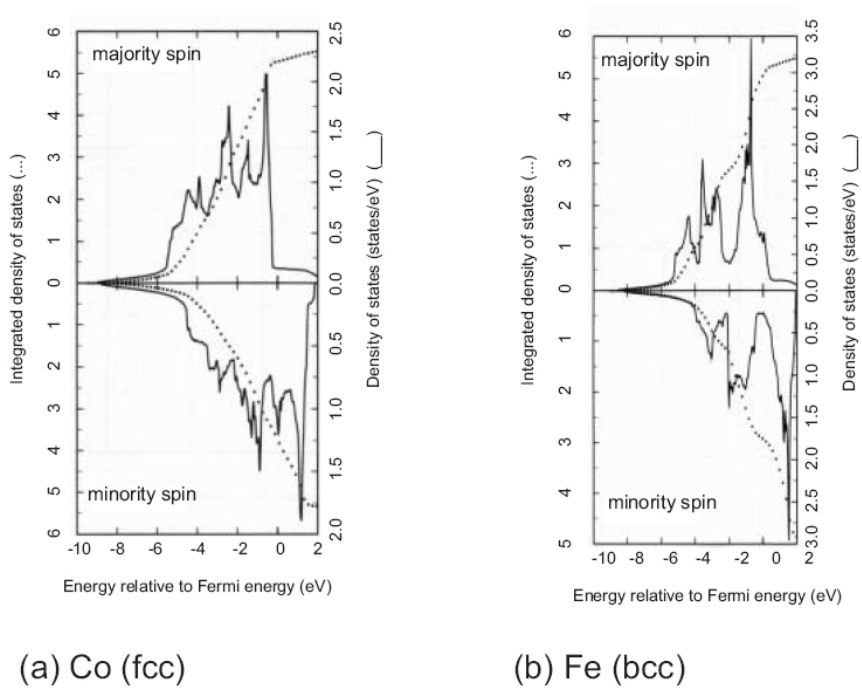

Figure 1.1: The density of states (DOS) for (a) Co (fcc) and (b) Fe (bcc) calculated by ab-initio methods. The DOS is much higher for the minority-spin band, as most of the majority-spin electrons occupy states below the Fermi energy (taken to be equal to zero). Adapted from Ref. [4].

a wide, completely delocalized and free-electron-like $4s$ band and a narrow band of more localized and weakly interconnected $3d$ orbitals. The $4s$ band, due to its small density of states (DOS) is of little bearing on the magnetic properties. On the other hand, the $3d$ band has a large DOS and, consequently, takes responsibility for the magnetism of the transition metals. The ferromagnetic phase occurs for

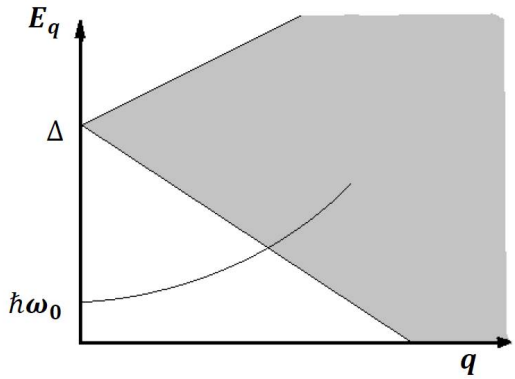

Figure 1.2: Elementary excitations in a ferromagnet. The Stoner quasiparticles are allowed everywhere between the two straight lines. The magnon excitations weaken and broaden as they cross the Stoner band. Based on Ref. [4].

Co, Ni and Fe, i.e., the elements for which the $3d$ band is more than half-filled, and that permits the electrons to be easily delocalized from one atomic $3d$ orbital to another. Mn appears in an antiferromagnetic configuration, since this element has a half-filled $3d$ band and hence delocalization is possible only between those neighboring orbitals the magnetic moments of which are aligned antiferromagnetically (delocalization between ferromagnetically aligned orbitals is forbidden by the virtue of Pauli exclusion principle).

For the iron-series elements an electron band can be divided into a "majority-spin" band and a "minority-spin" band. The densities of states for two such subbands are moved relative one to another by an exchange splitting $\Delta = \varepsilon_{\vec{k}\uparrow} - \varepsilon_{\vec{k}\downarrow}$, and do not differ otherwise, as postulated by Stoner [4]. Figure 1.1 shows the results of ab-initio calculations carried out for Co (fcc) and Fe (bcc). We can see from this figure that Stoner's postulate makes a very good approximation, as the DOS for the majority spins has shifted down from the Fermi energy, relative to the minority spins. This shift takes place due to the strong exchange coupling. A

broad and low in magnitude $4s$ subband can also be seen, while the $3d$ bands are narrower and much more intensive.

The Stoner model is essentially based on the idea of quasiparticles. However, ferromagnetic transition metals support even low-energy collective spin excitations. These spin waves or magnons have a quadratic dispersion relation according to

$$\hbar\omega = D|\vec{q}|^2 + \hbar\omega_0, \tag{1.9}$$

where $\vec{q}$ is the magnon wave vector. The spin-wave stiffness constant D is proportional to the exchange constant J and the square of the lattice constant a, and its value is 34 meV for Fe, 79 meV for Co and 29 meV for Ni [5]. The energy gap $\hbar\omega_0$, i.e., the energy of the uniform spin wave for which $q = 0$, is proportional to the magnetic anisotropy energy of the system (including shape anisotropy) and amounts to a small fraction of 1 meV. Both the energy $E_q = \varepsilon_{\vec{k}+\vec{q},\downarrow} - \varepsilon_{\vec{k}\uparrow}$ of the Stoner particle-hole excitations (a change in the electron momentum and spin) and the energy of the magnon are plotted in Fig. 1.2. The spin waves are distinguishable for low energies (small q) and decay more readily when they enter the region of Stoner excitations (higher energies and larger q).

To conclude our deliberations on the basic concepts of magnetism in matter, it is instructive to take a look at the scale of the energies for the Coulomb, exchange, bonding and spin-orbit interactions. Figure 1.3 shows an order-of-magnitude estimate of these energies for $3d$ ions in bulk. The largest energy corresponds to a change of charge of the $3d^n$ion (ionization). The second largest is the energy of the Coulomb and exchange interactions that couple the n electrons into terms ^{2S+1}L. Bonding (or interaction with the ligand field) is comparable to the two latter interactions, since the $3d$ electrons are not completely localized and overlap with the neighboring ligands. The smallest is the energy of the spin-orbit coupling. This is due to the quenching of the orbital angular momentum that occurs in the ligand field. As a result, the effective spin-orbit interaction energy is about 100 times smaller than the spin-orbit parameter [6].

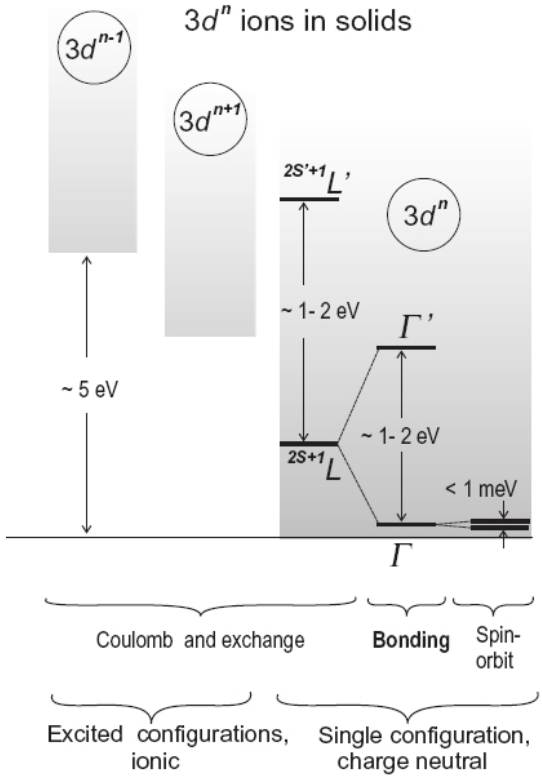

Figure 1.3: The energy scale of the relevant interactions in the bulk $3d$ transition-metal ions. Adapted from Ref. [6].

1.2 Transport in nanostructures

Over the last decades, hopes for new applications in the fast developing sector of data storage and computation, as well as the new technological possibilities and interest in nanostructures as a crossover region between the macro- and microscopic phenomena have drawn much attention to transport in nanometer-sized systems. A typical transport-study object is a double-junction *nanodevice*, that is, a device composed of a nanoscaled central electrode (island) which is attached

to two external, micro- or macroscopic, electrodes (source and drain), as in the schematics of Fig. 1.4; the contact region between the island and the leads functions as a tunneling potential barrier. These three electrodes form a closed circuit, and when a finite bias voltage is applied across the nanodevice, an electric current might flow through it. Whether the current will flow or not depends on the interplay between the electrochemical potentials in the leads and the energy spectrum of the island. Three factors, related to the three regions of the nanodevice (leads, island and contact regions), are crucial when modeling the nanodevice. The first factor is the energy spectrum and other properties (such as the size, charging energy, spin relaxation or magnetic moment) of the central island. Next are the magnetic moments of the external electrodes and their relative orientation (which can be ferromagnetic, antiferromagnetic or generic; of course, the external electrodes may as well be nonmagnetic). And the last factor is the strength of the inter-electrode coupling in the contact regions is of vital importance, since it sets rules for how the electrons that make up the current will hop from one element of the device to another.

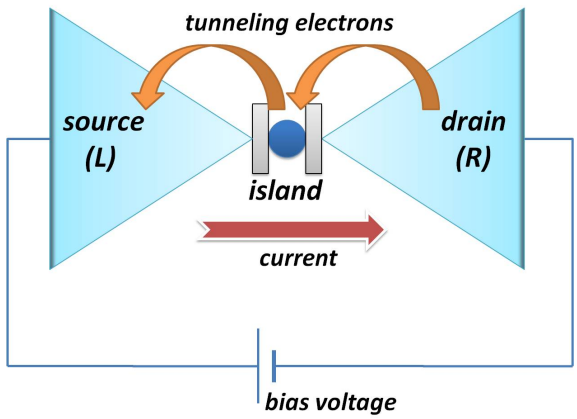

Figure 1.4: Schematics of a single-electron transistor (SET), the system typical for this thesis. Note the three electrodes: source, drain and island, as well as the tunneling barriers (painted in grey).

The unique property of nanostructures is their *small* size. The smallness of the central island affects transport through it in two ways. First, the spectrum of the island electrons becomes discrete when the island size decreases sufficiently, and the average level spacing δ becomes finite. Second, the energy to add an electron to the island, i.e., the so-called *charging energy* $E_C = e^2/2C$ (C is the island capacitance), depends on the island size: the smaller the island, the smaller its capacitance, and the more it costs to charge it. This energy cost must be paid by sources of the bias voltage applied across the device. If the energy provided by the bias is lower than E_C, electrons are prohibited from hopping from the external electrodes onto the island. Such a complete suppression of current is referred to as *Coulomb blockade*. The value of E_C is typically of the order of $10^{-5} - 10^{-4}$ eV [7], which corresponds to temperatures $T \approx 1 - 10$ K. Thus, for low temperatures charging effects dominate the electron transport. For the energy spectrum to be discernible in the form of conductance resonances, it is required that $\delta \gg k_{\mathrm{B}}T$, where k_{B} is the Boltzmann constant.

The strength of the island coupling to the external electrodes determines the value of the energy-level broadening Γ in the island.[1] The level broadening helps us distinguish different tunneling regimes in which transport takes place in significantly different ways. The most relevant for the systems studied in this thesis, is the limit of weak coupling between the island and the leads, where $\Gamma \ll k_{\mathrm{B}}T$. Within the weak-coupling regime transport occurs via sequential tunneling processes of individual electrons. Consequently, a transistor-like nanodevice, such as the one sketched in Fig. 1.4, in which tunneling occurs via sequential processes, is called a *single-electron transistor*. These tunneling processes, first-order in the coupling, dominate if the system is far from degeneracy points of two consecutive charge states. The second-order processes that constitute cotunneling become important for intermediate coupling strengths, $\Gamma \sim k_{\mathrm{B}}T$. For even

[1] Γ can be viewed also as the tunneling rate for the electrons hopping from one electrode to another: the stronger the coupling, the larger the tunneling rate, and the more broadened the island levels.

stronger couplings, when the junction resistance falls below the quantum resistance h/e^2, higher-order processes take over and the perturbative approach is no longer suitable at the degeneracy points. An example of higher-order processes is the Kondo effect that, below a certain temperature, leads to an enhanced conductance in quantum dots.

The external leads in the nanodevice of Fig. 1.4 can be made from normal metal or ferromagnet. The leads are assumed to be Fermi liquids throughout this thesis, that is, reservoirs of noninteracting particles (quasiparticles). If the leads are ferromagnetic, the relative orientation of their magnetic moments affects the current, giving rise to *tunneling magnetoresistance* (TMR). TMR may appear if at least two of the three electrodes of the given SET are ferromagnetic. However, for a SET with two ferromagnetic leads and a nonmagnetic island, TMR will be observable only if spin relaxation on the island is slow enough to allow for a net magnetic moment of the spins injected from the leads to build up on the island [8]; the process is referred to as the *spin accumulation*.

2 Method

Since all the experiments that motivated the work done for this thesis were conducted in the weak-coupling regime ($k_{\mathrm{B}}T > \Gamma$), the natural choice of tool for theoretical calculations was the *master equation* (see e.g. [9, 10]). Below follows a detailed description of the master-equation technique, in general and as applied to the studied systems.

2.1 Single-electron transistor (SET)

The electric-circuit geometry of a single-electron transistor (SET) in its typical double-junction configuration is drawn in Fig. 2.1. The left (L), right (R) and central (I) electrodes can be either ferromagnetic or nonmagnetic, and the magnetization of one of the electrodes can be controlled independently of the magneti-

zations of the other electrodes. The central island is separated from the external leads (which sometimes are called source and drain) by means of tunneling barriers (usually a thin layer of an oxide insulator). The energy spectrum of the island is regulated electrostatically by the gate electrode (parametrized by capacitance C_{g} and gate voltage V_{g}). The bias voltage applied across our double junction is usually chosen in a symmetric way, so that the potentials at the two leads satisfy $V_{\mathrm{R}} = V_{\mathrm{L}}$. The bias provides electrons in the leads with energy necessary for overcoming the Coulomb blockade, and creating the electric current I_{L} (or I_{R}) through the left (or right, respectively) junction. The junctions can be viewed as capacitors of capacitances C_{L} and C_{R}.

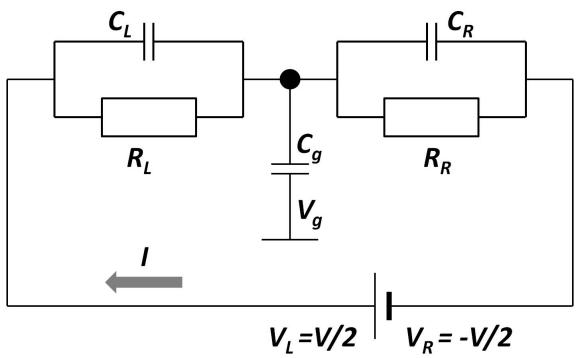

Figure 2.1: A single-electron transistor represented as an element of a dc-circuit. The left and right junctions are described by their capacitance and resistance, respectively. Gate capacitance and gate voltage control the island energy landscape.

The total Hamiltonian of the system in Fig. 2.1 can be written as

$$H = H_{\mathrm{L}} + H_{\mathrm{R}} + H_{\mathrm{I}} + H_{\mathrm{T}}, \tag{2.1}$$

where H_{L} and H_{R} are the Hamiltonians for the left and right leads, respectively, H_{I} describes the island and H_{T} corresponds to tunneling processes that occur between the island and the leads. The external electrodes are assumed to be normal

or ferromagnetic Fermi liquids:

$$H_\alpha = \sum_{\vec{p}\sigma} \varepsilon_{\alpha\vec{p}\sigma} c^\dagger_{\alpha\vec{p}\sigma} c_{\alpha\vec{p}\sigma}, \tag{2.2}$$

where the Fermi operators $c^\dagger_{\alpha\vec{p}\sigma}$ ($c_{\alpha\vec{p}\sigma}$) create (destroy) a quasiparticle measured with respect to the chemical potential μ_α of lead $\alpha = \mathrm{L}$ or R. In the case of a ferromagnetic lead, the Stoner model [11] tells us that the electron band is exchange split into two, majority ($\uparrow$) and minority ($\downarrow$), subbands. The spin asymmetry between the densities of states for the two subbands is strong: $\rho_{\alpha\uparrow}(\varepsilon) \neq \rho_{\alpha\downarrow}(\varepsilon)$ (cf. Fig. 1.1). If we assume that the density of states (DOS) does not depend on energy, we can define an effective spin polarization $\mathcal{P}_\alpha$ of the given lead:

$$\mathcal{P}_\alpha = \frac{\rho_{\alpha\uparrow} - \rho_{\alpha\downarrow}}{\rho_{\alpha\uparrow} + \rho_{\alpha\downarrow}}. \tag{2.3}$$

For normal-metal leads $\mathcal{P}_\mathrm{L} = \mathcal{P}_\mathrm{R} = 0$ and for a half metal we have $\mathcal{P}_\alpha = 1$.

The shape of the island part of the Hamiltonian, H_I, depends on the details of the system in question. The island can have a discrete (see Section 2) or a (quasi-)continuous (see Section 3) energy spectrum or DOS. The details of H_T also depend on this classification.

2.2 Sequential tunneling – master equation

2.2.1 General

In general, a full system of the previous section is governed by the von Neumann equation for the total density operator [12]. Assuming that the interaction part H_T of the Hamiltonian (2.1) can be treated perturbatively and that the off-diagonal terms in the density matrices vanish, we obtain a *master equation* that describes the time evolution of the probability $P_n(t)$ that a given system is in state n at time t [12]

$$\frac{\mathrm{d}P_n(t)}{\mathrm{d}t} = \sum_m \left[W_{nm} P_m(t) - W_{mn} P_n(t) \right], \tag{2.4}$$

where W_{mn} is a transition rate of going from state n to state m (cf. e.g. Ref. [13]). The process of going from n to m is assumed to be Markovian, i.e., independent of the previous transitions. Both for metallic [14–16] and discrete dots [10, 17–20], the master equation turned out to be a perfect model for describing the SET in the limit of weak coupling, where tunneling of electrons from the source to the drain is incoherent and takes place in a sequence of two processes independent of each other. The charging energy of the island quenches simultaneous tunneling of two electrons of opposite spins [21].

We calculate the tunneling rates W_{nm} by using the first-order perturbation theory in the tunneling Hamiltonian H_{T} and solve a set of master equations for all the states n in the steady-state limit

$$\frac{d\hat{P}}{dt} = \hat{A}\hat{P} = 0 \tag{2.5}$$

together with the normalization condition $\sum_n P_n = 1$. Here $\hat{P}$ is the probability vector, the components of which are probabilities P_n, and $\hat{A}$ is a matrix that comprises all the transition rates W_{nm}. By the use of the probability distribution and rates we can later compute the current through a given junction (lead).

2.2.2 Quantum dots

For a quantum dot, that is, an island with a discrete DOS ($\Delta\varepsilon \gg k_{\mathrm{B}}T$), n and m label the many-body energy states on the island, and W_{mn} will be a rate for transition from state n to state m. This transition is triggered and accompanied by a tunneling of an electron onto or off the island. We calculate the rate of this transition by the use of Fermi's golden rule

$$W^{\alpha}_{mn} = \frac{2\pi}{\hbar} \sum_{i^\alpha, f^\alpha} \left|\langle f^\alpha| \langle m| H_{\mathrm{T}} |n\rangle |i^\alpha\rangle\right|^2 W_{i^\alpha} W_{f^\alpha} \delta\left(\varepsilon_f - \varepsilon_i\right), \tag{2.6}$$

where W_{i^α} and W_{f^α} are thermal distribution functions of the final $|f^\alpha\rangle$ and initial $|i^\alpha\rangle$ states in lead α. The initial (final) energy of the system is $\varepsilon_{i(f)}$. The tunneling

Hamiltonian for a quantum dot is given by

$$H_{\mathrm{T}} = \sum_{\alpha\vec{k}\sigma m} \left(T_{\alpha\vec{k}\sigma} c^{\dagger}_{\alpha\vec{k}\sigma} d_{m\sigma} \ + \mathrm{H.c.} \right), \tag{2.7}$$

where we assumed spin conservation under tunneling. Operator $d_{m\sigma}$ destroys the island many-body state m with spin σ.

The general formula for the current through the lead α can be expressed as

$$I_{\alpha} = -e \sum_{m,n} P_n \left(W^{\alpha(\mathrm{charging})}_{mn} - W^{\alpha(\mathrm{discharging})}_{mn} \right), \tag{2.8}$$

where the transitions $W^{\alpha(\mathrm{charging})}_{mn}$ are due to the tunneling of an electron onto the island, and the transitions $W^{\alpha(\mathrm{discharging})}_{mn}$ are due to tunnelings off the island. In the weak-coupling regime, the island states $|m\rangle$ are assumed to be unaffected by the interaction with the leads. Consequently, we calculate first the many-body energy spectrum of the island, and then use this spectrum in Eq. (2.6). We interpret the tunneling events in terms of transitions between the island many-body states of different charge.

The quantum-dot method of calculating the rates and current is employed for the ferromagnetic nanoparticle with electron-magnon coupling (Paper I) and the molecular magnet of the Mn_{12}-acetate molecule (Papers II-III). We discuss the details of the calculation leading to the spectra of the isolated nanomagnets in the following chapter.

2.2.3 Metallic grains

In the case of a metallic (or ferromagnetic) island, in which the level spacing $\Delta\varepsilon \ll k_{\mathrm{B}}T$, we can interpret m and n of Eq. (2.4) as different numbers of excessive electrons on the island. The occupancy of the electronic states of the island relaxes to a Fermi-Dirac distribution between subsequent tunneling events. Recalling that the electrons tunnel one by one, we can write the master equation for the time evolution of the probability $P(N)$ that there are N excessive electrons

on the island in the following fashion

$$\frac{\mathrm{d}P(N)}{\mathrm{d}t} = -\left(W_{N+1,N} + W_{N-1,N}\right) P(N) + W_{N,N+1}P(N+1) + W_{N,N-1}P(N-1) \tag{2.9}$$

with the normalization condition

$$\sum_N P(N) = 1. \tag{2.10}$$

The term $W_{N,N+1} = W^{\mathrm{L}}_{N,N+1} + W^{\mathrm{R}}_{N,N+1}$ defines the rate of transition that corresponds to discharging the island from $N+1$ to N excessive electrons.

In the steady-state regime, appropriate for dc-current circuits, we set the time derivative of the probability distribution function equal to zero in Eq. (2.9). We note that the net probability of going between two subsequent states (e.g., N and $N+1$) is zero [22]. Hence we obtain a simple recursive relation

$$P(N)W_{N-1,N} = P(N-1)W_{N,N-1}. \tag{2.11}$$

The above equation can be solved by making use of the normalization condition (2.10). The solution was given in Ref. [22] and reads

$$P(N) = \frac{\prod_{i=-\infty}^{N-1} W_{i+1,i} \prod_{i=N+1}^{+\infty} W_{i-1,i}}{\sum_{j=-\infty}^{+\infty} \left(\prod_{i=-\infty}^{j-1} W_{i+1,i}\right) \left(\prod_{i=j+1}^{+\infty} W_{i-1,i}\right)}. \tag{2.12}$$

The current through the lead α will read

$$I_\alpha = -e \sum_N P(N) \left(W^{\alpha}_{N+1,N} - W^{\alpha}_{N-1,N}\right). \tag{2.13}$$

In general, the rates $W^{\alpha}_{N\pm1,N}$ may depend on the spin polarization ('up' or 'down') of the tunneling electrons. Therefore the current can be split into two spin channels and the spin-polarized current in one of those channels becomes

$$I^{\sigma}_\alpha = -e \sum_N P(N) \left(W^{\alpha\sigma}_{N+1,N} - W^{\alpha\sigma}_{N-1,N}\right), \tag{2.14}$$

where $\sigma = \uparrow, \downarrow$ denotes the spin polarization with respect to a chosen quantization axis. Special caution needs to be paid when dealing with SETs where the electrodes exhibit noncollinear magnetic moments. Obviously,

$$I_\alpha = I_\alpha^\uparrow + I_\alpha^\downarrow. \tag{2.15}$$

In the considered limit of a metallic grain with a continuous energy spectrum, we calculate the tunneling rates $W^\alpha_{N\pm1,N}$ ($\alpha =$ L or R) by integrating, over the energy, the square of the tunneling matrix element that couples the initial and final states at energy E, $|T(E)|^2$ (akin to the one in Eq. (2.7)), weighing it with the densities of states of the central, $\rho_\mathrm{I}(E)$, and of the external α-electrode, $\rho_\alpha(E)$, and with the number of occupied or unoccupied (depending on the direction of the tunneling process) initial and final states. For instance, the charging ($N \to N+1$) tunneling rate through the right junction will be [22]

$$W^\mathrm{R}_{N+1,N} = \int_{-\infty}^{\infty} \mathrm{d}E \frac{2\pi}{\hbar} |T(E)|^2 \rho_\mathrm{R}(E-\varepsilon_\mathrm{F}^\mathrm{R}) f(E-\varepsilon_\mathrm{F}^\mathrm{R}) \rho_\mathrm{I}(E-\varepsilon_\mathrm{F}^\mathrm{I}) \times \left[1 - f(E-\varepsilon_\mathrm{F}^\mathrm{I})\right]. \tag{2.16}$$

Here $\varepsilon_\mathrm{F}^\mathrm{R}$ and $\varepsilon_\mathrm{F}^\mathrm{I}$ are the Fermi energies of the right and central island, respectively, and $f(E)$ is the Fermi-Dirac distribution function. The integration can be simplified if we, for simplicity, assume that

$$\rho_\mathrm{R}(E) = \rho_{\mathrm{R}0} \tag{2.17}$$

and

$$\rho_\mathrm{I}(E) = \rho_{\mathrm{I}0}, \tag{2.18}$$

and

$$T(E) = T_0. \tag{2.19}$$

Then, Eq. (2.16) becomes [23]

$$W^\mathrm{R}_{N+1,N} = \frac{1}{e^2 R_\mathrm{R}} \frac{\varepsilon_\mathrm{F}^\mathrm{R} - \varepsilon_\mathrm{F}^\mathrm{I}}{1 - e^{-(\varepsilon_\mathrm{F}^\mathrm{R} - \varepsilon_\mathrm{F}^\mathrm{I})/(k_\mathrm{B}T)}} \tag{2.20}$$

where

$$R_{\mathrm{R}} \equiv \frac{\hbar}{2\pi e^2 \rho_{\mathrm{R0}} \rho_{\mathrm{I0}} |T(0)|^2} \tag{2.21}$$

is the resistance of the right junction. A similar derivation can be carried out for the other tunneling rates, and the general result reads as follows

$$W^{\alpha}_{N+1,N} = \frac{1}{e^2 R_{\alpha}} \frac{\varepsilon^{\alpha}_{\mathrm{F}} - \varepsilon^{\mathrm{I}}_{\mathrm{F}}}{1 - e^{-(\varepsilon^{\alpha}_{\mathrm{F}} - \varepsilon^{\mathrm{I}}_{\mathrm{F}})/(k_{\mathrm{B}}T)}} \tag{2.22}$$

and

$$W^{\alpha}_{N,N+1} = \frac{1}{e^2 R_{\alpha}} \frac{\varepsilon^{\mathrm{I}}_{\mathrm{F}} - \varepsilon^{\alpha}_{\mathrm{F}} - 2E_C}{1 - e^{-(\varepsilon^{\alpha}_{\mathrm{F}} - \varepsilon^{\mathrm{I}}_{\mathrm{F}} - 2E_C)/(k_{\mathrm{B}}T)}}. \tag{2.23}$$

In order to understand better the meaning of the Fermi-energy difference $\varepsilon^{\alpha}_{\mathrm{F}} - \varepsilon^{\mathrm{I}}_{\mathrm{F}}$, let us first analyze the circuit loop for our double-junction system (Fig. 2.1). The difference between the Fermi energies $\varepsilon^{\alpha}_{\mathrm{F}}$ and $\varepsilon^{\mathrm{I}}_{\mathrm{F}}$ is the energy the electron gains when it tunnels from the lead α to the island:

$$\varepsilon^{\mathrm{R(L)}}_{\mathrm{F}} - \varepsilon^{\mathrm{I}}_{\mathrm{F}} = \frac{e}{C}\left[\left(N + \frac{1}{2}\right) e \pm C_{\mathrm{L(R)}} V - C_{\mathrm{g}} V_{\mathrm{g}} + Q_0\right], \tag{2.24}$$

where the upper (lower) sign corresponds to the index R (L). The first term in the parenthesis is the change, due to tunneling, in the electrostatic energy of the island. The second term represents the work done by the voltage source. The gate-voltage readjustment of the island spectrum is described by the third term, and the last one is some background charge. Equation (2.24) holds if we assume fast charge relaxation on the island, i.e., the time of tunneling is much longer than the time it takes to redistribute the island charge, but still shorter than the time between tunneling events (sequential tunneling limit!).

Equations (2.22) and (2.23) are true for normal-metal islands when the external leads are also nonmagnetic. However, if the leads are ferromagnetic and spin relaxation on the island happens more slowly than charge relaxation, a nonequilibrium spin state forms on the island leading to a spin-dependent splitting in the island Fermi energy, $\Delta E^{\sigma}_{\mathrm{F}}$, where σ is 'up' or 'down' (and we assume that the magnetic moments of the leads are collinear). Now, Eq. (2.14) becomes valid for the current, but what happens to equations (2.22) and (2.23)? The rates will be

now spin dependent and the argument in the general expression for a tunneling rate

$$W^{\alpha}(\varepsilon) = \frac{1}{e^2 R_\alpha} \frac{\varepsilon}{1 - e^{-\varepsilon/(k_{\mathrm{B}}T)}} \tag{2.25}$$

will be modified according to the following

$$W^{\alpha}_{\uparrow\pm}(\varepsilon) = \frac{1}{e^2 R_\alpha} \frac{\varepsilon \mp \Delta E_{\mathrm{F}}/2}{1 - e^{-(\varepsilon \mp \Delta E_{\mathrm{F}}/2)/(k_{\mathrm{B}}T)}} \tag{2.26}$$

for electrons with spin 'up', and

$$W^{\alpha}_{\downarrow\pm}(\varepsilon) = \frac{1}{e^2 R_\alpha} \frac{\varepsilon \pm \Delta E_{\mathrm{F}}/2}{1 - e^{-(\varepsilon \pm \Delta E_{\mathrm{F}}/2)/(k_{\mathrm{B}}T)}} \tag{2.27}$$

for electrons with spin 'down'. The upper (lower) sign corresponds to tunneling onto (off) the island.

Since, obviously, the spin polarized current of Eq. (2.14) will influence the Fermi-level splitting ΔE_{F}, and the latter one will in its turn affect the current, the calculation of the current must be done self-consistently. The self-consistent equation for the spin-polarized current reads [24]

$$\sum_{\alpha=\mathrm{L,R}} \left(I^{\uparrow}_{\alpha} - I^{\downarrow}_{\alpha} \right) = \left(\rho \mathcal{V} e \Delta E_{\mathrm{F}} \right) / \tau_s \tag{2.28}$$

where τ_s is the electron-spin relaxation time in the central electrode, ρ is the density of states (per spin species) and $\mathcal{V}$ is the volume of the central electrode.

3

Quantum transport in ultrasmall nanomagnets

In this chapter I discuss single-electron transistors, the central islands of which possess discrete energy spectra (or, to phrase it differently, discrete densities of states). Section 3.1 deals with the first example of such a discrete system: an ultrasmall magnetic nanoparticle. The magnetic nanoparticle forms a good introduction to the far more complex Mn_{12}-based molecular magnet. The problem of transport through the latter system is studied in Section 3.2.

3.1 Magnetic nanoparticles

This section summarizes our theoretical study of single-electron tunneling transport through a ferromagnetic nanoparticle. The objective of this project was, on the one hand, to provide a model that captures the coupling between particle-hole and spin collective modes in such a nanoparticle and, on the other hand, to pursue an explanation of some important experimental results of Refs. [25] and [26]. A few remarkable features seen in experiment emerge in a very transparent and direct way from our treatment of the electron-magnon coupling. In particular, for strong electron-magnon coupling, we find that the tunneling conductance as a function of bias voltage displays a large and dense set of resonances. Their magnetic-field dependence in the large-field regime is linear and monotonic.

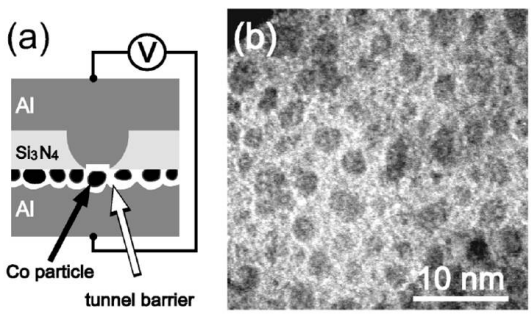

Figure 3.1: (a) Experimental set-up of Ref. [25]. (b) STEM image of the layer of Co particles used in the experiment [25]. Note the smallness of size. Reprinted from Ref. [25].

I start this section with a short resumé of the experiments [25, 26] seminal to the problem in question. Next, I present our model of electron-magnon coupling, followed by its application to the sequential-tunneling calculation. Finally, I discuss the magnetic-field dependence of the conductance spectrum.

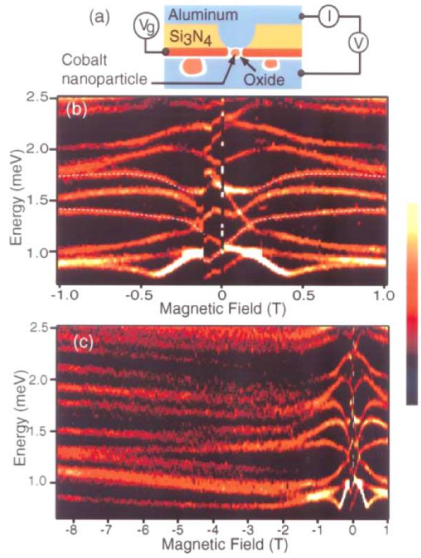

Figure 3.2: (a) Experimental set-up of Ref. [26]. (b) and (c) Plots of tunneling differential conductance in a Co nanoparticle as a function of the magnetic field and bias voltage (the latter quantity is translated into the quasiparticle energies here). Bright (dark) colors correspond to high (low) conductance; the maximum conductance is 3 nS. Reprinted from Ref. [26].

3.1.1 Motivation – experiments

About a decade ago Ralph *et al.* [25, 26] conducted two seminal SET experiments on small ferromagnetic nanoparticles. In the experiments, the two external electrodes were made of Al, the gap between them being ≤ 5 nm, the tunnel barriers were formed by oxidizing the Al leads, and a layer of Co nanoparticles was evaporized between the oxidized electrodes (see Figs. 3.1 and 3.2(a)). The typical diameter of the Co nanoparticles was 1-4 nm, and their center-to-center spacing was 2-5 nm (Fig. 3.1(b)). Devices for which the current-voltage characteristics at 4.2 eV manifested a Coulomb staircase were selected for detailed measurements,

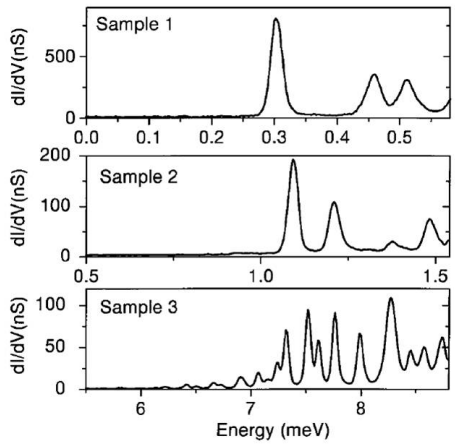

Figure 3.3: Tunneling spectra of three different samples at $T = 20$ mK and $B = 1$ T. Reprinted from Ref. [25].

ensuring that transport took place via individual nanoparticles. The SET set-up in Ref. [26] was also equipped with a gate electrode for probing the many-body states on the nanoparticle.

Conductance spectra of well-resolved resonance peaks (Figs. 3.3 and 3.4) and a magnetic-field dependence of the tunneling resonances (Figs. 3.2(b,c), 3.5 and 3.6) were measured. The tunneling conductance spectrum is denser (the mean energy spacing is about 0.2 meV) than the one predicted in an independent-particle picture (Figs. 3.3 and 3.4), which suggests that the quasiparticle Stoner states are coupled to spin-wave excitations. As the many-body energy levels are coupled to the direction of the particle magnetization, the reorientation of the magnetization leads to energy shifts and energy-level crossings, which underlines the importance of nonequilibrium transitions. Furthermore, the tunneling resonances exhibit a complicated nonmonotonic behavior as a function of the magnetic field (Figs. 3.2(b,c)) at small fields, i.e., in the region where the field can trigger a magnetization flip. For large magnetic fields, the tunneling resonances change

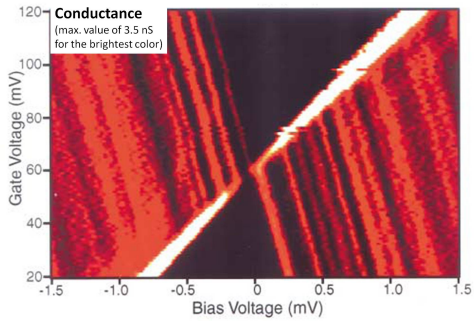

Figure 3.4: Conductance of a Co nanoparticle as a function of bias and gate voltage. The electron temperature is about 90 mK. Reprinted from Ref. [26].

monotonically with the field (Fig. 3.6), which confirms earlier theoretical suggestions [27, 28] that it is the minority-spin electrons that dominate tunneling through a ferromagnetic nanoparticle and that the total spin will increase when an electron is removed from the nanoparticle, due to a large DOS for minority electrons and strong exchange.

3.1.2 Magnetic nanoparticle – Hamiltonian

The choice of our model is motivated by the microscopic analysis of Ref. [29], where the explicit derivation of the exchange field-fluctuation propagator allows one to determine the elementary excitations (Stoner particle-holes and spin waves) of a magnetic nanoparticle. For a small nanoparticle, one finds one isolated spin collective mode ω_0 below the lowest particle-hole excitation energy, which corresponds to the spatially uniform $q = 0$ spin wave (see Chapter 1). For a large nanoparticle, there is a quasi-continuum of particle-hole excitations, in the region of which lies the uniform spin wave. In the nanoparticles investigated in Refs. [25, 26] there occur interactions between particle-hole excitations and spin-wave modes, both uniform and nonuniform ($q \neq 0$). If a particle-hole excitation of energy $\varepsilon_{ab} = \xi_a - \xi_b$, close in energy to a spin collective mode ω, interacts with

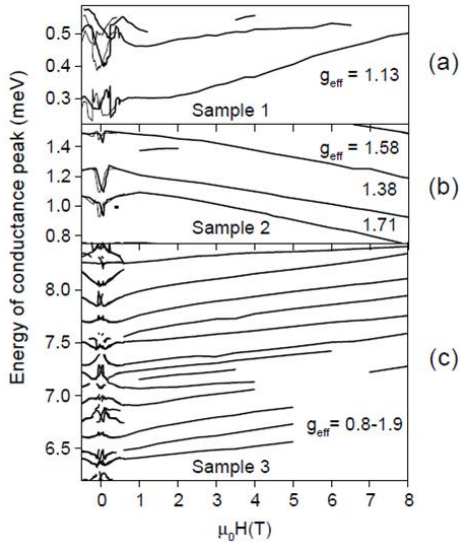

Figure 3.5: Magnetic-field dependence for the conductance resonances in Ref. [25]. Note the monotonic behavior at large fields $\mu_0 H = B$. Reprinted from Ref. [25].

that mode (uniform or not), the quasiparticle states a and b should in principle have opposite spins. This is so, because the coupling constant γ of the interaction between the particle-hole and magnon excitations is proportional to $|\langle b| S_x |a\rangle|$. However, since states $|a\rangle$ and $|b\rangle$ contain, due to the spin-orbit interaction, a small admixture of the other spin direction, the matrix element $|\langle b| S_x |a\rangle|$ will not vanish even if $|a\rangle$ and $|b\rangle$ have the same spin. The electron-magnon coupling boils down ultimately to the exchange interaction, which conserves spin.

We assume that the isolated nanoparticle can be represented by a single particle-hole excitation (two electronic states), a magnon, and an interaction thereof, according to the following Hamiltonian

$$H_d = \sum_{i=a,b} \varepsilon_i c_i^\dagger c_i + \omega \beta^\dagger \beta + \gamma \left(c_a^\dagger c_b \beta^\dagger + c_b^\dagger c_a \beta \right) + U \hat{n} \left(\hat{n} - 1 \right), \qquad (3.1)$$

where $c_i^\dagger$ (c_i) with $i = a, b$ creates (annihilates) the electronic level of energy ε_a

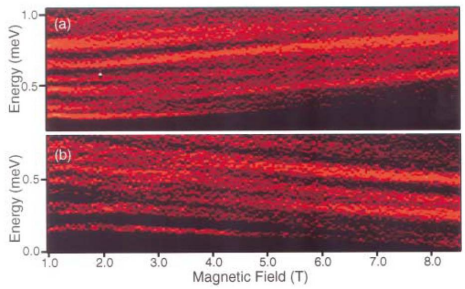

Figure 3.6: Conductance of the Co nanoparticle in Fig. 3.4 as a function of the magnetic field, for high fields. Note the monotonic behavior. (a) $V_{\rm g} = 20$ mV, (b) $V_{\rm g} = 125$ mV. Reprinted from Ref. [26].

(ε_b), with $\varepsilon_a < \varepsilon_b$. The Bose operators $\beta^\dagger$ and β describe a magnon of energy ω. All the energies below are measured in the units of the mean-level spacing $\delta \equiv \varepsilon_a - \varepsilon_b$ (the particle-hole excitation energy). The third term in Eq. (3.1) can be viewed as a pair of vertices (see Fig. 3.7) that describe an electron scattering from the electronic state a (b, respectively) to the state b (a) while absorbing (emitting) a magnon of energy ω. The coupling strength γ is treated as a phenomenological parameter; $\gamma \sim \omega$ stands for strong coupling. An interaction term similar to ours has been used in investigating magnon-assisted transport in ferromagnetic tunnel junctions [30]. The last term in Eq. (3.1) is the usual charging term, which enters when both electronic levels are occupied, $\langle \hat{n} \rangle = 2$.

The Hamiltonian (3.1) can be solved exactly. For $n = 0$ and $n = 2$, the energy spectrum is

$$\varepsilon_m^n = m\omega + \frac{n}{2}\left(\varepsilon_a + \varepsilon_b + 2U\right), \tag{3.2}$$

where m stands for the number of magnons. For $n = 1$, the spectrum becomes more complicated and splits into two subspaces $|\pm, k\rangle$ with energies:

$$\varepsilon_k^{\pm} = \varepsilon_k^0 + \varepsilon_{\rm av} \pm \frac{1}{2}\sqrt{\varepsilon_{\rm res}^2 + 4\gamma^2(k+1)}, \tag{3.3}$$

where $\varepsilon_{\rm res} \equiv (\varepsilon_b - \varepsilon_a) - \omega = \delta - \omega$ and $\varepsilon_{\rm av} = \frac{1}{2}\left(\varepsilon_a + \varepsilon_b + \omega\right)$. Besides the states

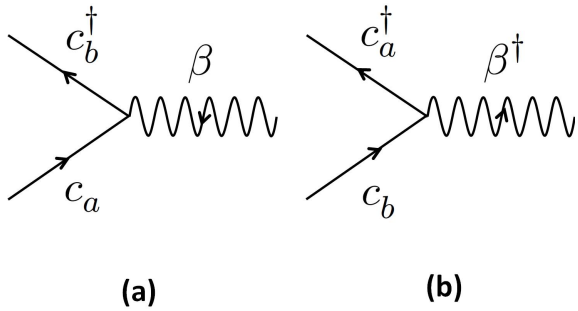

Figure 3.7: (a) Electron scattering from state a to state b associated by the absorption of a magnon. (b) Scattering from b to a with the emission of a magnon.

$|\pm, k\rangle$ there is also the state $|1_a, 0\rangle$, with energy ε_a, which forms a decoupled one-dimensional subspace in the $n = 1$ sector of the Fock space.

3.1.3 Transport calculation

We now apply the obtained spectrum of energy levels to the master-equation scheme of Chapter 2, which is appropriate when we assume the nanoparticle to be weakly coupled to the two external metal leads (left L and right R). We assume further that our double junction is symmetric with $\Gamma_{\rm L} = \Gamma_{\rm R} = \Gamma$ and $\mu_{\rm L} = -\mu_{\rm R} = V/2$, where V is the bias voltage across our SET. The dc-current I and the differential conductance $\mathrm{d}I/\mathrm{d}V$ are plotted in Figs. 3.8 and 3.9 for different γ-coupling regimes.

First, we consider coupling the p-h excitation to the uniform ($q = 0$) spin-wave mode. The case $\omega = 0.1\delta$, plotted in Fig. 3.8, pertains to this situation, as $\delta \sim 1$ meV for nanoparticles in Refs. [25, 26], and $\omega \sim 0.1$ meV. We notice that increasing the value of γ makes the extremely dense conductance spectrum, which for a weak coupling consists of two clusters, merge into one cluster, whose individual peaks now start to become discernible. However, the mean-level spacing between the peaks is $\approx 0.05\delta$, much smaller than the experimentally observed

resonance spacing 0.2δ. Therefore we conclude that such a large density of resonances, caused by an unrealistically strong coupling ($\gamma = 2\omega$) is *not* the one observed experimentally.

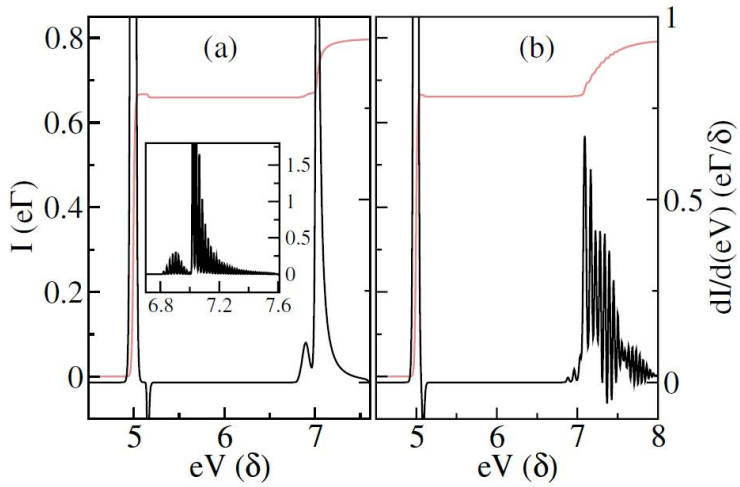

Figure 3.8: Transport in a magnetic nanoparticle with electron-magnon coupling: Current and differential conductance versus bias voltage V for $\omega = 0.1\delta$. (a) The electron-magnon coupling strength is $\gamma = 0.1\delta$, (b) $\gamma = 0.2\delta$. The temperature T is set equal to 0.005δ, except in the inset, where it is equal to 0.001δ.

Let us now investigate coupling to a nonuniform spin-wave mode (Fig. 3.9). The energy of the first nonuniform mode is $\omega \approx 1$ meV for a 4-nm Co nanoparticle, which is approximately equal to δ [25]. For a weaker coupling we have again two sets of resonances (this time discernible at a very low temperature, $T = 0.005\delta$) (Fig. 3.9(a)) that merge when the coupling increases (Fig. 3.9(b)). The resonance spacing is now $\approx 0.2 - 0.5\delta$, which is one of the characteristic features observed experimentally (Figs. 3.3 and 3.4).

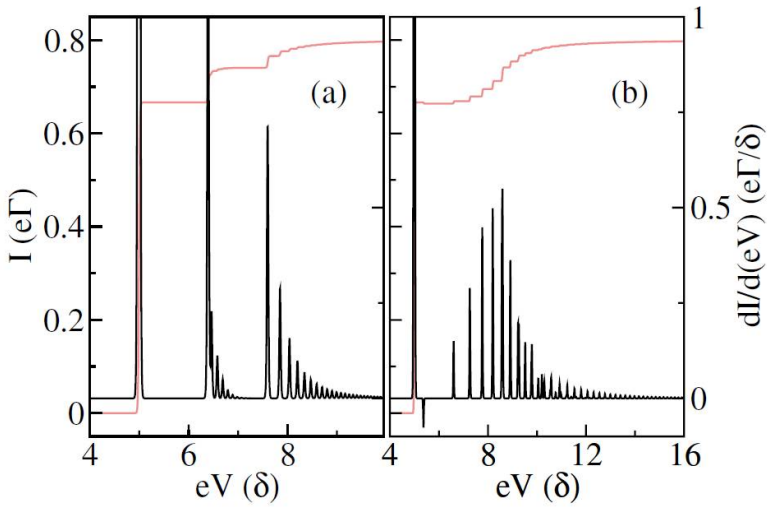

Figure 3.9: Transport in a magnetic nanoparticle with electron-magnon coupling. Current and differential conductance versus bias voltage V for $\omega = \delta$. (a) $\gamma = 0.3\delta$, (b) $\gamma = 0.8\delta$. The temperature T is in both cases set equal to 0.005δ.

3.1.4 Magnetic-field dependence

In this subsection we discuss how the resonance spectrum depends on the magnetic field. In our analysis we assume that the two bare electronic states $|1_a, 0\rangle$ and $|1_b, 0\rangle$ are of a predominantly minority-spin character. Our assumption is justified by the fact that minority electrons dominate tunneling transport in ferromagnetic grains [26–28]. In the region of small fields B (below the switching field), where the magnetic moment of the grain is close to a reversal, the energies of the grain fluctuate randomly [31, 32] and will give a quasi-random dependence of conductance resonances on the field. After the reversal, at larger fields, we obtain a monotonic linear dependence on the field (Fig. 3.10). The slopes of the resonance energies have the same sign (positive), like in the experiment [26], which is a reflection of the assumed spin character of the bare electronic levels.

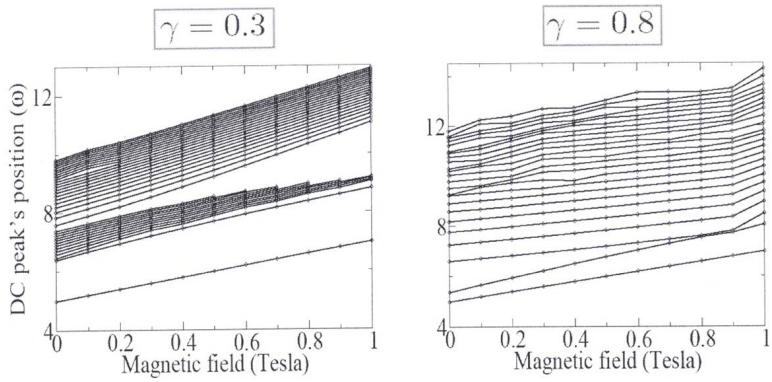

Figure 3.10: Transport in a magnetic nanoparticle with electron-magnon coupling. Magnetic-field dependence of the conductance resonances at high fields for two values of the coupling constant: $\gamma = 0.3$ and 0.8. Note the monotonic behavior.

3.2 Molecular magnets

Another, and even more promising in terms of applications and basic research, example of nanomagnets are single-molecule magnets (SMM) [33]. SMMs are molecules that possess a magnetic moment which is at least several times larger than that of a single electron. Interestingly, SMMs manifest a purely quantum phenomenon of magnetic-moment tunneling at the level of macroscopic experiments [34–37]. A prototypical example of an SMM is the Mn_{12}-acetate, which is made of 12 Mn atoms that are interconnected with organic ligands (Fig. 3.11). The Mn ions contribute to the high value of the magnetic moment ($S = 10$). The Mn_{12}-acetate has a long relaxation time (of the order of months), and is therefore particularly suitable for SET studies that intend to capture the magnetic properties of the molecule.

Indeed, the main objective of the work presented in this section was to perform a transport calculation in the limit of weak coupling on a SET with Mn_{12} as its

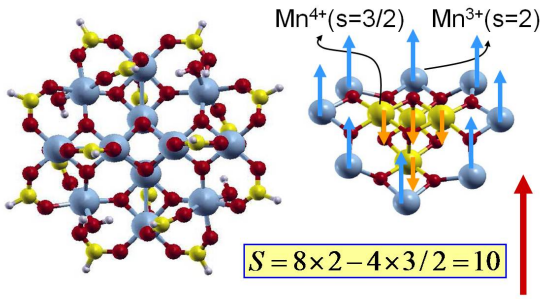

Figure 3.11: Structure of the center of the Mn_{12}-ac molecule; the Mn atoms are in blue on the left, and in blue and yellow on the right. Eight Mn^{3+} ($s = 2$) ions surround the four Mn^{4+} ions ($s = 3/2$) of the molecule core. The total spin becomes $S = 10$.

central island. As a result, we find that the spatial part of the many-body wave functions of the Mn_{12} molecule as well as the energy splitting of these many-body states strongly affect the electronic transport and can lead to strong negative differential conductance (NDC).

This section begins with a short summary of two important SET experiments with a Mn_{12} SMM as a central island [38, 39]. Then, I present briefly the spin density-functional theory (SDFT) that yields the many-body spectrum of the Mn_{12} molecule. Finally, the transport calculation follows together with a discussion of the results.

3.2.1 Motivation – experiments

As of now, two groups have carried out SET measurements on an individual Mn_{12} SMM [38, 39]. Those measurements were conducted in the weak-coupling regime, relevant to this thesis. The geometry of the samples is sketched in the inset of Fig. 3.12 and in Fig. 3.13 and has the typical SET appearance. Both experiments were done at low temperatures (3K in Ref. [39] and ≤ 0.3 K in Ref. [38]). The Mn_{12} molecule used was given by the chemical formula $Mn_{12}O_{12}(O_2C$-

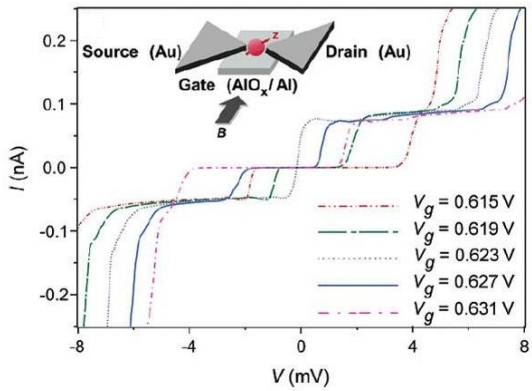

Figure 3.12: Current-voltage characteristics for several values of $V_{\rm g}$ at $T = 300$ mK for a SET with Mn_{12}-ac as a central electrode (the inset shows a cartoon of this SET). Reprinted from Ref. [38].

$R)_{16}(H_2O)_4$, where R is a generic chemical functional. The diameter of the molecule (core and ligands) varied from ~ 3 to ~ 5 nm, depending on R. The connection to the external leads (made of Au in Ref. [39] and Al in Ref. [38], respectively), and thus to the SET as such, seems to have been under better control in Ref. [39]. The external ligands served as tunneling barriers between the core of the molecule and the external metallic electrodes. In both experiments, Coulomb-blockade-like conductance resonance spectra were measured as a function of the gate and bias voltages (Figs. 3.12 and 3.14). In Ref. [38] also a magnetic-field effect on the conductance was established (Fig. 3.15).

Heersche *et al.* [39] found current suppression and NDC (Fig. 3.14). The focus of the other experiment [38] was on the magnetic-field dependence of the conductance spectrum (Fig. 3.15). The molecule states were found to be nondegenerate at $B = 0$, and depended nonlinearly on B. Surprisingly, no hysteresis in the electron tunneling spectrum was observed, which differs from observations in Mn_{12} bulk crystals [35, 36, 40, 41].

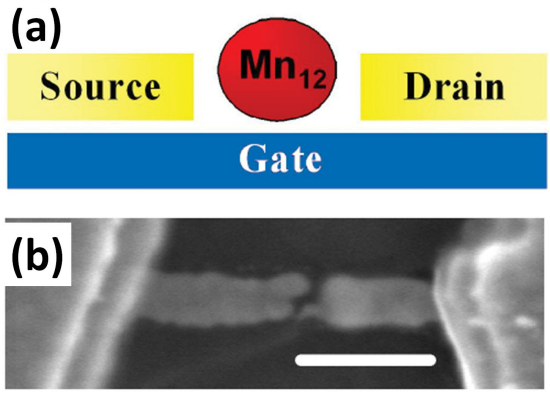

Figure 3.13: (a) SET with a Mn_{12} molecule as a central electrode. (b) SEM image of the SET, the contact gap is not discernible. Scale bar's length is 200 nm. Reprinted from Ref. [39].

3.2.2 Mn_{12} molecule. Spin model

Mn_{12}-ac is a prototypical SMM thanks to its large magnetic moment (with large spin $S = 10$), high magnetic anisotropy of essentially uniaxial character ($\sim$ 70 K [42, 43]), and long magnetic-moment relaxation time (of the order of months).

The core of Mn_{12} consists of four Mn^{4+} ions ($s = 3/2$) and is surrounded by a crown of eight Mn^{3+} ($s = 2$) ions, as it is shown in Fig. 3.11. The spins of these two species of Mn ions are oriented in an antiparallel fashion, leading to an overall ferrimagnetic configuration of the magnetic ions, with the total spin $S = 8\times 2 - 4\times 3/2 = 10$, that defines the easy axis of the molecule. The exchange interaction between the Mn ions is very strong, which gives a very robust $S = 10$ molecular magnet.

The first, and in many cases very accurate (due to the high symmetry of the molecule), approximation to model the energy of the neutral (uncharged) Mn_{12}

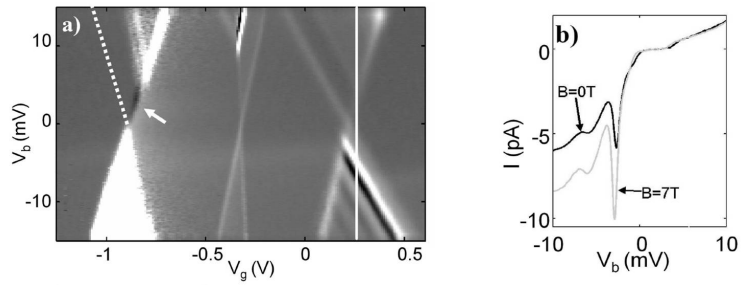

Figure 3.14: (a) Differential conductance as a function of gate and bias voltages, at 3 K. Current suppression (the dashed line indicates the suppressed conductance resonance) and negative differential conductance (NDC) (black lines) are observed. (b) Current-voltage characteristics for two magnetic fields. Note the NDC dips. Reprinted from Ref. [39].

molecule is to treat it as a giant spin $S = 10$ in a magnetic field $\vec{B}$:

$$H = -DS_z^2 - g\mu_B S_z B_z, \tag{3.4}$$

where the first term is responsible for the magnetic anisotropy, and the other one is the usual Zeeman Hamiltonian that lifts degeneracy of the energy levels corresponding to opposite spin directions. For Mn_{12}, $D = 0,548$ K and $g = 1.94$ [44]. The resulting energy spectrum has a shape of a double-well potential with the anisotropy barrier that separates one well from another (Fig. 3.16(a)). The external magnetic field changes the depths of the two potential wells (Fig. 3.16(b)).

The previous theoretical models [38, 39, 45–51] that aimed at explaining the experiments described in the subsection above are largely based on the giant-spin Hamiltonian (3.4). As such, they disregard the orbital degrees of freedom and the spin-orbit interaction with their influence on the electron that tunnels into a Mn_{12} molecule. Clearly, a model that implements the orbital degrees of freedom is desired.

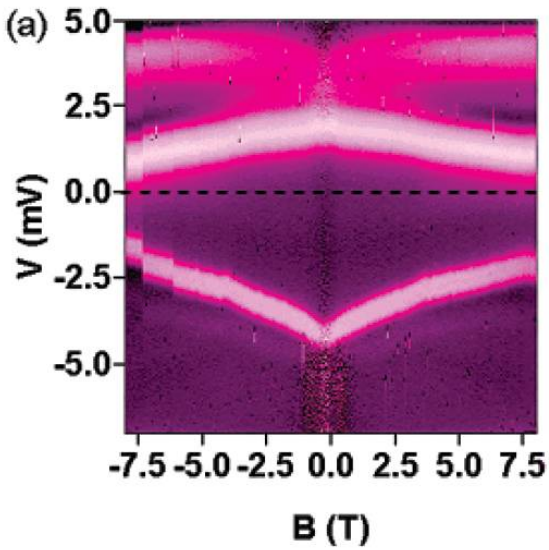

Figure 3.15: (a) Differential conductance as a function of the bias voltage and the magnetic field for a Mn_{12} SET. The color scale varies from deep purple (10 nS) to light pink (200 nS). Reprinted from Ref. [38].

3.2.3 Spin density-functional theory

In principle, the most exact way for obtaining the energy spectrum of the Mn_{12} molecule, or any other many-body system for that matter, would be to solve the appropriate Schrödinger equation. The only problem is that our molecule exceeds by far the regime where this is doable, analytically or even numerically. We are thus in need of an approximation; and the density-functional theory (DFT) [52–57] has proved to be a suitable one. The fundamental assumption of DFT is that the total nondegenerate GS energy of the system in question can be expressed as a unique functional of the electron density $\rho(\vec{r})$ [52]

$$E_{\mathrm{tot}} = T_0[\rho(\vec{r})] + \int \mathrm{d}\vec{r}\rho(\vec{r})\, v(\vec{r}) + V_{\mathrm{H}}[\rho(\vec{r})] + E_{\mathrm{xc}}[(\vec{r})], \qquad (3.5)$$

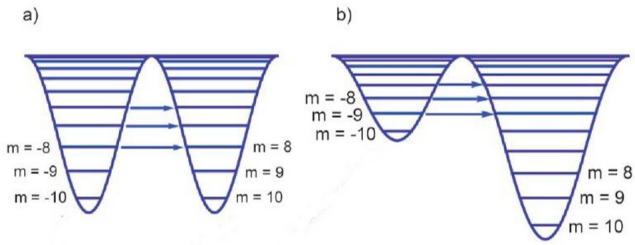

Figure 3.16: (a) In the first approximation, the Mn_{12} molecule has a double-well energy landscape (giant-spin model). Different expectation values of the S_z operator are indicated for $S = 10$. The magnetic field is zero. (b) The double well shifts when a magnetic field parallel to the molecule easy axis is applied. Adapted from Ref. [44].

where $v(\vec{r})$ describes an external potential at point $\vec{r}$, $T_0[\rho(\vec{r})]$ is the kinetic energy of a gas of noninteracting electrons the density of which is $\rho(\vec{r})$, $V_{\mathrm{H}}[\rho(\vec{r})]$ represents the energy of the average electrostatic interaction between the electrons according to

$$V_{\mathrm{H}}[\rho(\vec{r})] = \frac{1}{2}\int\int \mathrm{d}\vec{r}\,\mathrm{d}\vec{r}' \frac{\rho(\vec{r})\,\rho(\vec{r}')}{|\vec{r}-\vec{r}'|}, \tag{3.6}$$

and $E_{\mathrm{xc}}[\rho(\vec{r})]$ is the exchange-correlation energy. This E_{xc} is generally not known and needs to be approximated.

If we express the electron density in terms of single-particle orbitals [53] $\psi_{i\sigma}$ that correspond to a set of fictitious noninteracting quasiparticles, such that all the orbitals (and only those) below a certain chemical potential μ are occupied, we are left with a set of so-called Kohn-Sham equations [58]

$$\left(-\frac{\Delta}{2} + v(\vec{r}) + V_{\mathrm{H}}[\rho(\vec{r})] + \frac{\delta E_{\mathrm{xc}}[\rho_\uparrow(\vec{r}),\rho_\downarrow(\vec{r})]}{\delta\rho_\sigma(\vec{r})}\right)\psi_{i\sigma} = \varepsilon_{i\sigma}\psi_{i\sigma}, \tag{3.7}$$

where

$$\rho(\vec{r}) = \rho_\uparrow(\vec{r}) + \rho_\downarrow(\vec{r}) \sum_{i,\sigma} \theta(\mu - \varepsilon_{i\sigma}) |\psi_{i\sigma}|^2 . \tag{3.8}$$

Essentially, we have now replaced a system of interacting electrons with a system of noninteracting particles in an external field. The only unknown is still E_{xc}. One

can account for it accurately by using one of the available approximations, e.g., the local spin-density approximation (LSDA) or the generalized gradient approximation (GGA) [58].

One, particularly important, numerical implementation of DFT, the results of which have been used as a starting point for the transport calculations in Mn_{12} within this thesis, is the Naval Research Laboratory Molecular Orbital Library (NRLMOL) [59–68], a program package developed by Pederson, Jackson and Porezag. In this package, one expands the molecular orbitals in terms of linear combinations of Gaussian functions which center at the atomic sites of the molecule. Then, the Kon-Sham equations (3.7) are solved self-consistently, with the assumption of one of the many available LSDA or GGA functionals. One can also determine the forces acting on all the atoms and, in this way, the equilibrium geometry of the system [58]. Once the Kohn-Sham wave functions and the geometry are established, many physical observables can be calculated, e.g., the electron density of states, magnetic moments, charge states or magnetic anisotropy energies.

An important interaction in magnetic systems is the spin-orbit coupling. Its usual form (1.7) is exact only for electrons in a single-center system with a central electrostatic potential. For multi-center systems, such as our Mn_{12}, a Cartesian representation turns out to be more adequate:

$$H_{\mathrm{s-o}}\left(\vec{r},\vec{p},\vec{S}\right) = -\frac{1}{2c^2}\vec{S}\cdot\vec{p}\times\nabla\Phi\left(\vec{r}\right), \tag{3.9}$$

where Φ is the Coulomb potential, $\vec{p}$ the linear momentum of the electron, and $\vec{S}$ its spin. Spin-orbit coupling in this form has recently been used by Pederson and Khana [69, 70] for accounting for second-order anisotropy energies. If we expand the Kohn-Sham orbitals as a linear combination of a basis set [58] according to

$$\psi_{is}\left(\vec{r}\right) = \sum_{j\sigma} c_{j\sigma}^{is}\varphi_j\left(\vec{r}\right)\chi_\sigma\,, \tag{3.10}$$

with $\varphi_j\left(\vec{r}\right)$ and χ_σ being the orbital and spin components of the basis wave functions, respectively, we obtain the following expression for the $H_{\mathrm{s-o}}$ matrix ele-

ments

$$\begin{aligned} H_{\mathrm{s-o}}^{j\sigma k\sigma'} &= \langle\varphi_j\chi_\sigma|\, H_{\mathrm{s-o}}\left(\vec{r},\vec{p},\vec{S}\right)|\varphi_k\chi_{\sigma'}\rangle \\ &= -i\,\langle\varphi_j|\, V_x\,|\varphi_k\rangle\,\langle\chi_\sigma|\, S_x\,|\chi_{\sigma'}\rangle\,, \end{aligned} \tag{3.11}$$

where V_x is defined as

$$\langle\varphi_i|\, V_x\,|\varphi_j\rangle = \frac{1}{2c^2}\left(\left\langle\frac{\mathrm{d}\varphi_j}{\mathrm{d}z}\right|\Phi\left|\frac{\mathrm{d}\varphi_k}{\mathrm{d}y}\right\rangle - \left\langle\frac{\mathrm{d}\varphi_j}{\mathrm{d}y}\right|\Phi\left|\frac{\mathrm{d}\varphi_k}{\mathrm{d}z}\right\rangle\right). \tag{3.12}$$

Hence, the cumbersome calculation of $\nabla\Phi$ matrix elements is replaced by a simpler task of computing gradients of the basis functions. This method of including spin-orbit interaction, and by that the orbital degrees of freedom, answers to the desire expressed in the previous section.

$\mathbf{Mn_{12}}$ calculation

By following the SDFT method outlined above, we solve the set of Kohn-Sham equations for different charge systems of the Mn_{12} molecule (neutral, cationic and anionic). We impose a constraint that the expectation value of the system's total spin $\left\langle\vec{S}\right\rangle$ be quantized along the axis determined by two angles θ and ϕ. The solution is a set of single-particle orbitals φ_k. Then we construct approximate many-body wave functions for the ground and low-lying excited states as single Slater determinants of the spin orbitals φ_k

$$\left|Q,\theta,\phi,\vec{S};k_1,k_2,\ldots k_{N_Q}\right\rangle \equiv \left|\varphi_{k_1},\varphi_{k_2},\ldots\varphi_{k_{N_Q}}\right\rangle, \tag{3.13}$$

where N_Q is the number of electrons for a given charge state Q. The expectation values of S_z are close to the values of M in the giant-spin model for θ satisfying $S\cos\theta = M$. Therefore, we obtain $2S+1$ nearly orthonormal linearly independent many-body Slater determinants with $\langle S_z\rangle \approx M$, where $M = -S, -S+1, \ldots S-1, S$. We call this set of many-body states a *spin multiplet*.

The SDFT calculation yields, for different Q, such total-system quantities as the spin, GS energy, HOMO (highest occupied molecular orbital) and LUMO

(lowest unoccupied molecular orbital) levels, and magnetic anisotropy energy. The obtained values are summarized in Table 3.1. These numbers are the first ab-initio results for the charged Mn_{12} molecule; they are discussed in more detail in papers II and III. Here we note only the increase of the total spin due to adding a *delocalized* electron. The energies of the spin multiplets (Fig. 3.17) and overlaps between spin multiplets that correspond to different charge states Q (Fig. 3.18) are used later for transport calculations (cf. next section). Each charged state has several excited low-lying spin multiplets, which ultimately stems from the quasidegeneracy around the HOMO and LUMO levels of the neutral molecule. The same reason leads to the enhanced MAE (Table 3.1) when a delocalized electron is added to the neutral molecule.

Table 3.1: The GS properties from DFT: spin, energy, and magnetic anisotropy energy as a function of charge.

Charge state	Charge Q	Spin	Energy (eV)	MAE (K)	MAE (meV)
Anion	-1	21/2	-3.08	137	11.8
Neutral	0	20/2	0.00	55	4.7
Cation	1	19/2	6.16	69	5.9

3.2.4 SET with Mn_{12}

The spin-multiplet energy spectra (Fig. 3.17) and the transition rates between the spin multiplets of different charge (Fig. 3.18) are now implemented into the general SET scheme (see Chapter 2) for a quantum dot with a discrete set of energy levels, weakly coupled to two external metallic leads and to a gate electrode. When a finite bias voltage is applied across such a double junction, current flows, as plotted in Fig. 3.19 for two values of the gate voltage: $V_{\rm g} = -20$ V and $V_{\rm g} = 10$ V. Figure 3.20 shows the differential conductance $G = {\rm d}I/{\rm d}V_{\rm b}$ as a function of $V_{\rm b}$ and $V_{\rm g}$. The numerical calculations are done at zero temperature.

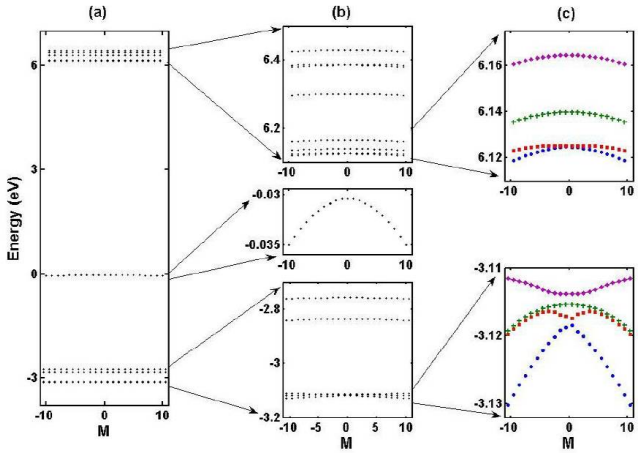

Figure 3.17: SDFT results for the Mn_{12}-ac molecule. (a) The energy spectrum of the three charge states plotted in the same energy scale. (b) A zoom-in of the spectra for the cation, neutral molecule and anion (from top to bottom). (c) A zoom-in of the lowest-lying multiplets for the cation (top) and anion (bottom).

The molecule couples to the two leads with equal strength (symmetric double junction); the gate capacitance is equal to $1/20$ of the total capacitance of the system. Three Coulomb-blockade stability diamonds are visible, corresponding to the three charge states $Q = -1, 0, 1$, where transport is blocked. The lines that border each diamond correspond to transitions between the GSs of two contiguous charge states. In the region indicated by $(-1, 0)$, the current flows due to transitions between anionic and neutral states. In the region $(0, +1)$ transitions between neutral and cationic states occur, and in the region $(-1, 0, +1)$, all the three charge states are present. The additional lines, parallel to the lines of GS-GS transitions are due to transitions between excited states. In Fig. 3.20 we can also see two dark lines, indicated by white arrows, that correspond to a decrease in the current while $V_{\rm b}$ is increased (NDC). NDC in a $\rm Mn_{12}$-SET has been observed experimentally [39].

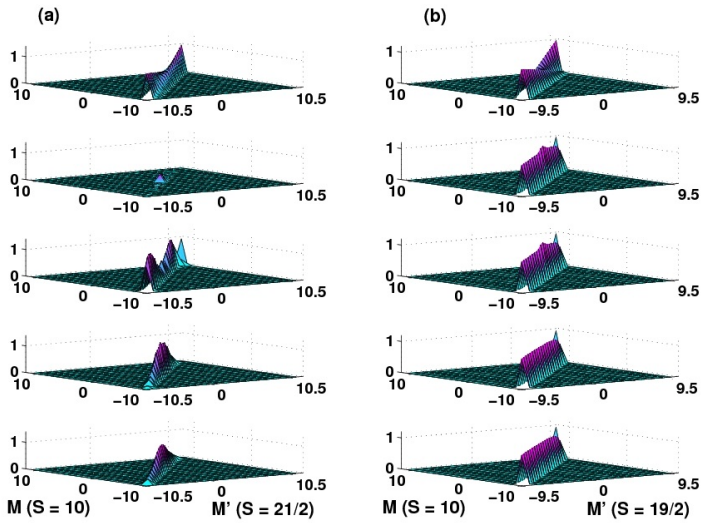

Figure 3.18: SDFT results for the Mn_{12}-ac molecule. Matrix elements for transitions between neutral and anionic (a) and cationic (b) charge states. From top to bottom: giant-spin model, transitions from the neutral GS spin multiplet to the anionic (a) and cationic (b) GS spin multiplets, transitions from the neutral GS spin multiplet to the anionic (a) and cationic (b) first, second and third excited spin multiplets.

In order to see exactly how the orbital degrees of freedom reveal themselves in the SDFT-based calculation, we plot $I(V)$ characteristics for a uniaxial giant-spin model (3.4) (SM) in Fig. 3.19. We note that the blue $I(V)$ curve ($V_{\rm g} = -20$ V) starts off much more rapidly for SM (dashed line) than for SDFT (solid line). In order to understand why this happens, it is instructive to take a look at the transition overlaps (Fig. 3.18(a)) between the neutral and anionic GS spin multiplets, both for SM and SDFT. We see from Fig. 3.18(a) (the two plots on the top) that the two overlaps differ substantially. The SM overlap connects well the GS levels (largest $|M|$ and $|M'|$) of the neutral and anionic GS spin multiplets, while the SDFT overlap does *not*. This lack of connection between the GS levels for

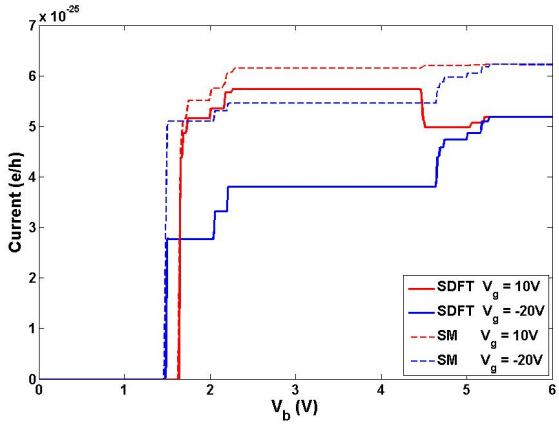

Figure 3.19: Theoretical current-voltage characteristic for the Mn_{12} SET. The solid (dashed) lines correspond to the calculation done within the SDFT (SM) approach. The blue (red) line represents the $I(V)$ curve for $V_g = -20$ V ($V_g = 10$ V). The double junction is symmetric, and the gate capacitance is 1/20 of the total capacitance, the temperature is zero.

SDFT leads to a current suppression at the onset of transport (solid blue line in Fig. 3.19). The negligibility of this connection is also responsible for the drop in current visible in the solid red $I(V)$ curve ($V_g = 10$ V). When this drop happens, the anion-to-neutral transport channel opens; the GS multiplet of the anion becomes occupied, but since it is only weakly connected to the neutral GS multiplet, the system gets trapped in the GS anion multiplet, and that leads to the noted drop in current or, in other words, to a NDC dip (see Fig. 3.20). From this difference between a purely-spin SM and the SDFT-based calculation that includes the spatial degrees of freedom, we draw the conclusion that the spatial selection rules can override the spin selection rules and affect transport dramatically, leading to current suppression and NDC. Otherwise, we note that the conductance resonances representing transitions between spin multiplets of different charge are separated by voltages that correspond to the energies of the order of MAE.

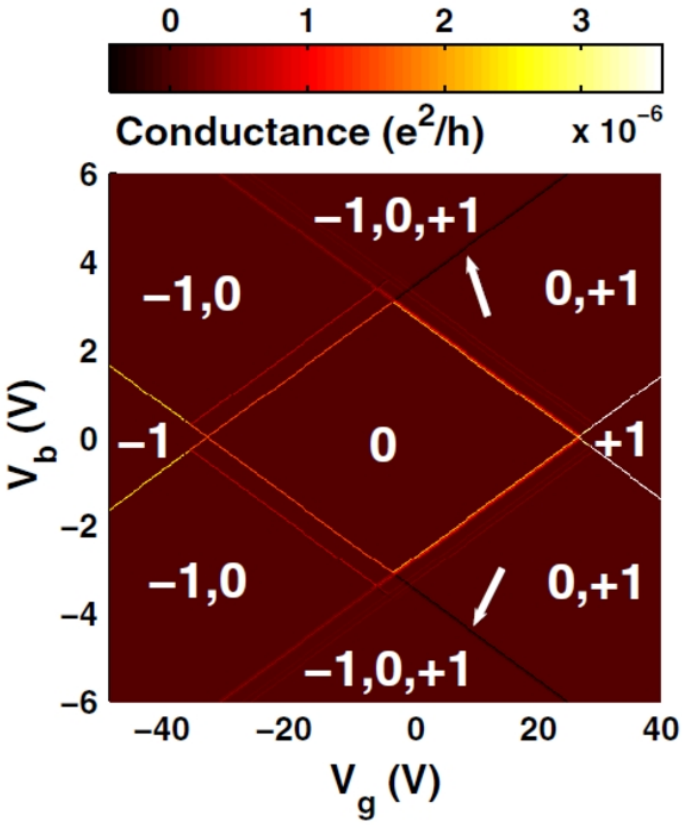

Figure 3.20: Differential conductance for the Mn_{12} SET as a function of bias and gate voltages, calculated within the SDFT approach. Numbers $-1, 0, +1$ denote the excess charge on the molecule in units of e and label regions of Coulomb blockade; in regions $(-1, 0)$, $(0, +1)$ and $(-1, 0, +1)$ transport is possible via transitions between charge states given in the parentheses. The double junction is symmetric, and the gate capacitance is 1/20 of the total capacitance; the temperature is zero. The two white arrows indicate the transition lines at which we observe negative differential conductance.

4

Magnetoresistance effects in ferromagnetic SETs

4.1 Ferromagnetic single-electron transistor (F-SET)

After studying single-electron tunneling spectroscopy in quantum-dot-like systems with a discrete spectrum and a net magnetic moment, we switch now our attention to another class of systems, where spin-dependent electron transport appears: the ferromagnetic single-electron transistor (F-SET). An F-SET is defined as a double-junction device, the external electrodes of which are ferromagnetic (F) and possess a net magnetization. The central island can be made of a ferromagnetic (F) or normal (N) metal: we have an F-SET of either F/I/F/I/F or F/I/N/I/F type (Fig. 4.1). 'I' denotes here an insulating interface (it is usually omitted in this

notation, though, so we write F/F/F or F/N/F instead), typically an oxide, between the central and external electrodes; this interface serves as a potential barrier for the tunneling electrons. The energy spectrum of the island is quasi-continuous, and the only discretization of the transport comes from the charging effects.

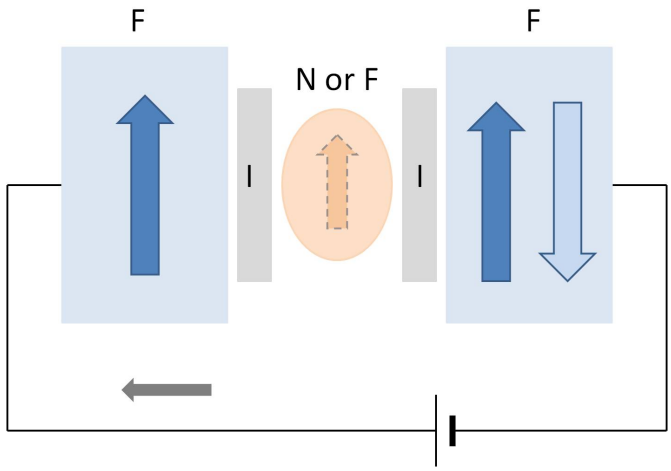

Figure 4.1: A schematic of a collinear F-SET: the two external leads are ferromagnetic (F), and the central island can be made either of a normal metal (N) or a ferromagnet (F); 'I' stands for the insulating tunneling barrier. The magnetic moments of the three (or two) electrodes are parallel or antiparallel to each other.

The resistance of F-SETs depends on the relative orientation of the magnetization of the electrodes; hence the second section is devoted to the phenomenon of magnetoresistance and emphasis is put on the so-called tunneling magnetoresistance (TMR), a phenomenon of utmost importance for the whole chapter. Sections 3 and 4 deal with single-electron tunneling and TMR in Ni/Au/Ni and Co/Ni/Co F-SETs, respectively. The experiments done by RuiSheng Liu *et al.*, central to our theoretical work, are presented, together with the main results and a theoretical analysis.

4.2 Tunneling magnetoresistance

The electron spin remains undetectable unless in the presence of an external magnetic field or the field produced by the material in which the electron is placed (magnetization). The static magnetic properties of solid matter affect the electron spin and hence the dynamics of the electron motion, in particular, electronic transport. This effect, known as magnetoresistannce (MR), can be expressed quantitatively as the relative change ΔR of the system resistance R due to the change of magnetic field or magnetization orientation

$$\mathrm{MR} = \frac{\Delta R}{R}. \tag{4.1}$$

The value of this ratio is typically expressed in percents. The magnetoresistive effect which occurs in tunneling devices is called tunneling magnetoresistance (TMR), and ΔR results from rearranging the relative orientation of the magnetic moments of the electrodes in a given F-SET. TMR is an outcome of spin-dependent tunneling processes and can be up to about 50% in room temperatures [71]. In our treatment we assume that the electron spin does not flip during a tunneling event.

In order to understand the basic physics of TMR, it is sufficient to limit oneself to the study of tunneling through a single magnetic junction, such as the one in Fig. 4.2, where we have two ferromagnetic layers FM1 and FM2 separated by a thin layer of an insulator (i.e., an F/I/F junction). The resistance for the parallel alignment of the two magnetizations, R_{p}, is smaller than the one for the antiparallel configuration, R_{ap}. This difference originates from the exchange shift between the DOS of the spin-minority and spin-majority electrons, as explained in Fig. 4.3. In the regime of sequential tunneling and by virtue of Fermi's golden rule, we can write the current through F/I/F as proportional to the spin-dependent DOS of states $\rho_{1\sigma}$ in FM1 and $\rho_{2\sigma}$ in FM2 ($\sigma = \uparrow$ or $\downarrow$)

$$I_{\uparrow\uparrow} = \rho_{1\uparrow}\rho_{2\uparrow} + \rho_{1\downarrow}\rho_{2\downarrow} \tag{4.2}$$

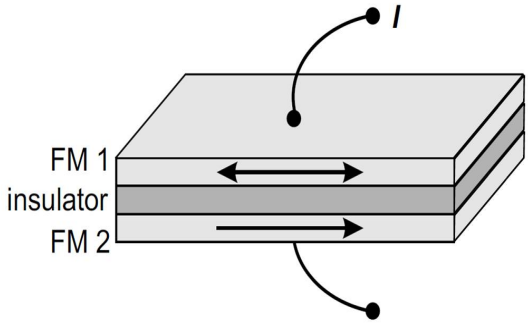

Figure 4.2: A ferromagnetic thin film separated by a layer of an insulating material forms a single tunneling junction where TMR is observed. Reprinted from Ref. [71].

and

$$I_{\uparrow\downarrow} = \rho_{1\uparrow}\rho_{2\downarrow} + \rho_{1\downarrow}\rho_{2\uparrow}, \tag{4.3}$$

where $\uparrow\uparrow$ ($\uparrow\downarrow$) denotes the parallel (antiparallel) alignment, and we assumed spin conservation at tunneling. We used here also Mott's idea of a two spin channel model, in which the majority and minority spins tunnel independently of each other, as if there were two transport channels (resistors) connected in parallel, as in Fig. 4.4. Looking at Fig. 4.3, we conclude that, since $\rho_\downarrow > \rho_\uparrow$ at the Fermi level, the current $I_{\uparrow\uparrow}$ will be larger than $I_{\uparrow\downarrow}$.

The magnitude of TMR for our F/I/F interface is defined by

$$\mathrm{TMR} = \frac{R_{\uparrow\downarrow} - R_{\uparrow\uparrow}}{R_{\uparrow\uparrow}} = \frac{G_{\uparrow\downarrow} - G_{\uparrow\uparrow}}{G_{\uparrow\uparrow}}, \tag{4.4}$$

and will be positive in our example of an F/I/F junction; G stands for the differential conductance. Using the definition of the spin polarization $\mathcal{P}_\alpha$ in the lead α ($\alpha = 1$ or 2 labels the two leads FM1 and FM2) in Eq. (2.3), we can write

$$G_{\uparrow\uparrow} = \frac{1}{2}\left(1 + \mathcal{P}_1\mathcal{P}_2\right) \tag{4.5}$$

and

$$G_{\uparrow\downarrow} = \frac{1}{2}\left(1 - \mathcal{P}_1\mathcal{P}_2\right), \tag{4.6}$$

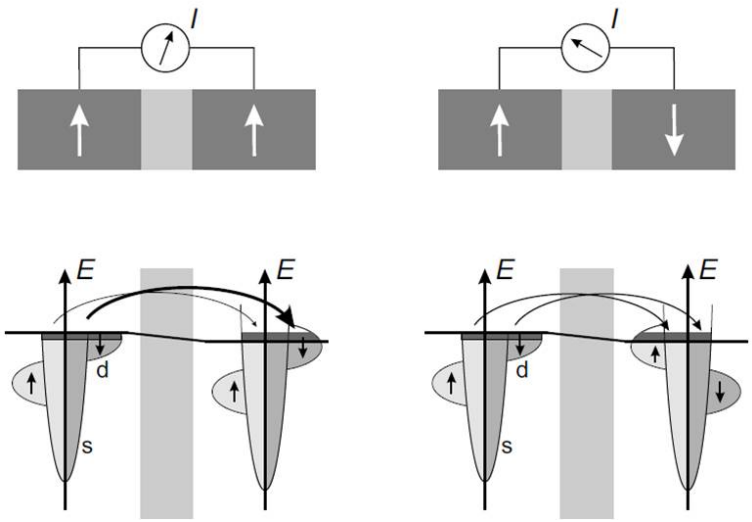

Figure 4.3: TMR results from a difference in the DOS for the two spin species. Mostly 'down' electrons tunnel from left to right. The number of empty 'down' states in the right electrode, which can become occupied by the 'down' electrons coming from the left electrode, decreases when the orientation of the magnetic moments of the two leads changes from parallel to antiparallel. Reprinted from Ref. [71].

and the TMR can be expressed as

$$\mathrm{TMR} = \frac{\Delta R}{R_{\uparrow\uparrow}} = \frac{2\mathcal{P}_1\mathcal{P}_2}{1-\mathcal{P}_1\mathcal{P}_2}. \tag{4.7}$$

This result was first derived by Jullière [72] and is generally valid for low temperatures.

For an F-SET of the form F/I/N/I/F, the same formulae as derived above apply for TMR. The situation changes when also the central island is a ferromagnet. Then, in principle, an infinite multitude of noncollinear alignments is possible. However, for us (see Section 3) three cases are of importance which can be represented pictorially as: ↑↑↑ (all the magnetic moments point in the same direction), ↑→↑ (the magnetic moments of the external electrodes are parallel to each other,

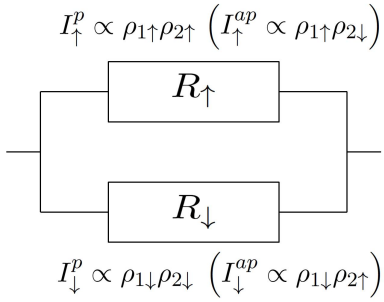

Figure 4.4: The electric current through a single ferromagnetic junction can be thought of as composed of two channels – spin 'up' and spin 'down' – that run in parallel of each other (the idea belongs to Mott). The spin components of the current, in terms of DOS for the two spin species, are noted for the two collinear configurations of the magnetizations. The indices 'p' and 'ap' stand for the parallel and antiparallel configuration of the magnetization vectors, respectively.

while that of the island is perpendicular to their direction), and $\uparrow\rightarrow\downarrow$ (the magnetic moments of the external electrodes are antiparallel to each other, and the island moment points perpendicularly to them). The differential conductance for an arbitrary angle ϑ between the magnetizations of two adjacent FM electrodes that form a single junction can be written [71] as

$$G(\vartheta) = G_0 \left(1 + \mathcal{P}_1 \mathcal{P}_2 \cos\vartheta\right), \tag{4.8}$$

where $G_0 = (G_\mathrm{p} + G_\mathrm{ap})/2$. Therefore, for the alignments $\uparrow\rightarrow$ and $\rightarrow\uparrow$ ($\downarrow$) we have within Jullière's model

$$G_{\uparrow\rightarrow} = G_{\rightarrow\uparrow(\downarrow)} = G(90^\circ) = G_0(1+0) = G_0. \tag{4.9}$$

Jullière's model describes particularly well amorphous barriers [73], for which the passing electrons have the same transmission amplitude – the assumption that is at the heart of this model.

4.3 Metallic island

When spin-polarized current enters a normal-metal island, it can create a spin imbalance on the island, so that the island gains a nonequilibrium magnetic moment. Search for this *spin accumulation*, as this phenomenon is often referred to, was the motivation for carrying out the experiment on the Ni/Au/Ni F-SET, which I describe in the following subsection. However, the measurements yielded no signature of a TMR signal, the presence of which would have indicated spin accumulation on the island due to spin injection from the ferromagnetic leads. The absence of spin accumulation is attributed to fast spin relaxation (caused by the strong spin-orbit interaction in Au), as I discuss later within this section. By doing Coulomb-blockade rate-equation calculations, we were able to find an upper-bound of several nanoseconds for the spin-relaxation time on the island. Experimentally, although the desired TMR signal was not observed, the very fabrication technique used to produce Ni/Au/Ni samples was a success as now unconventional hybrid devices could be realized with unprecedented control, including real-time tunable tunneling resistances (see Paper IV for more details).

4.3.1 Experiment on a Ni/Au/Ni SET

The F-SET composed of two Ni leads and a central nanodisk-shaped Au island was fabricated with AFM manipulation. Then, conductance measurements were carried out at $T = 1.7$ K that led to a typical (for Coulomb-blockade transport) plot as a function of the bias and gate voltages (Fig. 4.5). From the 2D conductance plot the capacitances and resistances of the junctions were determined. Later, their values were used as parameters of a theoretical simulation. The magnetic-field dependence of the conductance was also measured (Fig. 4.6). The magnetic field $\vec{B}$ was swept from -0.4 to 0.4 T in-plane, and parallel to the Ni electrodes. The study showed that the conductance was constant for the whole range of B. This indicates clearly absence of any magnetic effects in the island; in particular, there is no spin accumulation. The same conclusion can be drawn

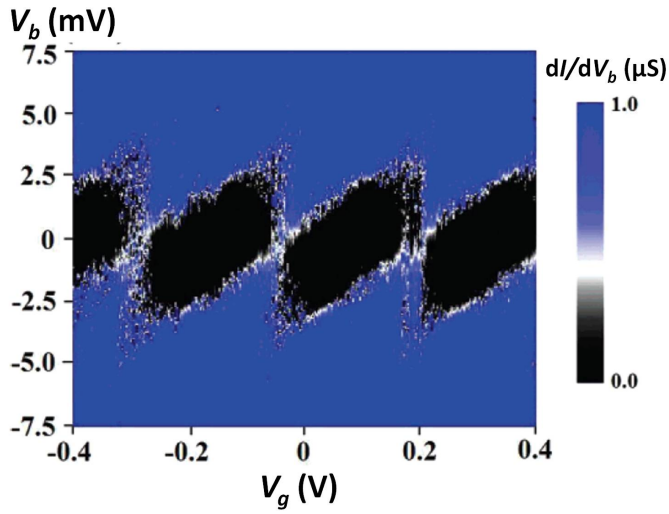

Figure 4.5: The differential conductance $\mathrm{d}I/\mathrm{d}V_\mathrm{b}$ as a function of the bias, V_b, and gate, V_g, voltages. The measurement was done at 4.2 K. The dark areas ("diamonds") correspond to the Coulomb blockade regime.

from the TMR measured as a function of the bias voltage (Fig. 4.7).

In order to exclude the influence of the quality of the magnetic tunnel junction on the lack of TMR, a single Ni/NiO_x/Ni junction was investigated. The Ni electrodes had the same spatial dimensions as those in the Ni/Au/Ni F-SET (Fig. 4.8). The magnetic sweep shows a clear maximum in TMR as the configuration switches from parallel to antiparallel; this is typical for an F/I/F junction. Thus, the magnetization alignment is controllable in Ni electrodes, and the spin injection is efficient in a single magnetic tunnel junction. It is what happens in the island that is responsible for the absence of a TMR signal in our F-SET.

4.3.2 Spin accumulation

In order to model theoretically our F-SET with two magnetic leads an a normal-metal island, we apply the theoretical machinery introduced for metallic islands

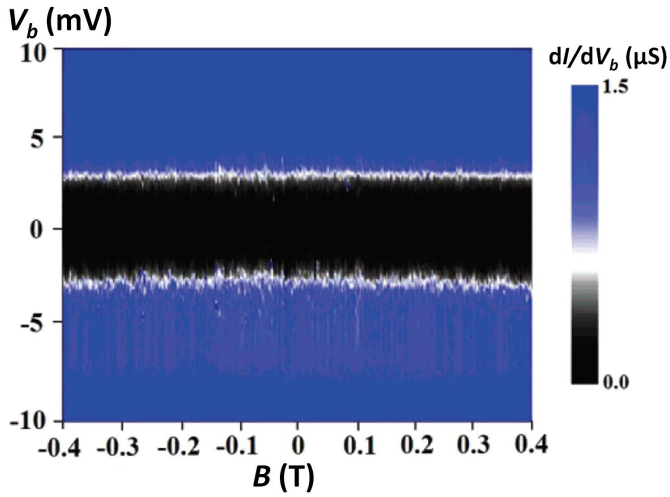

Figure 4.6: The differential conductance $\mathrm{d}I/\mathrm{d}V_\mathrm{b}$ as a function of the bias voltage, V_b, and the magnetic field B at $V_\mathrm{g} = 0$ and $T = 1.7$ K.

in Chapter 2. Since now the two external electrodes possess magnetic moments, there is an imbalance between minority and majority electrons in each of these electrodes. This imbalance leads to a possibility of spin accumulation on the island when transport is activated and lead electron spins are injected into the island. The spin accumulation translates into a nonequilibrium shift of the island Fermi energies between the two spin species. Assuming that the equilibrium DOS in the island is independent of spin [74] (which is generally true for normal metals), we can write

$$\Delta E_{\mathrm{F}\uparrow} = -\Delta E_{\mathrm{F}\downarrow} = \frac{\Delta E_\mathrm{F}}{2} \tag{4.10}$$

for the Fermi-energy shifts. We solve then the rate-equation problem (Chapter 2) by imposing the self-consistency condition on the spin polarized current (Eq. (2.28)). The iteration is cut when $I^\sigma_\mathrm{L} = -I^\sigma_\mathrm{R}$ within a desired accuracy for $\sigma = \uparrow$ and $\downarrow$. We carry out the calculation for a parallel ($\uparrow\uparrow$) and an antiparallel ($\uparrow\downarrow$) alignment of the magnetization vectors of the leads, and compute the TMR

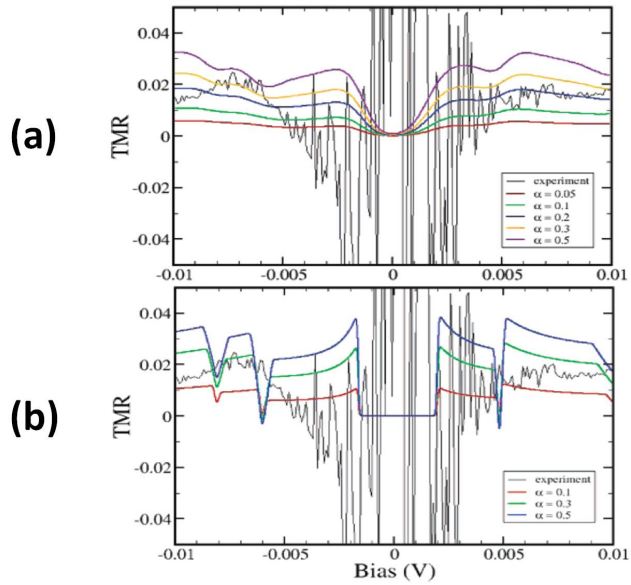

Figure 4.7: TMR as a function of the bias voltage at $T = 1.7$ (a) and 0.1 K (b), respectively. The solid black curve is the experimental result, while the color curves represent the theoretical simulations for a few values of the dimensionless spin-relaxation time α.

defined as

$$\mathrm{TMR} = \frac{I_\mathrm{p} - I_\mathrm{ap}}{I_\mathrm{ap}}. \tag{4.11}$$

We plot TMR(V) curves obtained for two temperatures $T = 1.7$ and 0.1 K in Figs. 4.7(a,b) (color lines). The parameters used in the numerical simulations were assumed to be of the same order of magnitude as those extracted from the measured Coulomb diamonds (Fig. 4.5). The capacitances are $C_\mathrm{L} = 24$ aF, $C_\mathrm{R} = 20$ aF ($C_\mathrm{L} + C_\mathrm{R} = 63.2$ aF in the experiment), $C_\mathrm{g} = 0.8$ aF (which is equal to the experimental estimate), and the resistances of the left and right tunnel junctions are assumed to be equal $R_\mathrm{L} = R_\mathrm{R} = 0.34\ \mathrm{M\Omega}$ (the experimental estimate). We note that the oscillatory character of the TMR curve is a result of spin accumulation and Coulomb blockade, and it has been seen in other experiments

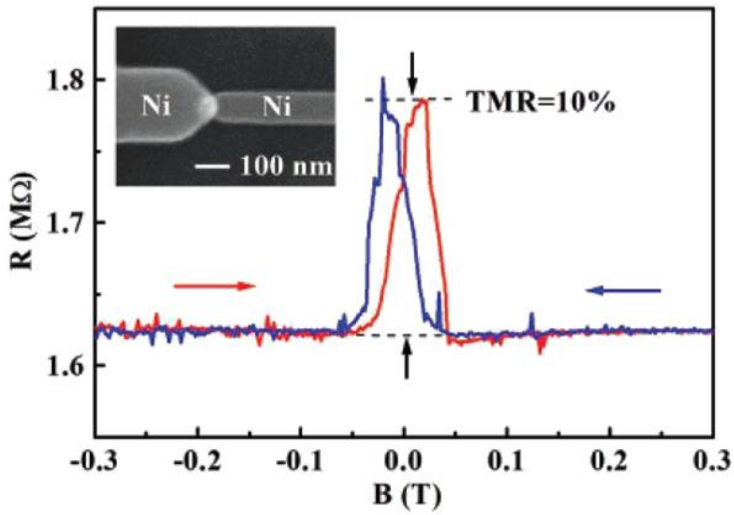

Figure 4.8: Switching behavior of a single tunnel junction between two Ni electrodes separated by NiO as a function of the magnetic field at 1.7 K. A scanning electron micrograph of the device is shown in the inset.

(magneto-Coulomb oscillations of Refs. [75, 76]). However, our experiment does not exhibit oscillations in the TMR, and the overall TMR signal is rather strongly suppressed ($\leq 2\%$ in Fig.4.7 (the experimental curve)).

These experimental observations indicate that the spin-relaxation time τ_s in the Au nanodisk is shorter than expected. Based on the comparison of the experimental and theoretical curves (Fig. 4.7(a)), we find an upper bound for τ_s. We see that the numerical result for the dimensionless $\alpha = 0.2$ fits the values of TMR best, at least at higher bias voltages. Although the fit is far from perfect, the order of magnitude is right, which allows for an estimate to be made. The dimensionless constant α is defined as

$$\alpha = \frac{\tau_s}{e^2 \rho \mathcal{V} R_{\text{total}}}, \tag{4.12}$$

where ρ is the DOS per eV and m^3 for one spin channel on the disk (i.e., assuming

a bulk normal-metal DOS, $\rho = \rho_\uparrow = \rho_\downarrow = \rho_{\mathrm{Au}}/2$). $\mathcal{V}$ is the volume of the disk and $R_{\mathrm{total}} = R_{\mathrm{L}} + R_{\mathrm{R}}$ is a sum of the bare tunnel resistances. For $\rho_{\mathrm{Au}} = 1.6 \times 10^{28}\ \mathrm{eV}^{-1}\mathrm{m}^{-3}$ (estimated for $\rho(E_{\mathrm{F}})$ in Au on the basis of the free-electron values in Ref. [5]), with the island volume $\mathcal{V} = \pi \times (15\ \mathrm{nm})^2 \times 30$ nm and the total resistance $R_{\mathrm{total}} = 0.68\ \mathrm{M}\Omega$, we have $\tau_s = 4$ ns. Given the uncertainty in the interpretation of the experimental TMR signal, it must be emphasized that this value is nothing but an upper bound for τ_s. Nevertheless, recent magnetotransport measurements on F-SETs with small Au nanoparticles do report τ_s of the order of 1 ns [77], which confirms that our numerical estimate of the spin-relaxation time is reasonable.

Spin relaxation

A few words about spin-relaxation and spin-decoherence mechanisms are in place here. Spin relaxation in matter is generally ascribed to the action of fluctuating magnetic fields [78]. These fields are usually the effective fields that result from the spin-orbit and exchange interactions [79]. Such a fluctuating magnetic field can be described by an amplitude and a correlation time τ_c during which the field is constant. If we put an electron spin in this given magnetic field of a certain random direction, the electron spin will precess around this direction with frequency ω over time τ_c. When a fluctuation happens, the magnetic field changes its direction and magnitude, which makes the spin precess about this other direction. When this repeats many times, the electron loses, in the end, its memory of the initial spin it had. If the angle of precession is small ($\omega\tau_c \ll 1$), the spin will undergo a slow angular diffusion. Otherwise, for $\omega\tau_c \gg 1$, the spin projection perpendicular to the magnetic field will vanish completely, and the parallel one will be preserved. A fluctuation in the magnetic field leads then to vanishing of the new perpendicular projection; thus the initial spin polarization gets destroyed immediately after the first change of the magnetic field.

The mechanism of spin relaxation relevant in metals such as Au is that of Elliott-Yafet [80]. Here the relaxation of conduction-electron spins takes place

through momentum scattering on phonons (at high temperatures) or impurities (at low temperatures), under the condition that the lattice potential mixes pure spin states into minority and majority states. This mixing happens by means of the spin-orbit interaction. The spin-relaxation time in bulk metals was measured to be 0.1–1 ns, typically. These values can be, however, significantly enhanced if the sample dimensions go down. The level-discretization that emerges in small systems will lead to a substantial weakening of the spin-orbit interaction. In our case of the Au nanodisk, we are still in the limit of a quasi-continuous spectrum (metallic dot), so the found upper bound of 4 ns is not surprising.

4.4 Ferromagnetic island

The last system considered in this thesis is a Co/Ni/Co F-SET whose all three electrodes (source, drain and the central, wire-like, island) are ferromagnetic. The experiment showed TMR traces with negative coercive fields, which are interpreted in terms of a switching mechanism driven by the shape anisotropy of the central elongated Ni island. A large TMR signal of about 18% decays rapidly with increasing bias voltage. This rapid drop is attributed to the bias-driven excitation of magnons in the central island and is accounted for by a bias-dependent exponential decay of the island spin polarization.

4.4.1 Experiment on a Co/Ni/Co SET

The Co/Ni/Co F-SET (Fig. 4.9) was fabricated by electron-beam lithography. The source and the drain electrodes (made of Co) have dimensions 1.5 μm $\times$ 80 nm and 800 nm $\times$ 280 nm, respectively. The central Ni island has an elongated, wire-like shape and is 20 nm wide and 150 nm long. The tunneling barriers between the electrodes are made of NiO_x. A Ni gate was also made for carrying out conductance measurements.

First, the magnetic-field dependence was measured for the F-SET resistance at 1.8 K and $V_b = 1$ mV. The magnetic field was applied in-plane, along the long

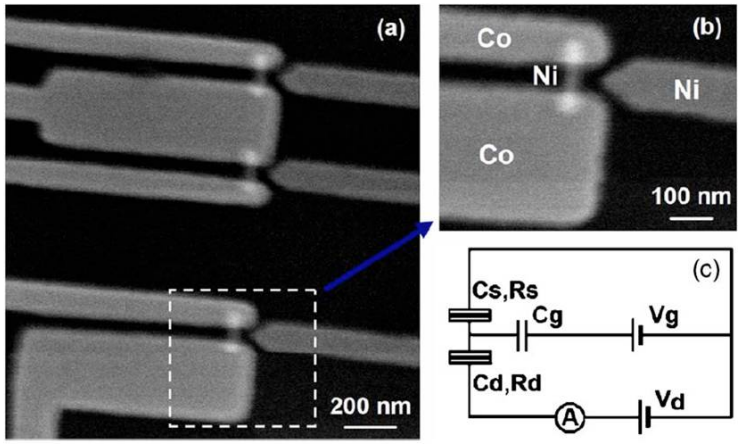

Figure 4.9: (a) Top-view SEM image of the device geometry. (b) Zoomed-in view of an isolated F-SET located inside the white rectangle in (a). (c) Circuit diagram of the connected device.

axes of the Co leads. The results are plotted in Fig. 4.10 (solid lines). As we can see, the TMR signals start off at negative fields for both sweep directions. The negative sign of the sample coercive fields originates from the geometry of the sample, in particular, from the shape anisotropy of the wire-like Ni island. The shape anisotropy makes the island magnetization align perpendicularly to the magnetic field when the field is small enough. Hence, the first (when going from the large negative field region in Fig. 4.10; at large fields the three magnetizations are parallel) switch of the magnetization configuration occurs already before $B = 0$, that is, before the coercive field for the wider Co electrode (0.13 T) is reached. Next, at $B = 0.21$ T, the narrower Co electrode switches its magnetization direction, and finally, $B = 0.3$ T is the coercive field for the Ni island. This scheme of magnetization alignment switchings was confirmed by a micromagnetic simulation within the Object Oriented Micromagnetic Framework. The results of the simulation are presented in the insets of Fig. 4.10.

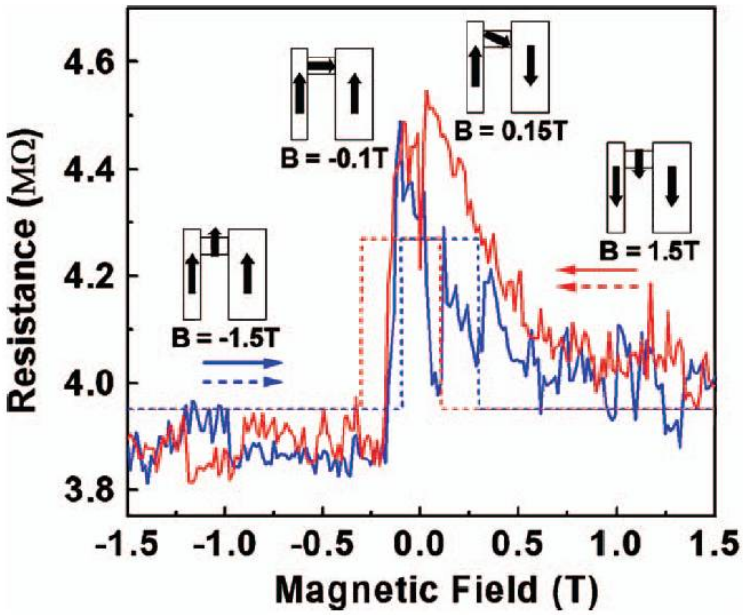

Figure 4.10: Magnetic-field dependence of the total resistance of the double junction, at $T = 1.8$ K and $V_{\rm b} = 1.5$ mV. The solid (dashed) lines represent the results of the experiment (theoretical calculations). Horizontal arrows denote the magnetic field sweep direction. The insets show schematic magnetization configurations of the device obtained from micromagnetic modeling, given the field is swept from -1.5 to 1.5 T.

The second part of the experiment consisted of investigating the $I(V)$ characteristics of our double junction. The current was measured at $T = 1.8$ K for two values of the magnetic field: $B = 0$ (the black curve in Fig. 4.11(a)) and $B = -1.5$ T (the red curve). The absence of Coulomb staircase suggests that the two junctions have equal tunneling rates. From the $I(V_{\rm g})$ curve we deduce the value of the charging energy, $E_C \approx 1$ meV. The TMR, defined as

$$TMR = \frac{I_{-1.5\rm T} - I_{0\rm T}}{I_{0\rm T}}, \tag{4.13}$$

was plotted as a function of bias in Fig. 4.11(b). Interestingly, the TMR reaches its

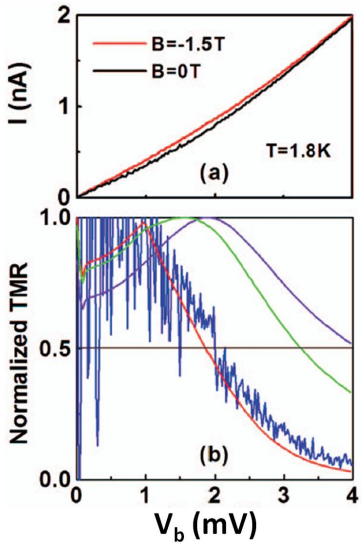

Figure 4.11: (a) Current-voltage characteristics measured at 1.8 K, with $B = 0$ (black curve) and -1.5 T (red curve), respectively. (b) TMR defined as $\mathrm{TMR} = (I_{-1.5\mathrm{T}} - I_{0\mathrm{T}})/I_{0\mathrm{T}}$, normalized by its maximum value, as a function of the bias voltage (black curve). The values for the current are taken from (a). The color lines represent numerical simulations done for different decay rates of the spin polarization of the island. The dimensionless decay time assumes values $\gamma = 1, 5, \infty$; the shorter the decay time, the steeper the TMR(V) function.

maximum value of 18% in the region of Coulomb blockade (i.e., for $eV_\mathrm{b} < E_C$) and falls rapidly when the drain-source voltage V_b exceeds E_C.

4.4.2 A noncollinear F-SET

The motivation of our work was to provide an explanation for the aforementioned experiments on F/I/F/I/F double junctions. Due to the geometry of the experimental set-up of Fig. 4.9, the orientation of the three electrodes (the cobalt source and drain, and the central island of nickel) is expected to be noncollinear for some

values of the external magnetic field. The magnetic field is applied in plane of our device and its value can be varied. We seek a simple theory that could support (some of) the experimental data and help us understand better the transport in F/I/F/I/F junctions with a noncollinear configuration of the magnetization vectors. Weak coupling between the central island and the external electrodes is assumed, therefore the calculations are performed in the regime of sequential tunneling of Chapter 2.

There has been a number of papers dealing with double ferromagnetic junctions of a noncollinear magnetization orientation, but the central electrode in those papers was always either a single-level quantum dot [81–83] or a normal metal [84–87]. More work, both theoretical and experimental, has been done on single F/I/F noncollinear junctions [88–92].

The relative configuration of the magnetization vectors of the junction is described uniquely by two angles: ϑ_{L} and ϑ_{R} between the magnetization of the central island and the magnetization of the left and right leads, respectively (Fig. 4.12). We assume fast energy relaxation on the island, i.e., after a tunneling of an electron onto or from the island, the electron distribution function on the island relaxes to the Fermi-Dirac distribution function in a time shorter than the time of a single tunneling event. The spin-relaxation time, τ_s, on the other hand, can be arbitrary and is a parameter in our simulations. The total Hamiltonian of the system is that of Eq. (2.1). The coupling between the leads and the central island is described by the tunneling part H_{T} of the Hamiltonian of our system, which is now somewhat more complicated than the Hamiltonian for the collinear system of Chapter 2; it reads

$$\begin{aligned} H_{\mathrm{T}}(\vartheta_{\mathrm{L}},\vartheta_{\mathrm{R}}) = \sum_{\alpha}\sum_{k,k'}\Big[&\left(T^{\alpha}_{k\uparrow,k'\uparrow} c^{\dagger}_{\alpha k\uparrow} \cos\frac{\vartheta_\alpha}{2} - T^{\alpha}_{k\downarrow,k'\uparrow} c^{\dagger}_{\alpha k\downarrow} \sin\frac{\vartheta_\alpha}{2} \right) c_{\alpha k'\uparrow} \\ &+ \left(T^{\alpha}_{k\downarrow,k'\downarrow} c^{\dagger}_{\alpha k\downarrow} \cos\frac{\vartheta_\alpha}{2} + T^{\alpha}_{k\uparrow,k'\downarrow} c^{\dagger}_{\alpha k\uparrow} \sin\frac{\vartheta_\alpha}{2} \right) c_{\alpha k'\downarrow} + \mathrm{H.c.} \Big] \end{aligned} \tag{4.14}$$

where the ‘up’ and ‘down’ direction of the electron spins is measured with respect

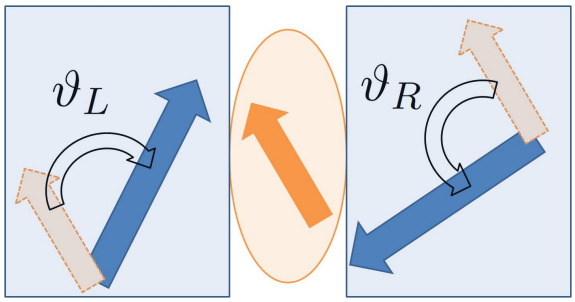

Figure 4.12: The three magnetization vectors of our noncollinear F-SET. The magnetization directions for the external electrodes are determined with respect to the direction of the island's magnetic moment by virtue of angles ϑ_{L} and ϑ_{R}.

to the local quantization axes. We follow the method of Chapter 2 and Ref. [93], except that now the magnetizations are noncollinear. This noncollinearity means that there are three different spin quantization axes here, and the tunneling rates will depend on the spin before and after the fact of tunneling. That is, the rate of tunneling for an electron with, say, spin 'up' from a lead to the island will now be more complicated than in Ref. [93], and depend on the angle between the magnetizations of that lead and the island. We apply Fermi's golden rule to calculate the tunneling rates, just as we did in the collinear case of the previous section (the F/I/N/I/F double junction), which ultimately lead to the spin currents (see Eq. (2.14)). These spin-polarized currents are calculated in the presence of spin accumulation in the island, so we must impose a self-consistent condition on them:

$$I_{\sigma}^{\mathrm{R}} - I_{\sigma}^{\mathrm{L}} = \left(\rho_{\sigma}\mathcal{V}e\Delta E_{\mathrm{F}}^{\sigma}\right)/\tau_{s}. \tag{4.15}$$

Note how this condition is different from the case of the normal-metal island of Eq. (2.28). The difference stems from the fact that the Fermi-energy spin splitting is symmetric in a normal metal, according to $\Delta E_{\mathrm{F}}^{\uparrow} = -\Delta E_{\mathrm{F}}^{\downarrow}$, while this is not generally true in a ferromagnet. In a ferromagnet, we have an asymmetry between the DOS for the two spin species, and a condition for the Fermi-energy

spin splitting becomes

$$\rho_{\uparrow}\Delta E_{\mathrm{F}}^{\uparrow} = \rho_{\downarrow}\Delta E_{\mathrm{F}}^{\downarrow}. \tag{4.16}$$

The directions of spins in the notation for the currents and Fermi-energy spin splittings are taken with respect to the quantization axis in the island.

The formulae for the rates from Section 2.4 still hold, only now the effective resistances in Eqs. (2.26) and (2.27) for the α-th junction become spin-dependent and can be written as

$$R_{\alpha}^{\uparrow(\downarrow)} = \frac{2R_{\alpha}^{\mathrm{p}}\left(1+\mathcal{P}_i\mathcal{P}_{\alpha}\right)}{\left(1\pm\mathcal{P}_i\right)\left(1\pm\mathcal{P}_{\alpha}\cos\vartheta_{\alpha}\right)} \tag{4.17}$$

and, naturally, the Fermi-energy splitting due to spin accumulation will no longer be symmetric, as we just mentioned. R_{α}^{p} denotes the resistance of the α-th junction when the magnetizations of the three electrodes are parallel to each other; the value of this parameter is taken from the experiment. $\mathcal{P}_{\alpha}$ and $\mathcal{P}_i$ are the spin polarizations of the α-th electrode (left or right) and of the island, respectively. We need resistances (or tunneling rates) that depend on the spin explicitly, at least if we want to take the spin relaxation into account (Eq. (4.15)).

It is worth commenting briefly on the values of the spin density of states (or spin polarization of the electrodes) that one should use for the simulations. It has been pointed out that there is a difference between these quantities yielded in band calculations and their values measured in tunneling transport [94]. For transition-metal ferromagnets not only the value, but also the sign of the spin polarization differs depending on whether we use the results of band calculations or tunneling measurments. In all the formulae above for transition rates and resistances, the spin polarization should be understood as the tunneling spin polarization, since it is transport we are looking at. However, the self-consistency condition (Eq. (4.15)) for the current contains the band-structure-calculation value of the spin density of states. As this condition describes the spin-splitting of the Fermi level in the island, all the electrons at the Fermi level, not only the ones that participate in transport, should be involved.

4.4.3 Numerical simulations

In practice, as the insets of Fig. 4.9 – a result of micromagnetic simulations – showed, the only three configurations of the magnetization vectors necessary for understanding the behavior of the double-junction resistance as a function of the magnetic field are those where $\vartheta_{\mathrm{L(R)}}$ is either $0°$, $90°$ or $180°$. We use these angles to calculate the corresponding effective resistances (Eq. (4.17)), which then are incorporated into the matrix-equation calculation akin to that of the previous section (and of Section 2.4).

First, we calculate the current and the total resistance of the F-SET at $V_{\mathrm{b}} = 1.5$ V and for the relevant magnetic-moment configurations. Then we plot the resistance as a function of the magnetic field (see the dashed curves in Fig. 4.10), by interpreting the system's magnetic configuration in accord with the insets of Fig. 4.10. We observe that the theoretical TMR is of the order of 8%, about two times smaller than the experimental one. This discrepancy, although large, is understandable considering the simplicity of our theoretical model. Besides, the order of magnitude has been reproduced.

Second, we compute the $I(V)$-characteristics of our double junction for two magnetic fields that correspond to the $\uparrow\uparrow\uparrow$ and $\uparrow\rightarrow\uparrow$ magnetization orientations, respectively. Later, the TMR is calculated, defined as in Eq. (4.13); the theoretical results are plotted in color in the lower panel of Fig. 4.11. The three color curves correspond to different decay rates $1/\gamma$ in the modified expression for the spin polarization of the central island as a function of bias voltage

$$\mathcal{P}(V) = \mathcal{P}_i e^{[(E_C - eV)/(\gamma E_C)]}, \tag{4.18}$$

where E_C is the charging energy for the island ($E_C/e \approx 1$ mV). The larger the decay rate, the steeper the V-dependence of the TMR. This phenomonological exponential decay of the spin polarization is an attempt of taking into account creation of magnons at the F/I interface, which is quite likely the phenomenon behind the drastic drop in TMR [95]. Energetically, the creation of magnons is not impossible at the range of small voltages of Fig. 4.10, as we explain in Paper

V. In the same paper we mention even other, less significant, mechanisms that may lead to a decay of spin polarization of the island.

Outlook

In Papers I-III we studied transport properties of small magnetic nanoparticles and the Mn_{12}-ac molecule. In practice, small magnetic nanoparticles are difficult to control, and the Mn_{12} molecule, though in many respects outstanding as an SMM, reacts strongly with the environment (e.g., when attached to a metallic electrode), which makes transport measurements very difficult and hard to reproduce [38, 39]. However, there exist more robust SMMs that do not loose their magnetic properties when attached to surfaces. Transport experiments on these SMMs [96, 97] are more easily reproducible. Thus, one possible extension of our work would be to do an SDFT calculation for these smaller molecular magnets and then compare it to the appropriate spin models. The coupling of the SMM to the external leads can be modeled more realistically by including explicitly the magnetic and electric fields in the SDFT approach. Another possibility for future research stems from the fact that higher-order tunneling processes contribute to the transport in some of these smaller and robust SMMs [97]. Consequently, extending the master-equation technique beyond the sequential-tunneling limit, in particular by taking into account cotunneling processes, seems to be a natural road to follow.

As for the theoretical part of Papers IV-V, in which we studied transport in large, metallic (ferromagnetic and normal-metal) nanoparticles, at least two issues require further investigation. The first one is the phenomenon of spin relaxation and how it originates from the strong spin-orbit interaction in metallic grains. A more detailed and realistic theory would enable us to estimate the spin accumu-

lation in such grains more accurately. Next, we have the very interesting issue of the F/I/F(N) interfaces that need to be accounted for more explicitly than what the single-electron-tunneling theory applied here does. Then, of course, it would be worthwhile to investigate at what point higher-order tunneling processes start playing a significant role in transport through our F-SETs. All those additional details, challenging theoretically, as they are, are of vital importance for better control and future applications of the studied systems.

Bibliography

[1] R. M. White, *Quantum Theory of Magnetism. Magnetic Properties of Materials*, Springer, Berlin, 3rd edition, 2007.

[2] R. Skomski, *Simple Models of Magnetism*, Oxford University Press, Oxford, New York, 2008.

[3] R. Skomski and J. M. D. Coey, *Permanent Magnetism*, Institute of Physics Publishing, Bristol, Philadelphia, 1999.

[4] G. A. Gehring, "An introduction to the theory of normal and ferromagnetic metals," in *Spin Electronics*, M. Ziese and M. J. Thornton, Eds. Springer, Berlin, Heidelberg, New York, 2001.

[5] C. Kittel, *Introduction to Solid State Physics*, Wiley, 8th edition, 2005.

[6] J. Stöhr and H. C. Siegmann, *Magnetism. From Fundamentals to Nanoscale Dynamics*, Springer, Berlin, 2006.

[7] J. Martinek and J. Barnaś, "Spin-dependent transport in single-electron devices," in *Concepts in Spin Electronics*, S. Maekawa, Ed. Oxford University Press, Oxford, New York, 2006.

[8] J. Barnaś and A. Fert, "Effects of spin accumulation on single-electron tunneling in a double ferromagnetic microjunction," *Europhys. Lett.*, vol. 44, p. 85, 1998.

[9] Yu. V. Nazarov and Ya. M. Blanter, *Quantum Transport: Introduction to Nanoscience*, Cambridge University Press, Cambridge, 2009.

[10] H. Grabert and M. H. Devoret (Eds.), *Single Charge Tunneling: Coulomb Blockade Phenomena in Nanostructures (NATO Science Series B: Physics)*, Springer, 1992.

[11] K. Yosida, *Theory of Magnetism*, Springer, 1996.

[12] C. Timm, "Tunneling through molecules and quantum dots: Master-equation approaches," *Phys. Rev. B*, vol. 77, p. 195416, 2008.

[13] K. Huang, *Statistical Mechanics*, Wiley, 2nd edition, 1987.

[14] I. O. Kulik and R. I. Shekhter, "Kinetic phenomena and charge discreteness effects in granulated media," *Zh. Eksp. Teor. Fiz.*, vol. 68, p. 623, 1975 [*Sov. Phys. JETP*, vol. 41, p. 308, 1975].

[15] D. V. Averin and K. K. Likharev, "Coulomb blockade of single-electron tunneling, and coherent oscillations in small tunnel junctions," *J. Low Temp. Phys.*, vol. 62, p. 345, 1986.

[16] B. L. Altshuler, P. A. Lee, and R. A. Webb (Eds.), *Mesoscopic Phenomena in Solids*, Elsevier, 1991.

[17] D. V. Averin and A. N. Korotkov, "Influence of discrete energy spectrum on correlated single-electron tunneling via a mesoscopically small metal granule," *Zh. Eksp. Teor. Fiz.*, vol. 97, p. 1661, 1990 [*Sov. Phys. JETP*, vol. 70, p. 937, 1990].

[18] D. V. Averin, A. N. Korotkov, and K. K. Likharev, "Theory of single-electron charging of quantum wells and dots," *Phys. Rev. B*, vol. 44, p. 6199, 1991.

[19] C. W. J. Beenakker, "Theory of Coulomb-blockade oscillations in the conductance of a quantum dot," *Phys. Rev. B*, vol. 44, p. 1646, 1991.

[20] Y. Meir, N. S. Wingreen, and P. A. Lee, "Transport through a strongly interacting electron system: Theory of periodic conductance oscillations," *Phys. Rev. Lett.*, vol. 66, p. 3048, 1991.

[21] L. I. Glazman and K. A. Matweev, "Coulomb correlations in the tunneling through resonance centers," *Pis'ma Zh. Eksp. Teor. Fiz.*, vol. 48, p. 403, 1988 [*JETP Lett.*, vol. 48, p. 445, 1988].

[22] M. Amman, R. Wilkins, E. Ben-Jacob, P. D. Maker, and R. C. Jaklevic, "Analytic solution for the current-voltage characteristic of two mesoscopic tunnel junctions coupled in series," *Phys. Rev. B*, vol. 43, p. 1146, 1991.

[23] J. Lambe and R. C. Jaklevic, "Molecular vibration spectra by inelastic electron tunneling," *Phys. Rev.*, vol. 165, p. 821, 1968.

[24] A. N. Korotkov and V. I. Safarov, "Nonequilibrium spin distribution in a single-electron transistor," *Phys. Rev. B*, vol. 59, p. 89, 1999.

[25] S. Guéron, M. M. Deshmukh, E. B. Meyers, and D. C. Ralph, "Tunneling via individual electronic states in ferromagnetic nanoparticles," *Phys. Rev. Lett.*, vol. 83, p. 4148, 1999.

[26] M. M. Deshmukh, S. Kleff, S. Guéron, E. Bonet, A. N. Pasupathy, J. von Delft, and D. C. Ralph, "Magnetic anisotropy variations and nonequilibrium tunneling in a cobalt nanoparticle," *Phys. Rev. Lett.*, vol. 87, p. 226801, 2001.

[27] C. M. Canali and A. H. MacDonald, "Theory of tunneling spectroscopy in ferromagnetic nanoparticles," *Phys. Rev. Lett.*, vol. 85, p. 5623, 2000.

[28] S. Kleff, J. von Delft, M. M. Deshmukh, and D. C. Ralph, "Model for ferromagnetic nanograins with discrete electronic states," *Phys. Rev. B*, vol. 64, p. 220401, 2001.

[29] A. Cehovin, C. M. Canali, and A. H. MacDonald, "Elementary excitations of ferromagnetic metal nanoparticles," *Phys. Rev. B*, vol. 68, p. 014423, 2003.

[30] E. McCann and V. I. Fal'ko, "Magnon-assisted transport and thermopower in ferromagnet-normal-metal tunnel junctions," *Phys. Rev. B*, vol. 68, p. 172404, 2003.

[31] A. Cehovin, C. M. Canali, and A. H. MacDonald, "Magnetization orientation dependence of the quasiparticle spectrum and hysteresis in ferromagnetic metal nanoparticles," *Phys. Rev. B*, vol. 66, p. 094430, 2002.

[32] P. W. Brouwer and D. A. Gorokhov, "Bound on anisotropy in itinerant ferromagnets from random impurities," *Phys. Rev. Lett.*, vol. 95, p. 017202, 2005.

[33] D. Gatteschi, R. Sessoli, and J. Villain, *Molecular Nanomagnets*, Oxford University Press, Oxford, New York, 2006.

[34] R. Sessoli, D. Gatteschi, A. Caneschi, and M. A. Novak, "Magnetic bistability in a metal-ion cluster," *Nature*, vol. 365, p. 141, 1993.

[35] L. Thomas, F. Lionti, R. Ballou, D. Gatteschi, R. Sessoli, and B. Barbara, "Macroscopic quantum tunnelling of magnetization in a single crystal of nanomagnets," *Nature*, vol. 383, p. 145, 1996.

[36] J. R. Friedman, M. P. Sarachik, J. Tejada, and R. Ziolo, "Macroscopic measurement of resonant magnetization tunneling in high-spin molecules," *Phys. Rev. Lett.*, vol. 76, p. 3830, 1996.

[37] W. Wernsdorfer and R. Sessoli, "Quantum phase interference and parity effects in magnetic molecular clusters," *Science*, vol. 284, p. 133, 1999.

[38] M.-H. Jo, J. E. Grose, K. Baheti, M. M. Deshmukh, J. J. Sokol, E. M. Rumberger, D. N. Hendrickson, J. R. Long, H. Park, and D. C. Ralph, "Signatures

of molecular magnetism in single-molecule transport spectroscopy," *Nano Lett.*, vol. 6, p. 2014, 2006.

[39] H. B. Heersche, Z. de Groot, J. A. Folk, , H. S. J. van der Zant, C. Romeike, M. R. Wegewijs, L. Zobbi, D. Barreca, E. Tondello, and A. Cornia, "Electron transport through single $\mathrm{Mn_{12}}$ molecular magnets," *Phys. Rev. Lett.*, vol. 96, p. 206801, 2006.

[40] L. Thomas, A. Caneschi, and B. Barbara, "Nonexponential dynamic scaling of the magnetization relaxation in $\mathrm{Mn_{12}}$ acetate," *Phys. Rev. Lett.*, vol. 83, p. 2398, 1999.

[41] F. Lionti, L. Thomas, R. Ballou, B. Barbara, A. Sulpice, R. Sessoli, and D. Gatteschi, "Thermally assisted macroscopic quantum resonance on a single-crystal of $\mathrm{Mn_{12}}$-acetate," *J. Appl. Phys.*, vol. 81, p. 4608, 1997.

[42] A. Caneschi, D. Gatteschi, R. Sessoli, A. L. Barra, L. C. Brunel, and M. Guillot, "Alternating current susceptibility, high field magnetization, and millimeter band EPR evidence for a ground $\mathrm{S = 10}$ state in $\mathrm{[Mn_{12}O_{12}(CH_3COO)_{16}(H_2O)_4] \cdot 2CH_3COOH \cdot 4H_2O}$," *J. Am. Chem. Soc.*, vol. 113, p. 5873, 1991.

[43] R. Sessoli, H.-L. Tsai, A. R. Schake, S. Wang, J. B. Vincent, K. Folting, D. Gatteschi, G. Christou, and D. N. Hendrickson, "High-spin molecules: $\mathrm{[Mn_{12}O_{12}(O_2CR)_{16}(H_2O)_4]}$," *J. Am. Chem. Soc.*, vol. 115, p. 1804, 1993.

[44] J. R. Friedman and M. P. Sarachik, "Single-molecule nanomagnets," *Annu. Rev. Condens. Matter Phys.*, vol. 1, p. 109, 2010.

[45] C. Romeike, M. R. Wegewijs, and H. Schoeller, "Spin quantum tunneling in single molecular magnets: Fingerprints in transport spectroscopy of current and noise," *Phys. Rev. Lett.*, vol. 96, p. 196805, 2006.

[46] C. Timm and F. Elste, "Spin amplification, reading, and writing in transport through anisotropic magnetic molecules," *Phys. Rev. B*, vol. 73, p. 235304, 2006.

[47] M. N. Leuenberger and E. R. Mucciolo, "Berry-phase oscillations of the Kondo effect in single-molecule magnets," *Phys. Rev. Lett.*, vol. 97, p. 126601, 2006.

[48] C. Timm, "Tunneling through magnetic molecules with arbitrary angle between easy axis and magnetic field," *Phys. Rev. B*, vol. 76, p. 014421, 2007.

[49] F. Elste and C. Timm, "Cotunneling and nonequilibrium magnetization in magnetic molecular monolayers," *Phys. Rev. B*, vol. 75, p. 195341, 2007.

[50] C. Romeike, M. R. Wegewijs, M. Ruben, W. Wenzel, and H. Schoeller, "Charge-switchable molecular magnet and spin blockade of tunneling," *Phys. Rev. B*, vol. 75, p. 064404, 2007.

[51] G. Gonzalez, M. N. Leuenberger, and E. R. Mucciolo, "Kondo effect in single-molecule magnet transistors," *Phys. Rev. B*, vol. 78, p. 054445, 2008.

[52] P. Hohenberg and W. Kohn, "Inhomogeneous electron gas," *Phys. Rev.*, vol. 136, p. B864, 1964.

[53] W. Kohn and L. J. Sham, "Self-consistent equations including exchange and correlation effects," *Phys. Rev.*, vol. 140, p. A1133, 1965.

[54] R. O. Jones and O. Gunnarsson, "The density functional formalism, its applications and prospects," *Rev. Mod. Phys.*, vol. 61, p. 689, 1989.

[55] Ed. D. Joubert, *Lecture Notes in Physics. Density functionals*, Springer, Heidelberg, 1998.

[56] R. M. Dreizler and E. K. U. Gross, *Density Functional Theory*, Springer, Berlin, 1990.

[57] H. Eschrig, *The Fundamentals of Density Functional Theory*, Teubner, Stuttgart, Leipzig, 1996.

[58] J. Kortus, *Electronic structure, magnetic ordering and phonons in molecules and solids* (Habilitationsschrift), Dresden, 2003.

[59] M. R. Pederson and C. C. Lin, "All-electron self-consistent variational method for Wannier-type functions: Applications to the silicon crystal," *Phys. Rev. B*, vol. 35, p. 2273, 1987.

[60] M. R. Pederson and K. A. Jackson, "Variational mesh for quantum-mechanical simulations," *Phys. Rev. B*, vol. 41, p. 7453, 1990.

[61] K. A. Jackson and M. R. Pederson, "Accurate forces in a local-orbital approach to the local-density approximation," *Phys. Rev. B*, vol. 42, p. 3276, 1990.

[62] M. R. Pederson and K. A. Jackson, "Pseudoenergies for simulations on metallic systems," *Phys. Rev. B*, vol. 43, p. 7312, 1991.

[63] A. A. Quong, M. R. Pederson, and J. L. Feldman, ," *Sol. Stat. Comm.*, vol. 87, p. 535, 1993.

[64] M. R. Pederson, J. Q. Broughton, and B. M. Klein, "Simulated annealing with floating Gaussians: Hellmann-Feynman forces without corrections," *Phys. Rev. B*, vol. 38, p. 3825, 1988.

[65] D. V. Porezag and M. R. Pederson, "Infrared intensities and Raman-scattering activities within density-functional theory," *Phys. Rev. B*, vol. 54, p. 7830, 1996.

[66] A. Briley, M. R. Pederson, K. A. Jackson, D. C. Patton, and D. V. Porezag, "Vibrational frequencies and intensities of small molecules: All-electron, pseudopotential, and mixed-potential methodologies," *Phys. Rev. B*, vol. 58, p. 1786, 1998.

[67] D. V. Porezag and M. R. Pederson, "Optimization of Gaussian basis sets for density-functional calculations," *Phys. Rev. A*, vol. 60, p. 2840, 1999.

[68] M. R. Pederson, D. V. Porezag, J. Kortus, and D. C. Patton, "Strategies for massively parallel local-orbital-based electronic structure methods," *Phys. Stat. Sol. (B)*, vol. 217, p. 197, 2000.

[69] M. R. Pederson and S. N. Khanna, "Electronic structure and magnetism of $Mn_{12}O_{12}$ clusters," *Phys. Rev. B*, vol. 59, p. 693(R), 1999.

[70] M. R. Pederson and S. N. Khanna, "Magnetic anisotropy barrier for spin tunneling in mn12o12 molecules," *Phys. Rev. B*, vol. 60, p. 9566, 1999.

[71] M. Getzlaff, *Fundamentals of Magnetism*, Springer, Berlin and Heidelberg, 2008.

[72] M. Jullière, "Tunneling between ferromagnetic films," *Phys. Lett. A*, vol. 54, p. 225, 1975.

[73] C. Heiliger, P. Zahn, and I. Mertig, "Microscopic origin of magnetoresistance," *Materials Today*, vol. 9, p. 46, 2006.

[74] I. Weymann and J. Barnaś, "Negative differential conductance and magnetoresistance oscillations due to spin accumulation in ferromagnetic double-island devices," *Phys. Rev. B*, vol. 73, p. 033409, 2006.

[75] K. Ono, H. Shimada, and Y. Ootuka, "Spin polarization and magneto-Coulomb oscillations in ferromagnetic single electron devices," *J. Phys. Soc. Jpn.*, vol. 67, p. 2852, 1998.

[76] K. Yakushiji, S. Mitani, K. Takanashi, and H. Fujimori, "Tunnel magnetoresistance oscillations in current perpendicular to plane geometry of $CoAlO$ granular thin films," *J. Appl. Phys.*, vol. 91, p. 7038, 2002.

[77] W. Wetzels, G. E. W. Bauer, and M. Grifoni, "Noncollinear single-electron spin-valve transistors," *Phys. Rev. B*, vol. 72, p. 020407, 2005.

[78] M. I. Dyakonov, "Spintronics?," in *Future Trends in Microelectronics: The Nano, the Giga, and the Ultra*, S. Luryi, J. Xu, and A. Zaslavsky, Eds., p. 424. Wiley-IEEE Press, New York, 2004.

[79] V. A. Ivanov, T. G. Aminov, V. M. Novotortsev, and V. T. Kalinnikov, "Spintronics and spintronics materials," *Russ. Chem. Bull. Intern. Ed.*, vol. 53, p. 2357, 2004.

[80] I. Zutic, J. Fabian, and S. Das Sarma, "Spintronics: Fundamentals and applications," *Rev. Mod. Phys.*, vol. 76, p. 323, 2004.

[81] J. König and J. Martinek, "Interaction-driven spin precession in quantum-dot spin valves," *Phys. Rev. Lett.*, vol. 90, p. 166602, 2003.

[82] J. König and J. Martinek, "Theory of transport through quantum-dot spin valves in the weak-coupling regime," *Phys. Rev. B*, vol. 70, p. 195345, 2004.

[83] W. Rudziński, J. Barnaś, R. Świrkowicz, and M. Wilczyński, "Spin effects in electron tunneling through a quantum dot coupled to noncollinearly polarized ferromagnetic leads," *Phys. Rev. B*, vol. 71, p. 205307, 2005.

[84] J. Barnaś and A. Fert, "Magnetoresistance oscillations due to charging effects in double ferromagnetic tunnel junctions," *Phys. Rev. Lett.*, vol. 80, p. 1058, 1998.

[85] J. Barnaś and A. Fert, "Effects of spin accumulation on single-electron tunneling in a double ferromagnetic microjunction," *Europhys. Lett.*, vol. 44, p. 85, 1998.

[86] A. Brataas, Yu. V. Nazarov, and G. W. Bauer, "Finite-element theory of transport in ferromagnet-normal metal systems," *Phys. Rev. Lett.*, vol. 84, p. 2481, 2000.

[87] D. H. Hernando, Yu. V. Nazarov, A. Brataas, and G. E. W. Bauer, "Conductance modulation by spin precession in noncollinear ferromagnet normal-metal ferromagnet systems," *Phys. Rev. B*, vol. 62, p. 5700, 2000.

[88] J. C. Slonczewski, "Conductance and exchange coupling of two ferromagnets separated by a tunneling barrier," *Phys. Rev. B*, vol. 39, p. 6995, 1989.

[89] J. S. Moodera, L. R. Kinder, T. M. Wong, and R. Meservey, "Large magnetoresistance at room temperature in ferromagnetic thin film tunnel junctions," *Phys. Rev. Lett.*, vol. 74, p. 3273, 1995.

[90] T. Miyazaki and N. Tezuka, "Giant magnetic tunneling effect in $\mathrm{Fe}/\mathrm{Al_2O_3}/\mathrm{Fe}$ junction," *J. Magn. Magn. Mater.*, vol. 139, p. L231, 1995.

[91] J. S. Moodera and L. Kinder, "Large magnetoresistance at room temperature in ferromagnetic thin film tunnel junctions," *J. Appl. Phys.*, vol. 79, p. 4724, 1996.

[92] H. Jaffres, D. Lacour, F. Nguyen Van Dau, J. Briatico, F. Petroff, and A. Vaures, "Angular dependence of the tunnel magnetoresistance in transition-metal-based junctions," *Phys. Rev. B*, vol. 64, p. 064427, 2001.

[93] I. Weymann and J. Barnaś, "Transport characteristics of ferromagnetic single-electron transistors," *Phys. Stat. Sol. (B)*, vol. 236, p. 651, 2003.

[94] R. Meservey and P. M. Tedrow, "Spin-polarized electron tunneling," *Phys. Rep.*, vol. 238, p. 173, 1994.

[95] S. Zhang, P. M. Levy, A. C. Marley, and S. S. P. Parkin, "Quenching of magnetoresistance by hot electrons in magnetic tunnel junctions," *Phys. Rev. Lett.*, vol. 79, p. 3744, 1997.

[96] J. E. Grose, E. S. Tam, C. Timm, M. Scheloske, B. Ulgut, J. J. Parks, H. D. Abru na, W. Harneit, and D. C. Ralph, "Tunneling spectra of indi-

vidual magnetic endofullerene molecules," *Nature Mater.*, vol. 7, p. 884, 2008.

[97] E. A. Osorio, K. Moth-Poulsen, H. S. J. van der Zant, J. Paaske, P. Hedegård, K. Flensberg, J. Bendix, and T. Bjørnholm, "Electrical manipulation of spin states in a single electrostatically gated transition-metal complex," *Nano Lett.*, vol. 10, p. 105, 2010.

Acknowledgements

First of all I would like to express my gratitude toward my supervisor Prof. Carlo M. Canali. His diligence, self-discipline, honesty and deep physical intuition, raised on a solid foundation of knowledge, as well as readiness to talk physics day and night make him an excellent scientist and a perfect guide in the fascinating, and sometimes treacherous, realms of solid-state physics. Thank you for all your support, Carlo.

I am very indebted to Prof. Håkan Pettersson, my co-supervisor, and Dr Ruisheng Liu for many fruitful discussions on the experimental physics of ferromagnetic single-electron transistors. I have learned a lot thanks to our collaboration. Prof. Vincenzo G. Benza and Dr Mark R. Pederson deserve special thanks for sharing with me of their rich expertise on the theory of nanomagnets. I would also like to thank Dr Magnus Paulsson for his help with some of the numerical calculations.

Special thanks go to Dr Susan R. Canali for her help with the English of this dissertation, and to Peter Liljenberg for his critical reading of the Swedish summary.

During the final period of my studies I have received a lot of support and positive reinforcement at my new workplace, Korrespondensgymnasiet. I would therefore like to thank my principal Bertil Tjerneld and all of my new Colleagues at Korr. Tack! It is great to teach, but it is even greater to teach among you.

Beata and Per Ekström deserve my deepest gratitude and friendship, as they were the first ones to make me feel more at home on this side of the Baltic Sea.

I would also like to thank Fr Paul Kozhippat for all his time and encouragement. Many thanks for numerous conversations and all the good time we shared go to all my friends in Kalmar, especially to Stefan Jönsson and Mirka Michalak. Among my friends back in Poland I wish to extend particular gratitude to Przemek Staroń for his supportive presence.

Finally, I would like to thank my Parents for accepting my own choices and letting me make them, and Miss Alicja Ziętal, my former geography teacher in grades 4–8, for igniting my interest in Nature.

S-J, you've been a source of inspiration over the last couple of months.

Paper I

Electron-Magnon Coupling and Nonlinear Tunneling Transport in Magnetic Nanoparticles

Ł. Michalak and C. M. Canali
Department of Chemistry and Biomedical Sciences, Kalmar University, 31912 Kalmar, Sweden

V. G. Benza
Dipartimento di Fisica e Matematica, Universita' dell'Insubria, Como, Italy
(Received 22 December 2005; published 1 September 2006)

We present a theory of single-electron tunneling transport through a ferromagnetic nanoparticle in which particle-hole excitations are coupled to spin collective modes. The model employed to describe the interaction between quasiparticles and collective excitations captures the salient features of a recent microscopic study. Our analysis of nonlinear quantum transport in the regime of weak coupling to the external electrodes is based on a rate-equation formalism for the nonequilibrium occupation probability of the nanoparticle many-body states. For strong electron-boson coupling, we find that the tunneling conductance as a function of bias voltage is characterized by a large and dense set of resonances. Their magnetic field dependence in the large-field regime is linear, with slopes of the same sign. Both features are in agreement with recent tunneling experiments.

DOI: 10.1103/PhysRevLett.97.096804 PACS numbers: 73.23.Hk, 72.10.Di, 72.25.Ba, 75.30.Ds

Metallic nanoparticles are among the best physical realizations of the concept of Fermi liquid introduced by Landau more than 50 years ago. Their discrete low-energy spectra can be put in a one-to-one correspondence with those of corresponding noninteracting electron systems. Single-electron tunneling spectroscopy [1] in normal-metal nanograins provides a vivid example of Landau's enormous simplification of interacting Fermi systems. Most of the interesting phenomena studied in these experiments can indeed be understood in terms of the quantum mechanics of confined noninteracting quasiparticles. If the grain is made of a ferromagnetic transition-metal material, however, the discrete resonant spectrum seen in tunneling experiments [2,3] is far more complex than the one predicted in an independent particle picture, and indicates that the quasiparticle states are coupled to the collective magnetic moment of the grain. Since ferromagnetic transition metals, in addition to Landau's particle-hole (p-h) excitations, support low-energy collective spin excitations, it is reasonable to assume that tunneling transport through ferromagnetic nanoparticles involves some kind of spin excitations that are the finite-system analogue of the familiar spin-waves or magnons of bulk ferromagnets. So far attempts of including spin collective modes in tunneling transport based on a simple toy model [4–6] have explained only in part the rich phenomena seen in experiment.

In this Letter we present a theoretical study of single-electron tunneling transport through a ferromagnetic metal nanoparticle based on a model that captures the salient features of its elementary excitations—p-h and spin collective—as derived from a recent *microscopic* study [7]. A few remarkable features seen in experiment emerge in a very transparent and direct way from our treatment of the electron-magnon coupling. We find that when a low-energy p-h excitation is strongly coupled to one of the spin collective modes, the tunneling differential conductance versus bias voltage displays an enhanced density of resonances with spacings smaller than the independent-electron energy mean-level spacing δ. The dependence of the tunneling resonances on external magnetic field is regulated by the behavior of the underlying quasiparticle states; it is characterized by mesoscopic fluctuations at small fields and a monotonic dependence at fields larger than the switching field. The model further predicts that in the limit of ultrasmall nanoparticles, where δ is much larger than the typical magnon energy, the conductance should display clusters of resonances separated by an energy of order δ.

The choice of our model is motivated by the microscopic analysis of Ref. [7], where the explicit derivation of the exchange-field-fluctuation propagator allows one to determine the elementary spin excitations (Stoner p-h and collective) of a magnetic grain. One finds that for a small nanoparticle there is one isolated spin collective mode below the lowest p-h excitation energy, which corresponds to the ferromagnetic resonance excitation (spatially uniform $q = 0$ spin wave), of energy $E_{\mathrm{res}} \sim$ magnetic anisotropy energy/atom ≈ 0.1 meV in cobalt. For large nanoparticles, the ferromagnetic resonance lies in a region of p-h quasicontinuum and acquires a linewidth αE_{res}, where $\alpha < 1$ is the Gilbert damping parameter. The crossover between these two regimes occurs when one p-h excitation contributes to the resonance, namely, when $\delta = \sqrt{\alpha} E_{\mathrm{res}}$. Although the nanoparticles investigated in Ref. [2,3] are too small to strictly satisfy this condition, interactions between p-h excitations and spin-wave modes, including the *nonuniform* ones ($q \neq 0$), will frequently occur. As long as the mechanism of the interaction of one p-h excitation with one spin-wave mode is independent on the latter being uniform or nonuniform, we can illustrate it by following Ref. [7], where the uniform case was consid-

ered. It was shown that when only one p-h excitation of energy $\epsilon_{ab} = \xi_b - \xi_a$ is close to $E_{\rm res}$, the exchange-field propagator has two poles at energies

$$\omega_{\pm} = \frac{E_{\rm res} + \epsilon_{ab}}{2} \pm \{[(E_{\rm res} - \epsilon_{ab})/2]^2 + \gamma^2\}^{1/2}. \quad (1)$$

The avoided crossing gap γ resulting from the collective mode p-h coupling is found to be $\gamma \sim \alpha E_{\rm res} = \frac{\Delta_{\rm MF}}{\sqrt{2S}}|\langle b|S_x|a\rangle|$, where $2S = N_\uparrow - N_\downarrow$ is the total spin of the nanoparticle, and $\Delta_{\rm MF}$ is the amplitude of the spin-splitting field. The presence of the matrix element $|\langle b|S_x|a\rangle|$ in the expression for γ emphasizes the fact that the coupling between spin waves or magnon and electrons is ultimately due to the exchange interaction, which conserves spin. Thus the quasiparticle states a and b should have opposite spins. In spite of the fact that most of the states lying close to the Fermi level have minority-spin character, because of spin-orbit coupling, the quasiparticle states $|I\rangle$ are in fact linear combinations of spin-up and spin-down components $|I\rangle = \alpha_I|\uparrow\rangle + \beta_I|\downarrow\rangle$, and the matrix element $|\langle b|S_x|a\rangle|$ will not vanish. Notice, however, that since spin-orbit interaction is relatively weak in transition-metal ferromagnets, the quasiparticle states can still be assumed to have in general one predominant spin character with just a small admixture of the other.

The Hamiltonian describing the isolated nanoparticle in which a magnon is coupled to one p-h excitation is

$$H_d = \sum_{i=a,b} \epsilon_i c_i^\dagger c_i + \omega\beta^\dagger\beta + \gamma(c_a^\dagger c_b\beta^\dagger + c_b^\dagger c_a\beta) + U\hat{n}(\hat{n} - 1), \quad (2)$$

where $c_i^\dagger$ and c_i with $i = a, b$ are Fermi operators creating and annihilating two electronic levels of energy ϵ_a and ϵ_b, respectively, with $\epsilon_a < \epsilon_b$. The Bose operators $\beta^\dagger$ and β describe a magnon of energy ω. Below we measure all energies in units of the mean-level spacing $\delta \equiv \epsilon_b - \epsilon_a$. The term $\gamma(c_a^\dagger c_b\beta^\dagger + c_b^\dagger c_a\beta)$ represents the electron-magnon coupling. It can be interpreted as a vertex describing an electron scattering from the electronic state a (respectively, b) to the state b (a), while absorbing (emitting) a magnon. We will view the coupling strength γ as a phenomenological parameter; $\gamma \sim \omega$ represents strong coupling. Recently, electron-boson interactions have been used extensively to model electron-phonon coupling in molecular single-electron transistors [8]. An interaction term more similar to ours has been used in studying magnon-assisted transport in ferromagnetic tunneling junctions [9]. The last term in Eq. (2) represents a Coulomb repulsion energy, which is nonzero when both electronic levels are occupied, $\langle\hat{n}\rangle = 2$. The model in Eq. (2), representing a double-level system coupled to one boson mode, is well known in quantum optics and cavity quantum electrodynamics under the name of the Jaynes-Cummings model [10]. The model can be solved exactly, since it conserves both the number of electrons $n = n_a + n_b$ and the quantity $(n_b - n_a)/2 + m$, where m is the number of bosons. In the trivial cases $n = 0$ and $n = 2$ the energy spectrum is $\epsilon_m^n = \omega m + n/2(\epsilon_a + \epsilon_b + 2U)$; the corresponding eigenstates are $|0, m\rangle = (\beta^\dagger)^m|0\rangle$ and $|2, m\rangle = c_a^\dagger c_b^\dagger(\beta^\dagger)^m|0\rangle$, where $|0\rangle$ is the vacuum. The $n = 1$, $(n_b - n_a)/2 + m + 1/2 = k + 1$ eigenspace is spanned by the states

$$|1_a, k+1\rangle \equiv c_a^\dagger(\beta^\dagger)^{k+1}|0\rangle, \quad |1_b, k\rangle \equiv c_b^\dagger(\beta^\dagger)^k|0\rangle. \quad (3)$$

The Hamiltonian is now diagonalized within each k subspace, yielding the eigenvalues ϵ_k^+ and ϵ_k^-,

$$\epsilon_k^\pm = \epsilon_k^0 + \epsilon_{\rm av} \pm \frac{1}{2}\sqrt{\epsilon_{\rm res}^2 + 4\gamma^2(k+1)}, \quad (4)$$

where $\epsilon_{\rm res} \equiv (\epsilon_b - \epsilon_a) - \omega$ and $\epsilon_{\rm av} \equiv \frac{1}{2}(\epsilon_a + \epsilon_b + \omega)$. The corresponding eigenvectors are

$$|\pm, k\rangle = \delta_1^\pm(k)|1_a, k+1\rangle + \delta_2^\pm(k)|1_b, k\rangle, \quad (5)$$

where

$$\delta_1^\pm(k) = \frac{\gamma\sqrt{k+1}}{\sqrt{[\epsilon_k^\pm - \epsilon_a - \omega(k+1)]^2 + \gamma^2(k+1)}}, \quad (6)$$

$$\delta_2^\pm(k) = \frac{[\epsilon_k^\pm - \epsilon_a - \omega(k+1)]}{\sqrt{[\epsilon_k^\pm - \epsilon_a - \omega(k+1)]^2 + \gamma^2(k+1)}}. \quad (7)$$

On top of these states $|\pm, k\rangle$ there is also the state $|1_a, 0\rangle$ with energy ϵ_a, which forms a decoupled one-dimensional subspace in the $n = 1$ sector. We now assume that the magnetic grain is weakly coupled to metallic external electrodes and investigate single-electron tunneling transport through the grain [1]. The total Hamiltonian describing the system is $H = H_d + H_l + H_r + H_t$, where H_d is given in Eq. (2); H_l and H_r describe the left and right electrodes, assumed to be normal Fermi liquids $H_\alpha = \sum_p \xi_{p\alpha} c_{p\alpha}^\dagger c_{p\alpha}$, $\alpha = l, r$, where p is the quantum number specifying a quasiparticle of energy $\xi_{p\alpha}$ measured with respect to the chemical potential of lead α; H_t is the tunneling Hamiltonian coupling the grain to the electrodes $H_t = \sum_{p,\alpha=r,l}[t_{p\alpha}c_{p\alpha}^\dagger(c_a + c_b) + \text{H.c.}]$. In the limit of weak coupling, transport takes place via sequential tunneling, which can be described by means of a standard rate-equation formalism for the occupation probabilities of the grain many-body states [11]. We are interested in the regime where Coulomb blockade is first lifted by applying an external bias voltage, and only the two charge states $n = 0, 1$ are involved. The master equations describing the kinetics of the *nonequilibrium* occupation probabilities $P_k^n = \{P_k^0, P_0^a, P_k^-, P_k^+\}$ for the states $\{|0, k\rangle, |1_a, 0\rangle, |-, k\rangle, |+, k\rangle, k = 0, 1, \ldots\}$, are

$$\dot{P}_k^0 = -\sum_{k';\alpha}[2P_k^0(W_{0k;+k'}^\alpha + W_{0k;-k'}^\alpha + W_{0;a}^\alpha) - P_{k'}^+ W_{+k';0k}^\alpha - P_{k'}^- W_{-k';0k}^\alpha - P_0^a W_{a;0}^\alpha], \quad (8)$$

$$\dot{P}_0^a = 2P_0^0\sum_\alpha W_{0;a}^\alpha - P_0^a\sum_\alpha W_{a;0}^\alpha, \quad (9)$$

$$\dot{P}^{\pm}_{k} = -\sum_{k';\alpha}[P^{\pm}_{k} W^{\alpha}_{\pm k;0k'} - 2P^{0}_{k'} W^{\alpha}_{0k';\pm k}]. \quad (10)$$

The coefficients $W^{\alpha}_{\cdots}$ appearing in Eqs. (8)–(10) are transition rates between two many-body states of the grain caused by electron tunneling from and to the leads. For instance, $W^{\alpha}_{0k;+k'}$ is the transition rate from state $|0, k\rangle$ to $|+, k'\rangle$ due to an electron tunneling from the α electrode onto the grain. The $W^{\alpha}_{\cdots}$ are given by Fermi's golden rule

$$W^{\alpha}_{0k;\pm k'} = \Gamma^{\alpha}_{0k;\pm k'} n_F(\epsilon^{\pm}_{k'} - \epsilon^{0}_{k} - \mu_\alpha)[\delta^{\pm}_{1}(k')^2 \delta_{k',k-1} + \delta^{\pm}_{2}(k')^2 \delta_{k',k}], \quad (11)$$

$$W^{\alpha}_{0;a} = \Gamma^{\alpha}_{0;a} n_F(\epsilon_a - \mu_\alpha), \quad (12)$$

where μ_α is the electrochemical potential of lead α, which we assume to be shifted symmetrically around zero by the applied bias voltage V: $\mu_l = -\mu_r = V/2$. The transition rates $W^{\alpha}_{\pm k';0k}$ and $W^{\alpha}_{a;0}$ are obtained from $W^{\alpha}_{0k;\pm k'}$ and $W^{\alpha}_{0;a}$, respectively, by replacing the Fermi function with $[1 - n_F]$ evaluated at the same energy. The tunneling rates $\Gamma^{\alpha}_{0k;\pm k'} = \frac{2\pi}{\hbar}\sum_p |t_{p\alpha}|^2 \delta[\epsilon_{p\alpha} - (\epsilon^{\pm}_{k'} - \epsilon_k)]$ will be taken for simplicity to be independent of energy and lead index, $\Gamma^{\alpha}_{0k;\pm k'} = \Gamma$. The nonequilibrium steady-state probability P^{n}_{k} is the solution of the matrix equation $\check{M}\check{P} = 0$, where the matrix $\check{M}$ includes all the transition rates, and $\check{P}$ is a vector of all the P^{n}_{k}'s. The dc current through the left or right junction is then written as

$$I = (+/-)e\Big\{\sum_k \Big[2P^{0}_{k}\sum_{k'}(W^{l/r}_{0k;-k'} + W^{l/r}_{0k;+k'}) - P^{-}_{k}\sum_{k'} W^{l/r}_{-k;0k'} - P^{+}_{k}\sum_{k'} W^{l/r}_{+k;0k'}\Big] + 2P^{0}_{0} W^{l/r}_{0;a} - P^{a}_{0} W^{l/r}_{a;0}\Big\}. \quad (13)$$

The transition sequence $|n = 0\rangle \rightarrow |n = 1\rangle \rightarrow |n = 0\rangle$ allows the tunneling electron to probe the coupled p-h spin-wave excitations of the grain, which appear as resonances in the differential conductance dI/dV as a function of the bias voltage V. We discuss first the case where the p-h excitation is coupled with the uniform ($q = 0$) spin-wave mode. For the nanoparticles considered in Refs. [2,3], $\delta \sim 1$ meV, while the energy of the uniform spin wave is approximately equal to the anisotropy energy/atom ~ 0.1 meV. In Fig. 1 we plot I and dI/dV vs V for the case $\omega = 0.1\delta$, which pertains to this situation. The calculations are done at temperature $T = 0.005\delta$, corresponding to the experimental $T \approx 50$ mK. When $\gamma = \omega$ [Fig. 1(a)], three sets of peaks in the conductance are visible. The first isolated peak occurs when the current starts to flow, and corresponds to the successive transitions $|0\rangle \rightarrow |1_a, 0\rangle \rightarrow |0\rangle$ which are possible when $\mu_l = V/2 = \epsilon_a$ [12]. On further increasing V, the current remains constant until the next lowest charging state ϵ^{-}_{0} becomes available (at eV $= 6.8\delta$ for this case). For yet larger V higher states $|0, k\rangle$ and $|-, k\rangle$ acquire a finite nonequilibrium occupation probability, and new transport channels open up. In principle, each allowed transition $|0, k\rangle \rightarrow |-, k\rangle$ gives a resonance at $\epsilon^{-}_{k} - \epsilon^{0}_{k}$, as shown in the inset of Fig. 1(a), calculated at very low temperature, $T = 0.001\delta$. But at $T = 0.005\delta$ only their envelope is visible in the form of a small bump in the conductance centered at eV $= 6.9\delta$. The third large peak, appearing at $eV = 7.0\delta$ is also the envelope of many closely spaced resonances, caused primarily by the transitions through the second group of charged states, $|+, k\rangle$, which become available at that energy. Although values of $\gamma > \omega$ are not very realistic, it is instructive to study the limit behavior of the tunneling conductance for large values of the magnon-electron coupling. In Fig. 1(b) we plot I and dI/dV vs V for $\gamma = 2\omega$. We can see that a large γ causes the sets of resonances of Fig. 1(a) to merge into one cluster, whose individual peaks now start to become visible also at $T = 0.005\delta$. Notice however, that the mean-level spacing between the peaks is $\approx 0.05\delta$, in fact much smaller than the experimentally observed resonance spacing, 0.2δ. This leads us to conclude that such a large density of resonances, caused by an unrealistically strong coupling to the uniform spin-wave mode, is *not* the one observed experimentally.

We now turn to the case where the p-h excitation is coupled to a nonuniform spin-wave mode. The exchange energy of the first nonuniform mode is $\omega \sim \Delta(a/R)^2$, where Δ is proportional to the exchange constant, a is the lattice constant, and R is the nanoparticle diameter. For a 4-nm Co nanoparticle we find $\omega \approx 1$ meV, which is approximately equal to δ [2]. In Fig. 2(a) we plot the IV characteristics for the resonant case, $\omega = \delta$, and two different values of γ. At small γ we have again two separate sets of resonances, which are now perfectly resolvable even at the experimental temperature. When γ is increased up to 0.8, the two sets of resonances merge into one cluster, as shown in Fig. 2(b). The number of resonances in the cluster is of the order of 15, with level spacing $\approx 0.3\delta = 0.3(\epsilon_b - \epsilon_a) = 0.3\omega$. Such a dense set of resonances with

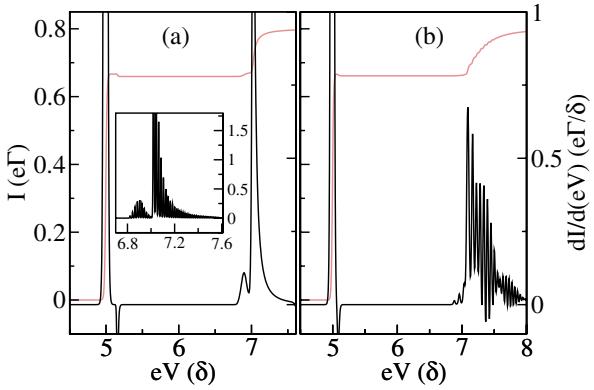

FIG. 1 (color online). Current and differential conductance versus bias voltage V for $\omega = 0.1\delta$. (a) The electron-magnon coupling strength is $\gamma = 0.1\delta$; (b) $\gamma = 0.2\delta$. The temperature T is set equal to 0.005δ, except in the inset, where it is equal to 0.001δ.

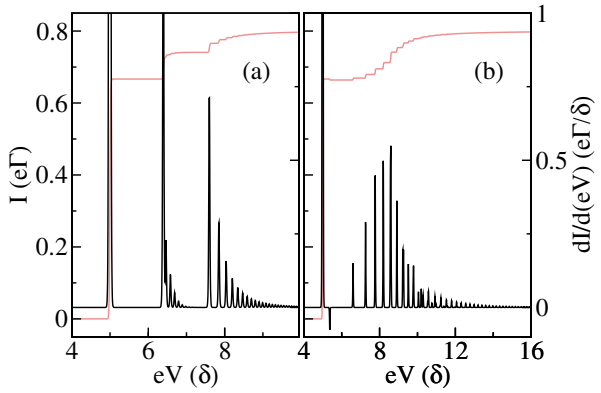

FIG. 2 (color online). Current and differential conductance versus bias voltage V, for $\omega = \delta$. (a) $\gamma = 0.3\delta$; (b) $\gamma = 0.8\delta$ The temperature T in both cases is set equal to 0.005δ.

spacing ≈ 0.2–0.5δ is one of the characteristic features observed experimentally in tunneling spectroscopy of magnetic nanograins. The results of Fig. 2 do not depend on ω being exactly equal to δ, but remain valid for $\delta \geq \omega$, although the larger ω the larger is γ that takes to go from Fig. 2(a) and 2(b). For nanoparticles much smaller than the ones considered in Refs. [2,3], when $\delta \gg \omega$, our model predicts that the conductance spectrum should eventually exhibit sets of resonances separated by an energy $\approx \delta \propto 1/R^3$.

We finally discuss the magnetic field dependence of the resonance spectrum. A crucial feature of our analysis is based on the assumption that the two bare electronic states $|1_a, 0\rangle$ and $|1_b, 0\rangle$ have predominantly minority-spin character. The fact that minority electrons dominate the tunneling transitions had been originally predicted in Refs. [4,5] and was later confirmed by experiments in gated devices [3]. We consider first the regime of small external fields, where the magnetic grain is close to a reversal of the magnetic moment. The electronic states are coupled to the moment itself, and as this moves under the effect of the field, the energies of the states will be subject to random fluctuations [13–15]. Also the frequency of the ferromagnetic mode can fluctuate strongly [7]. Within our model these fluctuations will result in a quasirandom dependence of conductance resonances as a function of the field. At larger fields, after the reversal has taken place, the situation is different. The grain magnetic moment will point along the field and the energies of the minority states $|1_a, 0\rangle$ and $|1_b, 0\rangle$ will increase linearly with the field strength B, with a slope given by their effective $g_{a/b}$ factors, which are ≈ 2 since spin-orbit coupling is weak. Similarly the spin-wave energy dependence can be parameterized by $\omega(B) = \omega(0) + g_\beta \mu_B B$ [7]. We obtain $\epsilon_k^{\pm} - \epsilon_k^0 = \text{const} + \frac{1}{2}[g_a + g_b + g_\beta \pm \Gamma(B)]\mu_B B$ and $\epsilon_k^{\pm} - \epsilon_{k+1}^0 = \text{const} + \frac{1}{2}[g_a + g_b - g_\beta \pm \Gamma(B)]\mu_B B$ for the resonance excitation energies, where $\Gamma = \sqrt{(g_a - g_b - g_\beta)^2 + \text{const}/B^2}$. If we take $g_{a/b} \approx 2$ and $g_\beta \leq 2$ [7], we find that the excitation energies are increasing functions of B. Thus we conclude that the conductance spectrum exhibits essentially a monotonic linear dependence on the field, and the slopes of the resonance energies have the same sign.

In conclusion, we have proposed a model that describes coupled electron-magnon excitations in a ferromagnetic metal nanoparticle. The conductance spectrum of single-electron tunneling exhibits a broad and dense set of resonances when the coupling is of the order of the magnon energy. The resonant peaks show Zeeman shifts of the same sign as a function of the external field. Both features of the model are in agreement with experiment. We expect that the resonances originate from the coupling to nonuniform spin waves; furthermore, the tunneling spectrum should break into individual clusters for ultrasmall particles.

We would like to thank A. H. MacDonald, D. Ralph, K. Flensberg, V. Fal'ko, and G. Usaj for useful discussions. This work was supported in part by the Swedish Research Council under Grant No: 621-2004-4339, the Faculty of Natural Science of Kalmar University and by ONR under Grant No. N00014-02-1-0813.

[1] For reviews, see G.-L. Ingold and Yu. V. Nazarov, in *Single Charge Tunneling*, edited by H. Grabert and M. H. Devoret, NATO Advanced Study Institute, Ser. B Vol. 294 (Plenum, New York, 1992); Jan von Delft and D. C. Ralph, Phys. Rep. **345**, 61 (2001).
[2] S. Guéron *et al.*, Phys. Rev. Lett. **83**, 4148 (1999).
[3] M. M. Deshmukh *et al.*, Phys. Rev. Lett. **87**, 226801 (2001).
[4] C. M. Canali and A. H. MacDonald, Phys. Rev. Lett. **85**, 5623 (2000).
[5] S. Kleff *et al.*, Phys. Rev. B **64**, 220401 (2001).
[6] S. Kleff and J. von Delft, Phys. Rev. B **65**, 214421 (2002).
[7] A. Cehovin, C. M. Canali, and A. H. MacDonald, Phys. Rev. B **68**, 014423 (2003).
[8] D. Boese and H. Schoeller, Europhys. Lett. **54**, 668 (2001); K. D. McCarthy, N. Prokofev, and M. T. Tuominen, Phys. Rev. B **67**, 245415 (2003); S. Braig and K. Flensberg, *ibid.* **68**, 205324 (2003); A. Mitra, I. Aleiner, and A. J. Millis, *ibid.* **69**, 245302 (2004).
[9] E. McCann and V. I. Fal'ko, Phys. Rev. B **68**, 172404 (2003).
[10] E. T. Jaynes and F. W. Cummings, Proc. IEEE **51**, 89 (1963).
[11] C. W. J. Beenakker, Phys. Rev. B **44**, 1646 (1991); D. Weinmann, W. Hausler, and B. Kramer, Phys. Rev. Lett. **74**, 984 (1995).
[12] This peak in Figs. 1 and 2, is an artifact of the model, where the state $|1_a, 0\rangle$ is decoupled within the $n = 1$ sector.
[13] A. Cehovin, C. M. Canali, and A. H. MacDonald, Phys. Rev. B **66**, 094430 (2002).
[14] P. W. Brouwer and D. A. Gorokhov, Phys. Rev. Lett. **95**, 017202 (2005).
[15] G. Usaj and H. U. Baranger, Europhys. Lett. **72**, 110 (2005).

Paper II

Theory of Tunneling Spectroscopy in a Mn_{12} Single-Electron Transistor by Density-Functional Theory Methods

Ł. Michalak,[1] C. M. Canali,[1] M. R. Pederson,[2] M. Paulsson,[1] and V. G. Benza[3]

[1]*Division of Physics, Department of Natural Sciences, Kalmar University, 391 82 Kalmar, Sweden*

[2]*Center for Computational Materials Science, Naval Research Lab, Code 6390, Washington, DC 20375, USA*

[3]*Dipartimento di Fisica e Matematica, Universita dell' Insubria, 20064 Como, Italy*

(Received 10 November 2008; revised manuscript received 2 November 2009; published 5 January 2010)

We consider tunneling transport through a Mn_{12} molecular magnet using spin density functional theory. A tractable methodology for constructing many-body wave functions from Kohn-Sham orbitals allows for the determination of spin-dependent matrix elements for use in transport calculations. The tunneling conductance at finite bias is characterized by peaks representing transitions between spin multiplets, separated by an energy on the order of the magnetic anisotropy. The energy splitting of the spin multiplets and the spatial part of their many-body wave functions, describing the orbital degrees of freedom of the excess charge, strongly affect the electronic transport, and can lead to negative differential conductance.

DOI: 10.1103/PhysRevLett.104.017202 PACS numbers: 75.50.Xx, 31.15.ej, 73.23.Hk, 85.65.+h

There is a growing interest in exploring the rich physics and spintronics functionality of molecular single-electron transistors (SETs) consisting of a few *magnetic* molecules weakly coupled to nanogapped electrodes [1]. Recently two groups [2,3] have carried out single-electron tunneling experiments on individual magnetic molecules based on $Mn_{12}O_{12}$ (henceforth Mn_{12}) with organic ligands. Mn_{12} is the most studied and perhaps the most remarkable molecular magnet [4]. In its crystal phase, Mn_{12} is characterized by a long spin relaxation time due to its large uniaxial magnetic-anisotropy energy. Furthermore, at low temperatures, quantum effects in the relaxation properties are clearly discernible [5–8] and have been attributed to quantum tunneling of the molecule collective magnetization [4]. How these properties are revealed in electronic quantum transport is a question of great significance for the field of molecular spintronics [1]. Indeed, the SET experiments [2,3] show signatures of the molecule magnetic state and its low-energy collective spin excitations. The theoretical models proposed so far [2,3,9–15] are typically based on effective giant-spin Hamiltonians with large uniaxial anisotropy barriers. This approach has two drawbacks [16]. First, the effective spin Hamiltonian for the charged states (anion and cation) of Mn_{12} needed to describe sequential tunneling transport, is not known. Scaling of the global anisotropy parameter to account empirically for changes in the number of electrons forming a macro-spin is fraught with uncertainty [17]. Second, the orbital degrees of freedom are not included in the giant-spin Hamiltonian formalism. The orbital effects due to changes in electron population on the Mn_{12} molecule modify the symmetry and magnitude of the magnetic-anisotropy Hamiltonian and can even change the spin ordering [18].

In this Letter we provide a microscopic many-body description of the ground state (GS) and low-lying spin excitations of both neutral and *charged* states of a Mn_{12} molecular magnet. Our approach is based on spin density functional theory (SDFT), which has been very successful in describing the spin-orbit-induced magnetic-anisotropy barrier in Mn_{12} and other molecular magnets [19–21]. We find that when a *delocalized* electron is added to (subtracted from) the molecule, the GS spin of the molecule increases (decreases) by $1/2$. For both charged states, the GS magnetic-anisotropy energy is larger than for the neutral Mn_{12}. We then incorporate this information into a quantum master equation for electronic transport in the sequential tunneling approximation, which is appropriate for the experimental Coulomb blockade (CB) regime. The approximate many-particle eigenstates lead to a tunneling conductance that exhibits fine structure on the order of the anisotropy energy and, under certain circumstances, to strong negative differential conductance (NDC). Comparison with the giant-spin model shows that spatial selection rules play a crucial role in determining which spin excitations contribute the most to the tunneling conductance.

We need to know the many-electron wave functions, representing low-energy spin excitations, as a function of the excess charge (Q), spin ordering ($\mathbf{M} \equiv \{\mu_\nu\}_{\nu=1,12}$), applied electric $\mathbf{E}$ and magnetic $\mathbf{B}$ fields, and the parameters θ, ϕ describing the quantization axes. We refer to the collection of all possible variables as the ''order-parameter vector'' (OPV), $\mathbf{p} \equiv (Q, \mathbf{M}, \mathbf{E}, \mathbf{B}, \theta, \phi)$ to label the states. Given a specific OPV, we first construct a set of Kohn-Sham (KS) single-particle states $\Phi_k(\mathbf{p})$, by diagonalizing a KS single-particle Hamiltonian $H(\mathbf{p})$ that depends upon this OPV. Since some of these effects (Q, $\mathbf{M}$) are clearly large and some (θ, ϕ) are generally small, there is flexibility as to which of these terms must be accounted for self-consistently. Specifically,

$$H(\mathbf{p}) = H(Q, \mathbf{M}, \mathbf{E}, \mathbf{B}, \theta, \phi) = H_0(\mathrm{DFT}, Q, \mathbf{M}) + V_{\mathbf{L}\cdot\mathbf{S}}(\theta, \phi) + \mathbf{E}\cdot\mathbf{r} + \mathbf{B}\cdot(\mathbf{L} + 2\mathbf{S}) \quad (1)$$

contains a spin-polarized term $H_0(\mathrm{DFT}, Q, \mathbf{M})$, which is treated self-consistently for the cation, neutral, and anionic states ($Q = +1, 0$ and -1); $V_{\mathbf{L}\cdot\mathbf{S}}(\theta, \phi)$ represents the spin-orbit interaction. We neglect the last two terms representing the coupling to external fields.

The spin-ordering $\mathbf{M}$ corresponds to that obtained from the local moments of the 12 Mn atoms (μ_ν) in the classical ferrimagnetic state of the neutral molecule [22]. The spin-orbit operator is treated exactly [19]—albeit non-self-consistently—in the basis of the eigenstates of $H_0(\mathrm{DFT}, Q, \mathbf{M})$. Diagonalizing the above Hamiltonian with the constraint that the expectation value of the total spin ($\langle\mathbf{S}\rangle$) is quantized along the axis determined by θ, ϕ results in a set of single-particle, *noncollinear* spin orbitals, $\phi_k(\mathbf{p})$, expressed as $\phi_k = \phi_k^+(r)\chi_+(\theta, \phi) + \phi_k^-(r)\chi_-(\theta, \phi)$. Here, the angle-dependent spinors $\chi_\pm(\theta, \phi)$ are spin-1/2 coherent states specified by the quantization axis, $\chi_\pm(\theta, \phi) = \cos(\theta/2)|\pm\rangle \pm \sin(\theta/2)e^{\pm i\phi}|\mp\rangle$.

We now construct approximate many-body functions for the ground and excited electronic states as single Slater determinants (SDs) of the spin orbitals $\phi_k(p)$:

$$|\mathbf{p}; k_1, k_2, \ldots, k_{N_Q}\rangle \equiv |\phi_{k_1}(\mathbf{p})\phi_{k_2}(\mathbf{p})\ldots\phi_{k_{N_Q}}(\mathbf{p})\rangle. \quad (2)$$

The above states are generally not eigenstates of either $\mathbf{S}^2$ or S_z. However, a state with $|\langle\mathbf{S}^2\rangle| = S_0(S_0 + 1)$, especially when constructed from a closed shell of spatial states, is expected to be the primary contributor to an $S = S_0$ eigenstate. While the variables (θ, ϕ) generate a continuous overdetermined set of SDs, a judicious choice of $2S_0 + 1$ values of θ and ϕ can lead to a nearly orthogonal set of normalized linearly independent many-particle SDs, with $\langle S_z\rangle$ taking on integer or half integer values akin to the standard $M = -S_0, -S_0 + 1, \ldots, S_0$ quantum numbers. Choosing $2S + 1$ values of θ given by $S\cos(\theta_M) = M$ leads to integer or half integer $\langle S_z\rangle$ regardless of the choice of ϕ; however, choosing $\phi_M = M\phi_0$ leads to destructive interference in the off-diagonal elements of these states and aids in producing approximate S_z eigenstates. For the case of $S = 10$, we find that choosing $\phi_0 = 34°$ leads to the smallest off-diagonal overlaps between approximate eigenstates. We call the $2S_0 + 1$ many-electron states constructed with this procedure a spin multiplet. Besides the GS spin multiplet, the anion and cation have a few low-lying excited spin multiplets. These come about because the HOMO level of the charged molecule is quasidegenerate with a many-fold of LUMO levels [18]. Using Eq. (2), we can construct several SD excited-states close in energy to the GS, all having the same spin, S_0. The relevant spin multiplets for the molecule are shown in Fig. 1(a). Typically, the level spacing within each spin multiplet is of the order of 0.1–1 meV, while different multiplets are separated by energies of the order of 10 meV. Note that the energies of a given spin multiplet are not exactly invariant under $M \to -M$, since the choice of the angle ϕ_M is incommensurate with the nonperfectly uniaxial symmetry of Mn_{12}. The breaking of the level degeneracy for the $(M, -M)$ pair is of the order of the transverse anisotropy terms coming from 4th order spin-orbit contributions, and therefore very small [23]. For a later comparison with the giant-spin approach, we disregard the small deviations from uniaxial symmetry and consider the spin Hamiltonian $H_{S_Q} = \sum_{i,n} D_{S_Q,i,n}[S_{Q,i}^z]^n$, given in terms of spin variables $\vec{S}_{Q,i}$ for each spin multiplet i of charge state Q; $D_{S_Q,i,n}$ are anisotropy constants which we extract by fitting the corresponding SDFT energy spectra. Table I shows the total spin, GS energy and magnetic-anisotropy energy of the lowest spin multiplet calculated for the different charge states of Mn_{12}. Adding an electron to the molecule increases the molecule spin and decreases the energy. Furthermore, the anisotropy increases significantly when a delocalized electron is added to the neutral molecule. This is due to the fact that there is a near degeneracy between unoccupied onefold and twofold states. The spin-orbit interaction leads to a strong mixing between these states which, because of the orbital components, enhances the anisotropy.

In the following we discuss quantum transport through a Mn_{12} molecule weakly coupled to metallic electrodes. Electron tunneling between leads and the molecule is described by the Hamiltonian $H_T = \sum_{\alpha,l}\sum_{k,\mathbf{p}} t_{\alpha l}a_{\alpha l}^\dagger c_k(\mathbf{p}) + \mathrm{H.c.}$, where $c_k^\dagger$ (c_k) creates (de-

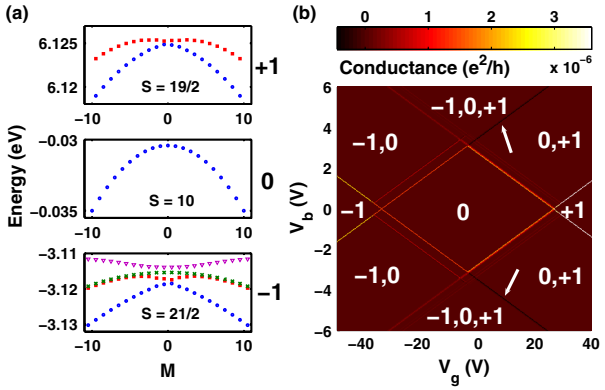

FIG. 1 (color online). (a) Lowest lying spin multiplets for the three charge states of the molecule; the small energy difference between states M and $-M$ is due to transverse anisotropy terms coming from 4th-order spin-orbit contributions and our choice of the $2S + 1$ values of (θ_M, ϕ_M). See text after Eq. (2). (b) Differential conductance of a Mn_{12} SET as a function of bias and gate voltage, for a symmetric double junction, with gate capacitance equal to 1/20 of the total capacitance, at zero temperature. Numbers -1, 0 and $+1$ denote the excess charge on the molecule and label regions of Coulomb blockade. In regions $(-1, 0)$, $(0, +1)$ and $(-1, 0, +1)$ transport is possible via transitions between different charge states.

TABLE I. The GS properties from DFT: spin, energy, and magnetic-anisotropy energy as a function of charge.

State	Q	Spin	Energy (eV)	MAE (K)	MAE (meV)
Anion	-1	21/2	-3.08	137	11.8
Neutral	0	20/2	0.00	55	4.7
Cation	1	19/2	6.16	69	5.9

stroys) an electron in orbital k in the molecule, and t_α depends on the tunneling barrier between lead $\alpha = L, R$ (left or right) and the molecule. The leads, at electrochemical potential μ_α, are described by the independent-electron Hamiltonian $H_\alpha = \sum_l \epsilon_{\alpha l} a^\dagger_{\alpha l} a_{\alpha l}$, where $a^\dagger_{\alpha l}$ ($a_{\alpha l}$) creates (destroys) a quasiparticle of quantum number l. We also take into account the work function for the external leads. As a result, the charge state populated at zero gate and bias voltages is the neutral one, and not the anion as it would seem from Table I. The sequential tunneling current is obtained from a master equation for the occupation probabilities of the molecule many-body states. The transition rate between two many-body states via tunneling of an electron from lead α into the molecule, is proportional to $f(E(\mathbf{p}', k_i', N_{Q'}) - E(\mathbf{p}, k_i, N_Q) - \mu_\alpha) \times |\langle \mathbf{p}'; k_1', k_2', \ldots, k_{N_{Q'}}' | c_k^\dagger(\mathbf{p}) | \mathbf{p}; k_1, k_2, \ldots, k_{N_Q} \rangle|^2$, where $f(E)$ is the Fermi distribution function and $E(\mathbf{p}, k_i, N_Q)$ is the energy of state $|\mathbf{p}; k_1, k_2, \ldots, k_{N_Q}\rangle$, modified by the bias $V_b = (\mu_L - \mu_R)/e$ and gate voltage V_g. We then solve numerically the master equation in steady-state and obtain the current as a function of V_b and V_g. Figure 1(b) shows the differential conductance $G = dI/dV_b$ as function of V_b and V_g. The calculations are done at zero temperature. We choose equal coupling of the molecule to the two leads; the gate capacitance is equal to $1/20$ of the total capacitance of the system. Three CB stability diamonds are visible, corresponding to the three different charge states $Q = -1$, 0, $+1$, where transport is blocked. In region indicated by $(-1, 0)$, [respectively $(0, +1)$], current flows through transitions between anionic (cationic) and neutral states. In region $(-1, 0, +1)$ all three charge states are present. The additional lines parallel to the GS-GS transitions are due to transitions between excited states. In Fig. 1(b) we can also see two lines, indicated by arrows, that correspond to a decrease in the current with increasing V_b (NDC). These lines give the bias at which, for a given V_g, anionic states become occupied in the $(0, +1)$ region. NDC in Mn_{12}-SET has been observed experimentally [2].

For a better understanding of transport just above the CB gap, in Fig. 2(a) we plot the differential conductance as a function of V_b, for $V_g = -20$ V. Transport in this region is due to transitions between the spin multiplets of the neutral and anionic molecule. The conductance peak spectrum displays a rich fine structure, with peak spacing on the order of 0.1–1 meV, which corresponds to that seen in experiment [2,3]. The first set of peaks at the very onset of transport is caused by transitions between the GS spin multiplets. Surprisingly, the conductance in this region is very small, $G \leq 10^{-8} e^2/h$, as shown in the inset; it is practically invisible for transitions between the low-lying states (large $|M|$ and $|M'|$) and slightly larger for transitions between higher-lying states (small $|M|$ and $|M'|$). As we argue below, this is caused by the very small overlap of the *orbital* parts of the many-body wave functions of the two GS spin multiplets. The second set of peaks in Fig. 2(a), $V_b \geq 1.485$ V, corresponds to transitions between the GS spin multiplet of the neutral molecule and the first three excited spin multiplets of the anion. This cluster of resonances is largely determined by the first excited spin multiplet of the anion, since reaching this multiplet opens up transport also via other multiplets. In particular, the dominant peak seen in the figure is due to transitions between the lowest-energy states of the GS spin multiplet of the neutral molecule and the first excited spin multiplet of the anion, as shown in Fig. 2(b).

In order to shed light on the interplay between orbital and spin-selection rules, we compare the SDFT-based calculation with the giant-spin model. Within this spin model, transitions are possible only between states whose spin differs by 1/2 (spin-selection rule), with transition rates given by Clebsch-Gordan (CG) coefficients [24]. In the computation of the conductance, we include the GS spin multiplet of the neutral molecule, and the GS and first three excited spin multiplets of the anion. The conductance for the giant-spin model is shown with the dotted line in Fig. 2(a). The first 11 peaks correspond to subsequent transitions between states $M = \pm S, \pm(S-1), \ldots, 0$ and $M' = \pm S', \pm(S'-1), \ldots, 1/2$, where $S' = S + 1/2$. The intensity of these peaks decreases monotonically with decreasing $|M|$, which is different from the SDFT-

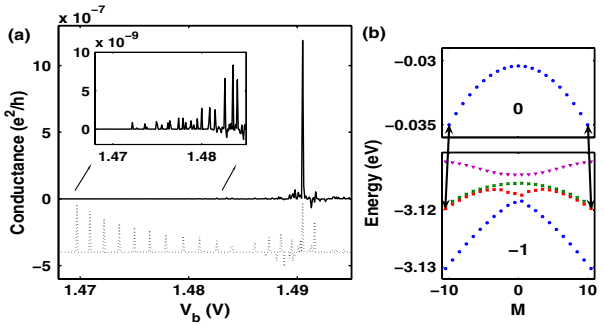

FIG. 2 (color online). (a) Differential conductance as a function of bias at $V_g = -20$ V. Parameters are as in Fig. 1. Solid (dotted, offset for clarity) lines: calculation based on SDFT (giant-spin model). Inset of (a) shows a zooming of the onset of SDFT transport due to transitions between the ground-state (GS) spin multiplets of the neutral and anionic molecule. Visible peaks in the main plot correspond to transitions between the GS spin multiplet of the neutral and the first three excited multiplets of the anion. (b) Spin multiplets involved in the transport. The transitions between the states generating the dominant peak in (a) are indicated by arrows joining the states.

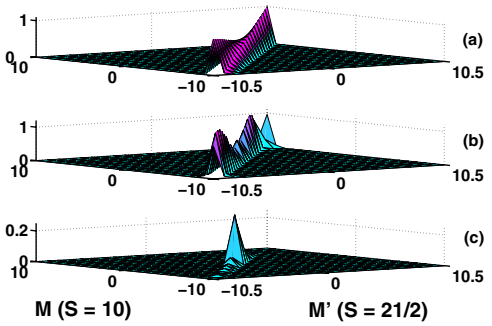

FIG. 3 (color online). Matrix elements for transitions between anionic and neutral charge states. (a) Giant-spin model; (b) SDFT results for transitions from neutral GS spin multiplet to anionic first excited multiplet; (c) SDFT results for transitions from neutral GS to anionic GS spin multiplets.

based conductance. The more complicated set of peaks at $V_b \geq 1.485$ V in Fig. 2(a) resembles the analogous cluster of peaks for SDFT and has the same interpretation. We examine the matrix elements giving the neutral-to-anion transition rates. Figure 3(a) shows the results for the giant-spin model, where the matrix elements are proportional to the CG coefficients and the spin-selection rule $|M - M'| = 1/2$ is strictly obeyed. Figure 3(b) shows that the same spin-selection rule is approximately satisfied by the SDFT matrix elements of the transitions between the GS spin multiplet of the neutral molecule and the first excited spin multiplet of the anion. In particular, the orbital part of the wave functions does not modify substantially this condition. In contrast, Fig. 3(c) shows that the SDFT matrix elements for the transition between the two GS spin multiplets are different: the effect of the spin-selection rules is now overridden by space selection rules, which suppress most of the transition rates near $|M| = S$ and lead to a vanishing conductance. Furthermore, the GS matrix elements close to the diagonal behave differently as a function of $|M|$ for the two models: they decrease with $|M|$ for SDFT and increase for the spin model, which is reflected in the conductance [Fig. 2(a)] for $V_b < 1.485$ V. Based on Figs. 3(a)–3(c), we expect the giant-spin model to agree better with the SDFT calculation for transitions involving the first excited-state spin multiplet of the anion. Indeed, Fig. 2(a) shows that for bias voltages $V_b \geq 1.485$ V the two models yield qualitatively the same conductance. The small matrix elements in Fig. 3(c) are also the cause of the NDC seen in Fig. 1(b) along the line separating the transport regions $(0, +1)$ and $(-1, 0, +1)$: when V_b becomes large enough to access the anion GS multiplet, the system remains trapped in these states due to their small connection to the neutral states. Thus, the current decreases.

In conclusion, we presented a microscopic study of the GS properties and low-energy spin excitations for the neutral and charged Mn_{12} molecular magnet, based on SDFT. Resonances in the tunneling conductance are governed both by spin and spatial selection rules. The latter ones play a key role in determining the relative contribution to transport of various spin multiplets, and can lead to NDC. The orbital properties of the spin states provided by SDFT are essential to build a correct effective spin model and interpret the transport experiments.

This work was supported by the Faculty of Natural Sciences at Kalmar University and the Swedish Research Council under Grant No. 621-2007-5019. M. R. P. thanks the DOD HPCMO for computational resources.

Note added.—After this manuscript was submitted, another Letter [25] related to our work appeared.

[1] L. Bogani and W. Wernsdorfer, Nature Mater. **7**, 179 (2008).
[2] H. B. Heersche *et al.*, Phys. Rev. Lett. **96**, 206801 (2006).
[3] M. H. Jo *et al.*, Nano Lett. **6**, 2014 (2006).
[4] D. Gatteschi, R. Sessoli, and J. Villain, *Molecular Nanomagnets* (Oxford, New York, 2006).
[5] R. Sessoli *et al.*, Nature (London) **365**, 141 (1993).
[6] L. Thomas *et al.*, Nature (London) **383**, 145 (1996).
[7] J. R. Friedman *et al.*, Phys. Rev. Lett. **76**, 3830 (1996).
[8] W. Wernsdorfer and R. Sessoli, Science **284**, 133 (1999).
[9] C. Romeike, M. R. Wegewijs, and H. Schoeller, Phys. Rev. Lett. **96**, 196805 (2006).
[10] C. Timm and F. Elste, Phys. Rev. B **73**, 235304 (2006).
[11] M. N. Leuenberger and E. R. Mucciolo, Phys. Rev. Lett. **97**, 126601 (2006).
[12] C. Timm, Phys. Rev. B **76**, 014421 (2007).
[13] F. Elste and C. Timm, Phys. Rev. B **75**, 195341 (2007).
[14] C. Romeike *et al.*, Phys. Rev. B **75**, 064404 (2007).
[15] G. Gonzalez, M. N. Leuenberger, and E. R. Mucciolo, Phys. Rev. B **78**, 054445 (2008).
[16] J. Lehmann and D. Loss, Phys. Rev. Lett. **98**, 117203 (2007).
[17] K. Park *et al.*, Phys. Rev. B **68**, 020405 (2003).
[18] K. Park and M. R. Pederson, Phys. Rev. B **70**, 054414 (2004).
[19] M. R. Pederson and S. N. Khanna, Phys. Rev. B **60**, 9566 (1999).
[20] M. Pederson *et al.*, Phys. Status Solidi B **217**, 197 (2000).
[21] J. Kortus *et al.*, Polyhedron **22**, 1871 (2003).
[22] J. Kortus, C. S. Hellberg, and M. R. Pederson, Phys. Rev. Lett. **86**, 3400 (2001).
[23] The breaking of the $M \rightarrow -M$ symmetry is the result of our approximation in constructing spin multiplets in terms of spin coherent states. Obviously *exact* eigenstates of a spin Hamiltonian would maintain the $M \rightarrow -M$ invariance, assured by time-reversal symmetry.
[24] C. M. Canali and A. H. MacDonald, Phys. Rev. Lett. **85**, 5623 (2000).
[25] S. Barraza-Lopez *et al.*, Phys. Rev. Lett. **102**, 246801 (2009).

Paper III

Giant-Spin Hamiltonian versus First-Principles Approach in the Theory of Tunneling Transport in Single-Molecule Magnets

Ł. Michalak[1,2], C. M. Canali[2] and M. R. Pederson[3]

[1]*Division of Solid State Physics, Department of Physics, Lund University, 221 00 Lund, Sweden*

[2]*Division of Physics, School of Computer Science, Physics and Mathematics, Linnaeus University, 391 82 Kalmar, Sweden and*

[3]*Center for Computational Materials Science, Naval Research Lab, Code 6390, Washington, DC 20375, USA*

(Dated: December 9, 2010)

Abstract

A detailed analysis of a recently proposed theoretical approach (*Phys. Rev. Lett.* **104**, 017202 (2010)) to quantum transport in a Mn_{12} single-electron transistor based on spin density-functional theory (SDFT) is presented. SDFT is used to construct low-energy many-body states describing collective spin excitations relevant to transport. We investigate, in particular, the HOMO and LUMO levels of all charge states of Mn_{12} and how their energy gap affects the magnetic anisotropy and the collective spin excitations of the system. We then discuss in detail how to construct all the transition rates between the spin many-body states used in the master-equation for quantum transport. The ab-initio approach that includes orbital degrees of freedom of the excess charge on the molecule is compared with a pure spin model in the transport calculations. We observe that the orbital degrees of freedom lead to a suppression of certain transition matrix elements, which results in a current suppression and negative differential conductance. We also propose an efficient way for circumventing the numerical difficulties that concern the singularity of the linear-equation system for transport calculations.

I. INTRODUCTION

Low-dimensional nanostructures that possess a net magnetic moment have been entertaining considerable attention over the last decades, mainly due to their possible applications in data storage, spintronics, and quantum computation. Magnetic nanoparticles are a typical example of such structures, but their importance for applications might be even surpassed by another class of systems - *single-molecule magnets* (SMMs) [1], that is, molecules that are characterized by a magnetic moment at least several times larger than that of a single electron [2]. Single-molecule magnets are typically characterized by large anisotropy barriers, responsible for very long spin relaxation times. Unlike nanoparticles, molecules can be easily synthesized chemically in multiple identical copies, which is clearly an advantage both for research and technology. Specifically, the net magnetic moment of a molecule will be the same in each molecule of the given compound and it will not depend on the environment (as long as the temperature is kept low and magnetic field is off). SMMs exhibit also, at the level of macroscopic experiment, a purely quantum phenomenon of magnetic-moment tunneling, which lies at the basis of the observed staircase-shaped hysteresis loop [3–6]. The magnetic moment of the molecule is thus controlled by an external magnetic field. A prototypical example of an SMM is the Mn_{12}-acetate, which is comprised of 12 manganese ions that are interconnected with organic ligands; the Mn ions are responsible for the molecule magnetic moment. Its high value of the magnetic moment ($S = 10$) and long relaxation time (of the order of months in crystal phase) make Mn_{12} a particularly promising candidate for future applications.

For designing data-storage or quantum-computation applications of SMMs, or magnetic nanostructures in general, transport studies are of considerable importance. An SMM, used as a central electrode together with metallic external leads, will form a single-molecule transistor in which transport occurs via sequential tunnelings of individual electrons, due to the charging effects that become manifested when the central island is small enough. Furthermore, the molecule magnetic moment can depend on the molecule charge. Hence adding (removing) one electron to (from) the molecule by means of transport could be yet another way of controlling the molecule magnetic moment.

As of now, two groups have performed single-electron tunneling measurements on an individual Mn_{12} SMM [7, 8]. These experiments were conducted in the Coulomb-blockade

regime, that is, the coupling to the leads was weak. Current suppression and negative differential conductance (NDC) [7], and a puzzling lack of hysteresis [8] have been observed. The theoretical models for single-electron transistors (SETs) with Mn_{12} as a central island developed so far [7–15] are based on giant-spin Hamiltonians. As such, they disregard the orbital degrees of freedom in the energy spectrum of the Mn_{12} molecule and how they affect the tunneling electron [16]. These models make also some arbitrary assumptions as to the magnitude of the magnetic moment of the charged molecule [16]. The theoretical models proposed by another two groups [17, 18] for transport in Mn_{12} combine nonequilibrium Green's functions technique with density-functional theory (DFT). However, this mean-field approach is not very well-suited for transport calculations with electrodes well separated from the central islands by potential barriers, that is, for the Coulomb-blockade regime. Besides, these two models do not include the effect of charging on the magnitude of the molecule magnetic moment or on the molecule energy spectrum. The additional electron spreads over the contact region and no direct hopping onto/off the molecule, reminiscent of the aforementioned experiments, is present.

From looking at these two groups of theoretical models of single-electron transistors (SETs) with Mn_{12} as the central island, we see that, in order to make some advancement, it is essential to provide an ab-initio microscopic model for both the charged and uncharged molecule that includes the orbital degrees of freedom (by means of spin-orbit coupling) on top of the spin ones. Later, the molecule has to be well separated from the external leads so that the weak-coupling regime of the experimental set-up is mimicked. This is done much better by a master-equation method, where tunneling between the ground and excited states of the charged and neutral molecule corresponds to adding an electron to or removing it from the molecule, than by approaching the subject with mean-field machinery.

In our paper we provide an ab-initio description (more detailed when compared to that of Ref. [19]) of the Mn_{12} molecule and apply the resultant knowledge of the molecule electronic structure to a SET set-up in such a way that these two demands are met. For modeling the molecule itself, we use spin density-functional theory (SDFT) which, by including spin-orbit coupling, allows us to compute the crystalline magnetic anisotropy of the molecule. We find that adding a *delocalized* electron causes the magnetic moment of the molecule to increase by 1/2. When the energy spectrum is at hand, the molecule is sandwiched between two external metallic electrodes and transport in the regime of weak coupling is allowed [19]. Spin-orbit

coupling modifies the rates of tunneling between the many-body states of different charge, which – in turn – leads to a modification of the conductance spectrum, when compared to a giant-spin model. Under certain circumstances, the inclusion of the orbital degrees of freedom leads to NDC. The conductance exhibits fine structure of the order of the anisotropy energy.

Compared with Ref. [19], the present paper provides a more detailed description of the SDFT method as applied to Mn_{12}, as well as of the transport-calculation approach. Also the results are presented and discussed in a more comprehensive manner. In particular, we present the full many-body energy spectrum of the Mn_{12} molecule and all the transition overlaps between the spin multiplets belonging to the three different charge states (anion, neutral, and cation). Furthermore, the enhancement of the magnetic anisotropy energy (MAE) due to charging and the origin of the existence of several spin multiplets for the charged states (anion and cation) are elaborated on in a larger extent. Next, the values for the charging energy are given (≈ 2.5 eV) and commented on. In the transport part, we compare the spin-model- and SDFT-based electric currents in a broader range of bias voltage that covers transitions to/from the neutral molecule from/to both charged states; the analysis of Ref. [19] was limited to the onset of transport (low bias voltage, and only anion-to/from-neutral transitions). In addition, we present here a numerical way of dealing with a sparse (and thus singular) system of rate equations that we encounter in the transport calculations.

This paper is organized as follows. Section II gives a detailed description of calculating the energies of the ground state (GS) and lowest excited states of a charged and neutral molecule (Part A). In Part B of Section II we provide and discuss the energy spectrum of the molecule and some GS properties for the three different charges (anion, neutral, cation). Section III covers the transport calculation by means of master equations; it also includes a discussion of some numerical difficulties encountered in this calculation. Results for conductance and their discussion are given towards the end of that section. Finally, Section IV contains a summary and a few words on the possible future extensions of our work.

II. SPIN DENSITY-FUNCTIONAL CALCULATION

A. Method

The goal of our calculation is to obtain low-energy properties of the Mn_{12} neutral, anionic and cationic molecule. We do that within the framework of the Kohn-Sham method of the spin density functional theory. A set of variables defines our system, such as: the excess charge Q ($Q = 0$ for the neutral molecule and $Q = \pm 1$ for the cation and the anion, respectively), the spin ordering $\mathbf{M}$ ($\mathbf{M} \equiv \{\mu_\nu\}_{\nu=1,12}$ where μ_ν is the magnetic moment of the ν-th Mn ion), the external electric $\mathbf{E}$ and magnetic $\mathbf{B}$ fields, and the parameter angles θ and ϕ that determine the quantization axes with respect to the easy axis of the molecule, which is given by the molecule symmetry. These variables put together constitute an order-parameter vector (OPV), $\mathbf{p} \equiv (Q, \mathbf{M}, \mathbf{E}, \mathbf{B}, \theta, \phi)$, which is used for labeling the states. Not all of the components of OPV have the same effect on the system, in particular the effect of Q and $\mathbf{M}$ is large when compared to the dependence on θ or ϕ. Thus, we are allowed to split the total Hamiltonian, which is a function of OPV, into the following terms:

$$H(\mathbf{p}) = H(Q, \mathbf{M}, \mathbf{E}, \mathbf{B}, \theta, \phi) = H_0(DFT, Q, \mathbf{M}) + V_{\mathrm{s-o}}(\theta, \phi) + \mathbf{E} \cdot \mathbf{r} + \mathbf{B} \cdot (\mathbf{L} + 2\mathbf{S}). \quad (1)$$

The self-consistent diagonalization of the first term, $H_0(DFT, Q, \mathbf{M})$, for a given OPV, provides us with a set of Kohn-Sham single-particle states $\Phi_k(\mathbf{p})$. When we have this set of wave functions at our disposal, we can now include the spin-orbit interaction, $V_{\mathrm{s-o}}$, by applying the usual time-independent perturbation theory to the obtained set of states (for d-orbitals, which are responsible for the main magnetic properties of the Mn_{12} molecule, the spin-orbit interaction is much weaker than the exchange or Coulomb interactions, so a perturbative treatment is well justified). The external fields $\mathbf{E}$ and $\mathbf{B}$, contained in the last two terms in the equation above, are set to zero throughout this paper.

The spin ordering $\mathbf{M}$ is obtained from the classical ferrimagnetic arrangement of the local magnetic moments of the 12 Mn ions (μ_ν) in the neutral molecule [20, 21]. This spin configuration is constructed from four $\mu = 3$ minority-spin Mn ions, $3d(t_{2g})^3$, on the inner cubane Mn_4O_4 unit of the molecule and eight $\mu = 4$ majority-spin Mn ions, $3d(t_{2g})^3 3d(e_g)$, on the outer crown of the molecule. Through exact diagonalization of Heisenberg Hamiltonians developed from DFT calculations [20], Park *et al.* [21] find that the classical ferrimagnetic

configuration has a weight of approximately 36 percent in the exact many-spin $S = 10$ state. Similarly, by determining exchange parameters from inelastic neutron scattering followed by exact diagonalization, Waldmann and Guedel [22] find that this configuration has a weight of approximately 64 percent.

The spin-orbit matrix elements are not calculated by assuming the usual $\mathbf{L}\cdot\mathbf{S}$ representation, which is suitable only for spherically symmetric systems. Instead, the more appropriate and exact Cartesian representation, as developed for non-symmetric and/or multi-centered systems [23], is used. The first-order corrections to the energy eigenstates vanish due to the quenching of the angular orbital momentum of the d-orbitals in the ligand field of the molecule, and the second-order ones are always negative [23] and sensitive to the angles θ and ϕ. The spin-orbit coupling accounts for the magnetic anisotropy in our system.

When diagonalizing the total Hamiltonian in Eq. (1), including the spin-orbit correction, we impose the constraint on the expectation value of the total spin ($\langle\mathbf{S}\rangle$) that it be quantized along the axis determined by θ and ϕ. As a result, we obtain a set of single-particle noncollinear spin orbitals $\phi_k(\mathbf{p})$

$$\phi_k(\mathbf{p}) = \phi_k^+(r)\chi_+(\theta,\phi) + \phi_k^-(r)\chi_-(\theta,\phi), \tag{2}$$

where $\chi_\pm(\theta,\phi) = \cos(\theta/2)|\pm\rangle \pm \sin(\theta/2)e^{\pm i\phi}|\mp\rangle$ are the spin-$\frac{1}{2}$ coherent states defined by the quantization axis.

We are now ready to construct approximate many-body wave functions for the ground and low-lying excited states as single Slater determinants (SDs) of the spin orbitals $\phi_k(p)$

$$|\mathbf{p}; k_1, k_2, \ldots k_{N_Q}\rangle \equiv |\phi_{k_1}(\mathbf{p})\phi_{k_2}(\mathbf{p})\ldots\phi_{k_{N_Q}}(\mathbf{p})\rangle, \tag{3}$$

where N_Q is the number of electrons for a given charge state Q. The excited states can be represented in terms of creation and destruction operators acting on the GS Slater determinants for a given OPV. Overlaps between many-body states corresponding to different charge states lead to transition rates that are used in the conductance calculation later on.

The variables θ and ϕ yield a continuous overdetermined set of SDs which are clearly not eigenstates of either S^2 or S_z. However, as can be deduced from Ref. [21], a state with $|\langle S\rangle| = S_0$, especially when constructed from a closed shell of spatial states, is expected to be the primary contributor to an $S = S_0$ eigenstate. In addition, a brief look at the behaviour of a high-spin coherent state provides us with a way of extracting physically meaningful SDs

that are expected to be approximate eigenstates of S_z. We note that for a ferromagnetically ordered case, a high-spin product function of $2S$ rotated χ_+ spinors, $|S(\theta,\phi)\rangle = \prod_{i=1}^{2S} |\chi_+^i\rangle$, such that the total spin vector is now oriented along the quantization axis given by the angles θ and ϕ, can be reexpanded in terms of the original $|SM\rangle$ states, quantized along the easy axis, according to:

$$|S(\theta,\phi)\rangle = \sum_{M=-S}^{S} \binom{2S}{S-M}^{1/2} \cos^{S+M}(\frac{\theta}{2}) \sin^{S-M}(\frac{\theta}{2}) \times e^{i(S-M)\phi}|SM\rangle. \quad (4)$$

For this spin coherent state, choosing $2S+1$ values of θ given by $S\cos(\theta_M) = M$ leads to $\langle S_z\rangle = M$. Accordingly, we expect the expectation values of S_z to be close to the values of M, once the same choice of the θ angles is made (see Fig. 1). Indeed, this choice leads to (almost) integer or half-integer values of $\langle S_z\rangle$ regardless of the choice of ϕ. Furthermore, choosing $\phi_M = M\phi_0$ (Fig. 1) leads to destructive interference in the off-diagonal elements of the many-body states and aids in producing approximate S_z eigenstates. Thus we obtain a set of $2S+1$ nearly orthonormal linearly independent many-body SDs with $\langle S_z\rangle$ taking on values akin to the magnetic quantum numbers $M = -S, -S+1, \ldots, S$. We call such a set of states a *spin multiplet*. For the case of $S = 10$ (neutral molecule), explicit calculations show that setting $\phi_0 = 34^\circ$ produces the smallest off-diagonal overlaps between approximate S_z eigenstates. With this choice of the phase factor, several figures of merit can be used to assess the error in the approximate S_z states. For example, the diagonal coefficients range has magnitudes between 0.4 and 1.0, and the average projection onto other states is approximately 0.2.

B. Results and discussion

We have carried out calculations for the neutral, cationic and anionic states of the Mn_{12} molecule. In Table 1, the moments, GS energies, HOMO and LUMO levels, as well as the MAE are shown as a function of charge. One of the important results here is determining the magnetic moment of the charged molecule: our calculation shows that the energy is minimized for $S = 21/2$ $(19/2)$ in the case of the anion (cation), that is, adding an electron to the molecule increases the molecule spin. The GS energy of the molecule decreases with adding an electron to the molecule. The positive electron affinity simply means that the

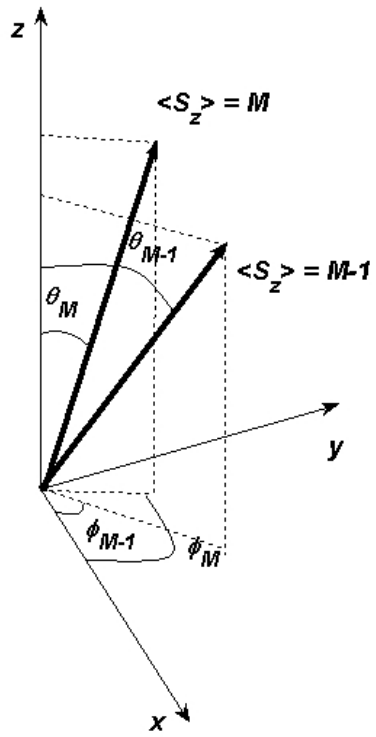

FIG. 1: The constraints imposed on $\langle S_z \rangle$ for the purpose of generating approximate many-body states: $S\cos(\theta_M) = M$ and $\phi_M = M\phi_0$. Two subsequent values of $\langle S_z \rangle$ are shown.

isolated molecule will have a tendency to attract an extra electron. However, it by no means implies that the molecule attached to external leads should have an excessive charge while at the offset of transport, since now, as we argue in the second part of this paper, one has to take into account the work function of the leads, and that makes the neutral (and not the anionic) charge state the state from which transport is initiated.

TABLE I: The GS properties from DFT: spin, energy, frontier-orbital energies for the neutral molecule (and their shift as one electron is added (removed) to (from) the molecule) and magnetic anisotropy energy as a function of charge

State	Q	Spin	Energy (eV)	Neutral HOMO (eV)	Neutral LUMO (eV)	MAE (K)	MAE (meV)
Anion	-e	21/2	-3.08	-2.28	-1.73	137	11.8
Neutral	0	20/2	0.00	-4.86	-4.43	55	4.7
Cation	+e	19/2	6.16	-7.45	-7.00	69	5.9

The energies for the low-lying spin-multiplets of the three charge states are plotted in Fig. 2 as a function of $\langle S_z \rangle$. We note that the anion and cation have a few low-lying excited spin multiplets besides the ground-state spin multiplet. In the case of neutral Mn_{12}, previous DFT calculations published by one of us [24] have shown that, while there is a large energy gap of the order of 0.5 eV between the HOMO and the LUMO for the neutral molecule (Table 1), the next unoccupied molecular level (LUMO+1) is a two-fold degenerate state which is only 8 meV above the LUMO. When one electron is added to the molecule, the new HOMO is only a few meV below the new LUMO. A similar situation happens for the cation: when an electron is taken away from the molecule, the HOMO has a narrowly avoided crossing with the LUMO. There is an analogy with the case of impurities in a semiconductor that can help understand this point. Neutral Mn_{12} behaves like an intrinsic semiconductor, which at zero temperature is an insulator with a gap separating a filled valence band from an empty conduction band. The Mn_{12} anion corresponds to adding a donor impurity to the semiconductor. Now the new Fermi level is very close to empty states of the conduction band and has therefore metallic properties. Similarly the cation behaves like an acceptor added to the system, with a hole state very close in energy to the highest occupied valence states. Both anion and cation molecules are therefore characterized by very small HOMO-LUMO gaps.

We note that charging or discharging the neutral molecule yield rigid shifts of the neutral-molecule HOMO and LUMO levels, with the energy gap essentially unchanged (Table 1); however, we have to remember that these levels are no longer frontier orbitals when one electron has been added (removed) to (from) the molecule. The new HOMO and LUMO levels for the charge states are in fact quasi-degenerate, as we explain above.

These orbital quasi-degeneracies in the single particle spectrum are responsible for the occurrence of excited spin-multiplets just above the ground-state spin multiplet, with the same total spin. Typically, the level spacing within each spin-multiplet is of the order of 0.1-1 meV, while different multiplets are separated by energies of the order of 10 meV.

For transport calculations, we need the absolute values of matrix elements

$$\langle \Phi(\mathbf{p}; 1, 2, \ldots N-1) | c_k(\mathbf{p}') | \Phi(\mathbf{p}'; 1, 2, \ldots N) \rangle, \tag{5}$$

where $c_k(\mathbf{p}')$ is a destruction operator that removes orbital $\phi_k(\mathbf{p}')$ from the SD $|\Phi(\mathbf{p}'; 1, 2, \ldots N)\rangle$ thus creating an $(N-1)$-particle many-body state from an N-particle

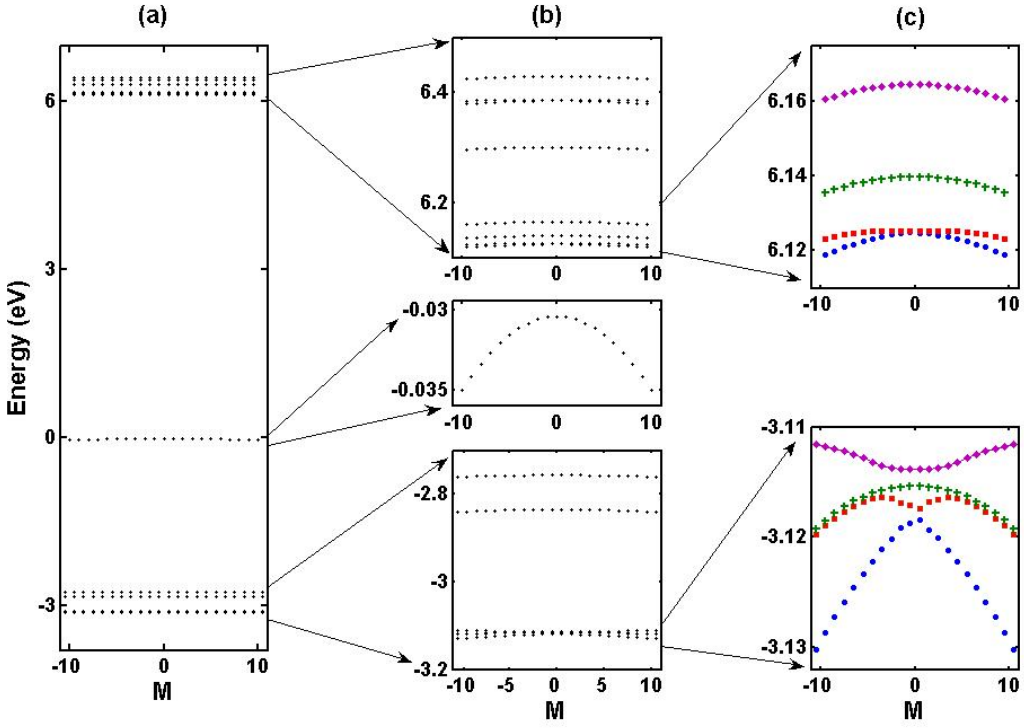

FIG. 2: (color online) (a) The energy spectrum of the three charge states plotted in the same energy scale. (b) A zoom-in of the spectra for the cation, neutral molecule and anion (from top to bottom). (c) A zoom-in of the lowest-lying multiplets for the cation (top) and anion (bottom).

many-body state. This change of the excess charge corresponds to an electron being removed from the molecule due to, e.g., a transport process. In order to evaluate the above many-body overlap, it is necessary to expand the single-particle orbitals for OVP $\mathbf{p}$ in terms of the single-particle orbitals of OVP $\mathbf{p}'$. Transition matrix elements relevant for low-bias transport are shown in Fig. 3, where we also added, for comparison, a plot of the matrix elements in the case of the giant-spin model, which are given entirely by the Clebsch-Gordan coefficients.

In Fig. 2 we see that the energies corresponding to $\langle S_z \rangle = M$ and $\langle S_z \rangle = -M$ are not identical. In addition, the overlaps between states of different charge do not preserve the $M \to -M$ symmetry in Fig. 3. This apparent (albeit small) violation of Kramer's degeneracy stems from a trade-off between choosing spin coherent eigenstates that are as orthogonal as possible (accomplished with our choice of the best wrapping angle $\phi_M = M\phi_0$), and dealing with the absence of perfect cylindrical symmetry of the molecular magnet Mn_{12},

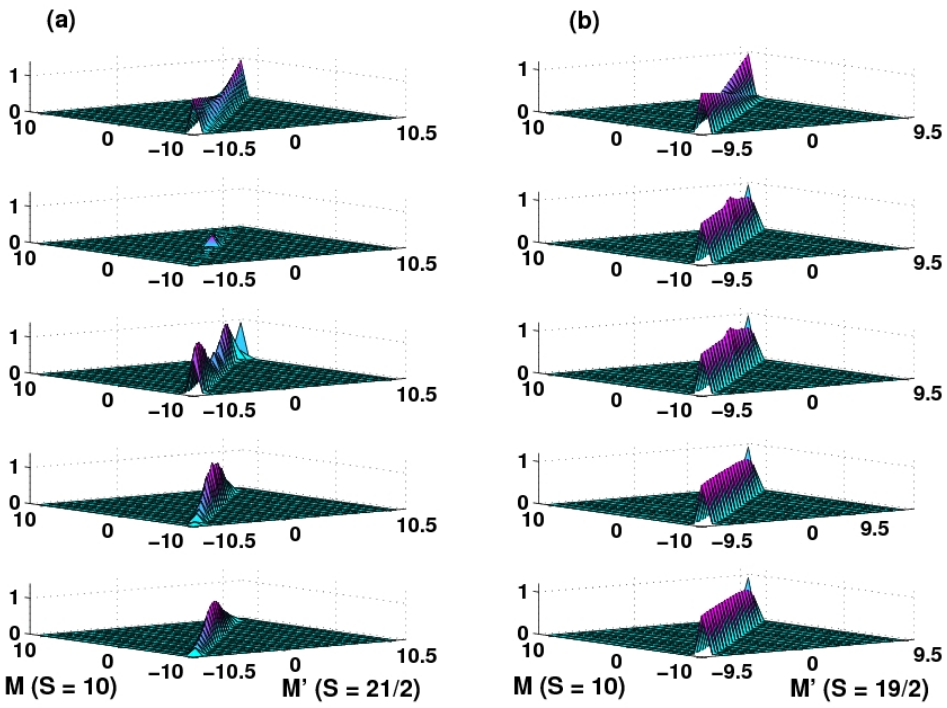

FIG. 3: (color online) Matrix elements for transitions between neutral and anionic (a) and cationic (b) charge states. From top to bottom: giant-spin model, transitions from the neutral GS spin multiplet to the anionic (a) and cationic (b) GS spin multiplets, transitions from the neutral GS spin multiplet to the anionic (a) and cationic (b) first, second and third excited spin multiplets.

which generates transverse anisotropy terms. If the symmetry was perfectly cylindrical, our construction would trivially give doubly degenerate eigenstates. The small term that breaks the cylindrical symmetry is exactly the order of magnitude of our approximation. Alternatively, we could choose S pairs of spin-coherent states (θ_M, ϕ_M) and (θ_{-M}, ϕ_M) that comply with the symmetry of Mn_{12} and would therefore be degenerate. Unfortunately these states would have larger (off-diagonal) overlaps with each other and therefore would be less suitable in the transport calculation.

Also presented in Table 1 is the magnetic anisotropy of each reference state that is determined from exact diagonalization of the spin-orbit interaction. As indicated in the table, when a *delocalized* electron is added to the neutral Mn_{12} molecule the anisotropy increases. As shown explicitly in Ref. [23], the anisotropy barrier in the Mn_{12} molecule is enhanced mostly due to the second order energy shifts in the $V_{\mathrm{s-o}}$ potential between

occupied and unoccupied states; both the spatial overlaps between these states and small energy denominators are important. For the neutral molecule there is a large HOMO-LUMO gap, while for the charged states this gap is very small, which leads to a quasi-degeneracy of the HOMO and LUMO states for the charged molecule. Hence, the energy denominators are smaller for the charged states thus leading to a stronger enhancement of the anisotropy. To see exactly how this enhancement happens, it is instructive to look at a simple model developed by Skomski [26]. Consider two d-electron orbitals $|\Psi_1\rangle = |xy\rangle$ and $|\Psi_2\rangle = |x^2 - y^2\rangle$ in a crystal field that splits their otherwise identical energy by $2A$, where $A > 0$, as the following Hamiltonian describes it:

$$H_0 = \begin{pmatrix} A & 0 \\ 0 & -A \end{pmatrix}.$$

Now, add to this Hamiltonian, as a small perturbation, the spin-orbit coupling $V_{\mathrm{s-o}} = \xi \mathbf{L}\cdot\mathbf{S}$, where ξ has the units of an energy. By treating the spin $\mathbf{S}$ as a classical vector that makes angle θ with the z-axis, one can show that

$$H = H_0 + V_{\mathrm{s-o}} = \begin{pmatrix} A & 0 \\ 0 & -A \end{pmatrix} + 2\xi\cos\theta \begin{pmatrix} A & 0 \\ 0 & -A \end{pmatrix}.$$

Diagonalization of the above Hamiltonian yields two energy eigenvalues:

$$E_{\pm} = \pm\sqrt{A^2 + 4\xi^2\cos^2\theta}. \tag{6}$$

If we now assume that only the lowest level E_- is occupied, then the total energy is $E_-(\theta)$ and it reaches its minimum for $\theta = 0, \pi$. These angles determine the z-axis to be the easy axis of our two-level system. The anisotropy energy is defined as

$$E_{\mathrm{a}} = E_-^{\text{hard plane}} - E_-^{\text{easy axis}} = E_-(\theta = \frac{\pi}{2}) - E_-(\theta = 0, \pi) \tag{7}$$

and becomes equal to

$$E_{\mathrm{a}} = \sqrt{A^2 + 4\xi^2} - A = \frac{2\xi^2}{A}, \tag{8}$$

where we assumed $\xi << A$. The ξ^2/A dependence transcends this simple model and generally applies to 3d anisotropies obtained by perturbation theory [26]. From this dependence

we see more clearly why the anisotropy becomes enhanced when the two levels mixed by the spin-orbit coupling are quasi-degenerate. This mixing, due to the spatial components of the wave functions, is obviously stronger if we allow the added electron to spread over the whole molecule (as we do in our calculation) than if we make it localize in one region of the molecule.

An important property in transport phenomena is the charging energy, that is, the energy required to add one electron to the system in question. In transport calculations, the charging energy is often accounted for by a Hubbard term (so called Hubbard U) in the total Hamiltonian of the system coupled to a source and drain. In our case this energy is not assumed to be some constant parameter U, as electron-electron interactions are included in the very DFT calculation, which is performed independently for the molecule with different values of Q. It is, nevertheless, possible to extract values of the charging energy from our calculations. Mn_{12} has a closed-shell neutral state, so the charging energies for the neutral HOMO and LUMO are not equal to each other. The value of the charging energy can be determined most easily by calculating the derivatives of the HOMO and LUMO eigenvalues with respect to charge. Thus, in practice, a couple of additional self-consistent calculations, in which we change Q by a small fraction, on either of the Q ground states yields the charging energy for the given frontier orbital. For the neutral molecule we find the charging energy, U, of 2.61 eV for the HOMO and 2.75 eV for the LUMO. These values are entirely consistent with trends for U in other molecules. For instance C_{60} (size of 1.3 nm) has a Hubbard U of approximately 3.0 eV [25] and the smaller C_{28} fullerene has a U of approximately 4.1 eV [27]. While the charging energy U of the Mn_{12} molecule is slightly dependent upon which occupied or unoccupied state is vacated or filled, variations in this parameter are negligibly small.

III. TRANSPORT CALCULATION

A. Method

Equipped with the microscopic spectrum of the total energies for different charge states of the Mn_{12}-molecule and the overlaps for the transitions between these energy states, we are now ready to launch on the transport calculation for a SET with Mn_{12}-ac as its central island

(Fig. 4). The molecule is assumed to be weakly coupled, through tunneling barriers, to two external normal-metal leads. The weakness of the coupling means that the broadening of the molecular many-body energy levels due to tunneling is negligible, and that electrons tunnel onto and off the molecule in a one-by-one fashion (so called sequential-tunneling regime). The time between two consecutive tunneling events is much longer that the energy-relaxation time in the molecule (that is, the molecule is back in its equilibrium before the next electron hops onto or from it).

The Hamiltonian of the external lead α (where $\alpha =$ L or R) describes a normal Fermi liquid

$$H_\alpha = \sum_l \epsilon_{\alpha l} a^\dagger_{\alpha l} a_{\alpha l}, \tag{9}$$

where $a^\dagger_{\alpha l}$ and $a_{\alpha l}$ denote creation and destruction operators, respectively, of a quasiparticle given by the quantum number l in lead α. The quasiparticle energies $\epsilon_{\alpha l}$ are measured with respect to the electrochemical potential μ_α of a given lead. The tunneling Hamiltonian, that stands for the lead-island coupling is given by

$$H_{\rm T} = \sum_{\alpha,l} \sum_{k,\mathbf{p}} \left(t_{\alpha l} a^\dagger_{\alpha l} c_k(\mathbf{p}) + \text{h.c.} \right), \tag{10}$$

where $c^\dagger_k$ (c_k) creates (destroys) an electron in orbital k in the molecule. The tunneling constant $t_{\alpha l}$ depends on the tunneling barrier in the contact region between lead α and the molecule. In principle it depends on the energy $\epsilon_{\alpha l}$ of the tunneling electron, but we disregard that in the following calculation.

In the weak-coupling regime, the tunneling Hamiltonian (10) is treated perturbatively and the tunneling rates for transitions between states defined by two different parameter vectors $\mathbf{p}'$ and $\mathbf{p}$ are calculated by virtue of the Fermi golden rule. The final shape of the transition rate for going from state $\mathbf{p}$ to state $\mathbf{p}'$ becomes

$$\begin{aligned} \Gamma^{\alpha+}_{\mathbf{p}',\mathbf{p}} \; = & \frac{2\pi}{\hbar} \Gamma_\alpha f\left(E(\mathbf{p}', k'_i, N_{Q'}) - E(\mathbf{p}, k_i, N_Q) - \mu_\alpha \right) \times \\ & \left| \langle \mathbf{p}'; k'_1, k'_2, \ldots, k'_{N_{Q'}} | c^\dagger_k(\mathbf{p}) | \mathbf{p}; k_1, k_2, \ldots, k_{N_Q} \rangle \right|^2 \end{aligned} \tag{11}$$

for tunneling onto the molecule, and

$$\begin{aligned} \Gamma^{\alpha-}_{\mathbf{p}',\mathbf{p}} \; = & \frac{2\pi}{\hbar} \Gamma_\alpha \left[1 - f\left(E(\mathbf{p}, k_i, N_Q) - E(\mathbf{p}', k'_i, N_{Q'}) - \mu_\alpha \right) \right] \times \\ & \left| \langle \mathbf{p}'; k'_1, k'_2, \ldots, k'_{N_{Q'}} | c_k(\mathbf{p}) | \mathbf{p}; k_1, k_2, \ldots, k_{N_Q} \rangle \right|^2 \end{aligned} \tag{12}$$

for tunneling off the molecule. Here $\Gamma_\alpha = \sum_l |t_{\alpha l}|^2$ describes the tunneling rate through junction α, $f(\epsilon - \mu_\alpha)$ is the Fermi-Dirac distribution function for energy ϵ in lead α. The charging (discharging) tunneling rate corresponds to the charge change $Q' - Q = \mp e$ (where $e > 0$) on the molecule or, in other words, to $N_{Q'} - N_Q \pm 1$, the change in the electron occupation of the molecule. Our SDFT calculations have shown also that $\left\langle S_{N_{Q'}} \right\rangle - \left\langle S_{N_Q} \right\rangle = \pm 1/2$ for charging and discharging the molecule, respectively.

We note here that the parameter vector reduces in practice to $\mathbf{p} = (Q, \mathbf{M}, \theta, \phi)$ for $\mathbf{E}, \mathbf{B} = 0$. Since the last three arguments of $\mathbf{p}$ describe essentially the expectation values for the molecule spin, $\langle S \rangle$ and $\langle S_z \rangle$, it is possible to express $\mathbf{p}$ as $\mathbf{p} = (Q, S, M)$, where S and M are akin to the usual spin quantum numbers. In this way, states $\mathbf{p}$ label directly the total-energy levels within the multiplets of Fig. 2 in Section III and can be put in a one-to-one correspondence (within each multiplet) to the $|S, M\rangle$ eigenstates of the phenomenological giant-spin model:

$$H_{S_Q} = \sum_{i,n} D_{S_Q,i,n} \left(S^z_{Q,i} \right)^n , \tag{13}$$

which is given in terms of spin variables $\mathbf{S}_{Q,i}$ for each spin multiplet i of charge state Q; $D_{S_Q,i,n}$ are anisotropy constants extracted from the SDFT spectra of Fig. 2. This identification facilitates a comparison between the SDFT- and giant-spin-model-based conductance calculations. The energies for the spin model are thus given by Eq. (13). In order to determine the transition overlaps between different $|S, M\rangle$ states, we observe that adding (taking away) an electron to the molecule with the total spin $\mathbf{S}$ is equivalent to adding the spin angular momentum of the added (subtracted) electron $\mathbf{s}$ ($s = 1/2$) to the spin momentum $\mathbf{S}$ of the molecule before the electron addition (subtraction) [28]. The addition of angular momenta yields $\langle S', M' | S, M \rangle$ overlaps in terms of a product of the Clebsch-Gordan coefficients and a factor which depends on the t tunneling coefficient in Eq. (10). In the numerical calculations, we choose this factor arbitrarily in such a way so that the largest overlap for the SM has the same order of magnitude as that from the SDFT calculations; in practice, this t-dependent factor has a dimensionless value of 20.

By using the rates given by Eqs. (11) and (12), we find the electric current through the

tunneling barrier between the molecule and lead α:

$$I_\alpha = -e \sum_{\mathbf{p}\mathbf{p}'} P_{\mathbf{p}} \left(\Gamma^{\alpha+}_{\mathbf{p}'\mathbf{p}} - \Gamma^{\alpha-}_{\mathbf{p}'\mathbf{p}} \right) =$$

$$= -e \sum_{M,i;M',i'} P_{Q=0,S=10,M,i} \left(\Gamma^{\alpha+}_{Q-e,S'=S+1/2,M',i';Q,S,M,i} - \Gamma^{\alpha-}_{Q+e,S'=S-1/2,M',i';Q,S,M,i} \right), \quad (14)$$

where we made use of the fact that $S = 10$ for the neutral molecule ($Q = 0$), and $P_{\mathbf{p}}$ (or, more specifically, $P_{Q,S,M,i}$) is the probability that the molecule is in the state given by $\mathbf{p} \equiv (Q, S, M, i)$. The probabilities $P_{\mathbf{p}}$ are the numerical solution to the system of master equations in the steady-state condition:

$$\frac{\mathrm{d}\hat{P}}{\mathrm{d}t} = \hat{A}\hat{P} = 0, \quad (15)$$

with the probability normalization condition $\sum_{\mathbf{p}} P_{\mathbf{p}}$. Here $\hat{P}$ is a vector whose components are the individual-state probabilities $P_{\mathbf{p}}$. The matrix $\hat{A}$ contains all possible transition rates given in Eqs. (11) and (12).

On top of the microscopic energy levels of the molecule, the transport in our SET is governed by the usual, transistor-like, electrostatics [29, 30], as shown in Fig. 4. C_{L}, C_{R} and C_{g} represent the capacitances that describe the left and the right junction, and the coupling to the gate electrode, respectively. The electrostatic modification of the energy spectrum of Mn_{12} appears via the gate voltage V_{g} together with the gate capacitance C_{g}. Across the double junction, a bias voltage V_{b} is applied which shifts the Fermi levels of the left and right electrodes, as sketched in Fig. 5, according to $\mu_{\mathrm{L}} - \mu_{\mathrm{R}} = (E_{\mathrm{F}} + eV_{\mathrm{b}}/2) - (E_{\mathrm{F}} - eV_{\mathrm{b}}/2) = eV_{\mathrm{b}}$. The work function, which determines how far from the vacuum level the equilibrium (i.e., for $V_{\mathrm{b}} = 0$) chemical potentials of the two leads (E_{F}) are, makes the neutral-charge state favorable when the gate and bias voltages are zero (see Fig. 5).

B. Singularity of the rates matrix

Before we proceed to a presentation and analysis of the numerical results of the previous section, it is important to mention a certain numerical difficulty one encounters while carrying out master-equation based SET calculations with our molecule as the central electrode. Not only is the energy spectrum of the Mn_{12} molecule discrete and rich, as we see in Fig. 2, but its energy levels that belong to different charge states of the molecule are also relatively

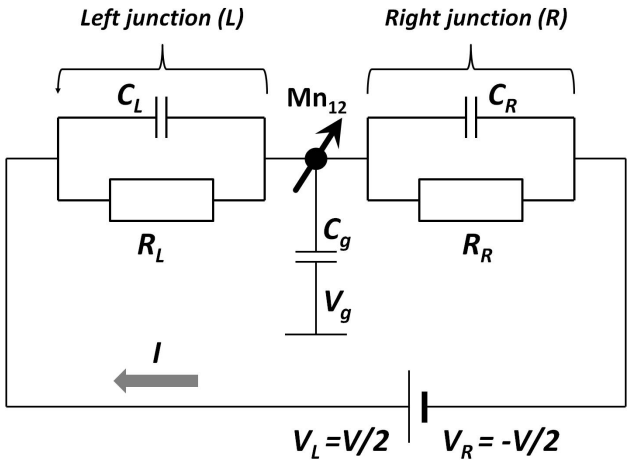

FIG. 4: Studied SET with the Mn_{12} molecule as a central electrode in a typical transistor-like dc-circuit.

weakly interconnected (Fig. 3). As a matter of fact, most of the levels are not connected at all, at least if we are to treat the zeros of the SDFT calculation for the transition overlaps as exact zeros. The vanishing of the transition overlaps for a majority of energy levels leads to a singularity of matrix $\hat{A}$ in Eq. (15). This singularity must be somehow removed.

One way of circumventing this obvious problem is to couple the levels within a given spin multiplet by the use of a certain "phonon bath". This phonon bath makes the excited states within a given spin multiplet relax to the multiplet's GS, and that relaxation depends on the bath temperature $T_{\rm bath}$. This method proves to be efficient inasmuch as it removes the troublesome singularity. However, there is one important drawback in letting the excited states relax: it complicates and changes the physical situation of the whole transport system. In particular, the transition overlaps given by the SDFT are effectively and severely modified now, as the excited states become largely depopulated due to the "phonon"-assisted relaxation. The transport becomes now dominated by the transitions between the GSs of the spin multiplets belonging to different charge states. Clearly, another approach is in place.

Another way of solving the problem of the singularity of the rates matrix $\hat{A}$ boils down to a realization that the zeros in the SDFT overlaps are *not* exact zeros; they are instead – as any result of any numerical simulation is – given with a finite uncertainty. Reasoning like this, we replace by hand the zeros in the transition-overlap matrices with a small parameter a. We find that $\hat{A}$ is not singular for $a > 10^{-14}$. Then we study the change in the value

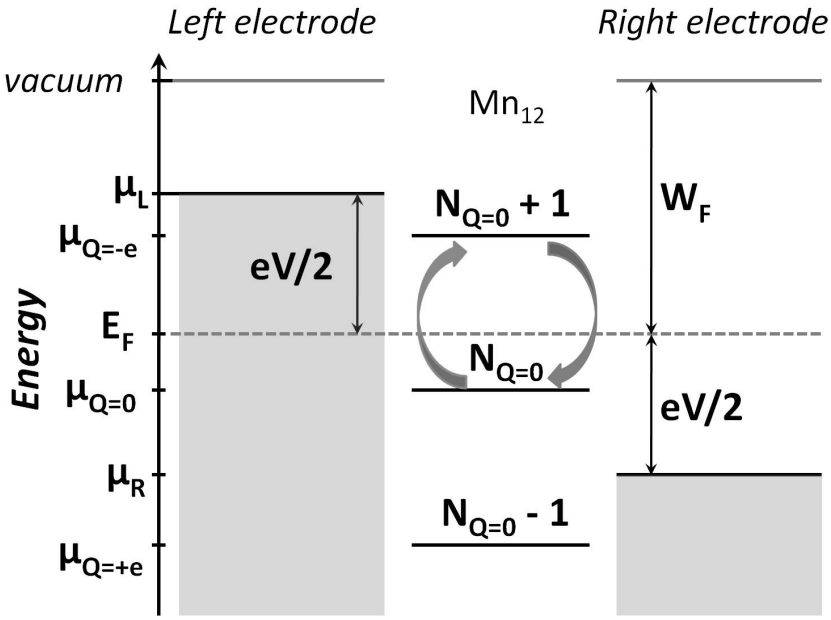

FIG. 5: Energy cartoon of the studied SET with the Mn_{12} molecule as a central electrode. The chemical potential of lead L (R) is shifted upwards (downwards) due to the bias voltage $V_{\rm b}$. The work function $W_{\rm F}$ determines the distance from the equilibrium chemical potential $E_{\rm F}$ to the vacuum level; we assume the value for gold (≈ 5 eV). The chemical potential of the molecule is plotted for the GSs of the three charge states ($Q = -1, 0, 1$ in units of e). The values of the chemical potential for the neutral molecule, $\mu_{Q=0}$, and for the anion $\mu_{Q=-e}$, lie in the energy window between $\mu_{\rm L}$ and $\mu_{\rm R}$ for the bias voltages given in the figure, which means that these two charge states participate in transport (the curvy arrows). Whenever the chemical potentials of the external leads cross the chemical potential for the charged states of the molecule, transport channels open.

of the current when a is varied, and find that the current does not change more than by a 5×10^{-6} fraction of its value for the range $10^{-13} < a < 10^{-8}$, which means that the current is quite stable with respect to the changes in a. We then choose $a = 10^{-10}$ and carry out the Coulomb-blockade transport calculation as described in the A part of the present section.

Obviously, this new method of dealing with the singularity of $\hat{A}$ is not free of drawbacks. In particular, one has to point out that now each level of a given spin multiplet of a given charge is coupled to each level of any other spin multiplet of a different charge, even though this extra coupling is very small. Adding a to the overlaps opens a multitude of additional

transport channels that otherwise would have stayed closed. However, adding a will not change the value of the current substantially, so the influence on the $I(V_{\rm b})$ curves is irrelevant. One could see the procedure of introducing a as some kind of a low-temperature fluctuation that joins all the energy levels and makes them relax one to another. After all, this is what temperature does in the real-life experiments on SETs.

C. Results and discussion

The numerical calculations are done at zero temperature. The molecule couples to the two leads with equal strength (symmetric double junction); the gate capacitance is equal to 1/20 of the total capacitance of the system. The zero matrix elements of both SDFT and SM overlaps are replaced with $a = 10^{-10}$. We plot the current-voltage characteristic of our Mn_{12} SET for two values of the gate voltage: $V_{\rm g} = -20$ and 10 V. In order to see exactly how the orbital degrees of freedom reveal themselves in the SDFT-based calculation, we plot $I(V_{\rm b})$ characteristics for both the uniaxial giant-spin model (SM) of Eq. (13) and the SDFT approach in Fig. 6. The blue (red) color corresponds to the negative (positive) value of the gate voltage. We note that the blue $I(V_{\rm b})$ curve ($V_{\rm g} = -20$ V) starts off much more rapidly for SM (dashed line) than for SDFT (solid line).

In order to understand why this happens, it is instructive to take a look at the transition overlaps (Fig. 3(a)) between the neutral and anionic GS spin multiplets, both for SM and SDFT. We see from Fig. 3(a) (the two plots on the top) that the two overlaps differ substantially. The SM overlap connects well the GS levels (largest $|M|$ and $|M'|$) of the neutral and anionic GS spin multiplets, while the SDFT overlap does *not*. This lack of connection between the GS levels for SDFT leads to a current suppression at the onset of transport (solid blue line in Fig. 6). The negligibility of this connection is also responsible for the drop in current visible in the solid red $I(V_{\rm b})$ curve ($V_{\rm g} = 10$ V). When this drop takes place, the anion-to-neutral transport channel opens, the GS multiplet of the anion becomes occupied, but since it is only weakly connected to the neutral GS multiplet, the system gets trapped in the GS anion multiplet, and that leads to the noted drop in current or, in other words, to a NDC dip (see also the two-dimensional conductance plot and other transport results in our earlier work [19]). From this difference between a purely-spin SM and the SDFT-based calculation that includes the spatial degrees of freedom, we draw a conclusion that the spa-

tial selection rules can and do, indeed, override the spin selection rules and affect transport dramatically, leading to current suppression and NDC.

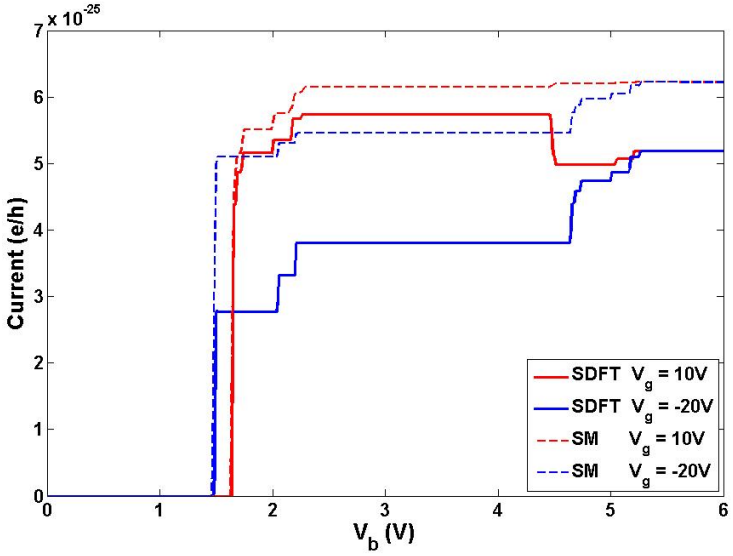

FIG. 6: (color online) Theoretical current-voltage characteristic for the Mn_{12} SET. The solid (dashed) lines correspond to the calculation done within the SDFT (SM) approach. The blue (red) line represents the $I(V_b)$ curve for $V_g = -20$ V ($V_g = 10$ V). The double junction is symmetric, and the gate capacitance is 1/20 of the total capacitance; the temperature is zero.

IV. SUMMARY

In conclusion, we presented a more detailed description of our SDFT method of calculating the many-body properties of the Mn_{12}-ac molecule and discussed the results of this method more extensively than in our previous work [19]. In particular, we present the full many-body energy spectrum of the molecule and attribute its asymmetry with respect to the M spin quantum number to the imperfection of the uniaxial symmetry of the molecule, which is manifested by the presence of transverse anisotropy terms. We explained in detail, by using a toy-model example, why the anisotropy becomes enhanced when the HOMO and LUMO levels mixed by the spin-orbit coupling are quasi-degenerate. The charging energy of the molecule was estimated, and the estimate was judged consistent with SET experiments on other molecules.

We also compared the current-voltage characteristics for the SDFT-based approach and the giant-spin model. A current suppression and NDC is observed for the former one, while the latter one does not exhibit these features. We attribute these features to the suppression of the SDFT transition rates between the GS spin multiplets of different charge. This transistion-rate suppression is a result of including orbital degrees of freedom in the SDFT calculation. Since the linear master-equation system in our simulation is singular due to the sparseness of the transition rates (both in SDFT and SM), we proposed a way of solving this numerical issue.

The Mn_{12} molecule, though in many respects outstanding as an SMM, reacts strongly with the environment (e.g., when attached to a metallic electrode), which makes transport measurements very difficult and hard to reproduce [7, 8]. However, there exist more robust SMMs that do not loose their magnetic properties when attached to surfaces. Transport experiments on these SMMs [31, 32] are more easily reproducible. Thus one possible extension of our work would be to do an SDFT calculation for these smaller molecular magnets and then compare it to the appropriate spin models. The coupling of the SMM to the external leads can be modeled more realistically by including explicitly the magnetic and electric fields in the SDFT approach. Another possibility for future research stems from the fact that higher-order tunneling processes contribute to the transport in some of these smaller and robust SMMs [32]. Consequently, extending the master-equation technique beyond the sequential-tunneling limit, in particular by taking into account cotunneling processes, seems to be a natural road to follow.

Acknowledgements. We would like to express our gratitude to Vincenzo G. Benza for help in developing the ab-initio approach, understanding its results and applying them to the transport calculations. We would also like to thank Magnus Paulsson for help with overcoming the numerical intricacies of the transport calculations.

---

[1] L. Bogani and W. Wernsdorfer, Nature Mater. **7**, 179 (2008).

[2] D. Gatteschi, R. Sessoli and J. Villain, *Molecular Nanomagnets* (Oxford, New York, 2006).

[3] R. Sessoli *et al.*, Nature **365**, 141 (1993).

[4] L. Thomas *et al.*, Nature **383**, 145 (1996).

[5] J. R. Friedman *et al.*, Phys. Rev. Lett. **76**, 3830 (1996).

[6] W. Wernsdorfer and R. Sessoli, Science **284**, 133 (1999).

[7] H. B. Heersche *et al.*, Phys. Rev. Lett. **96**, 206801 (2006).

[8] M. H. Jo *et al.*, Nano Lett. **6**, 2014 (2006).

[9] C. Romeike, M. R. Wegewijs, and H. Schoeller, Phys. Rev. Lett. **96**, 196805 (2006).

[10] C. Timm and F. Elste, Phys. Rev. B **73**, 235304 (2006).

[11] M.N. Leuenberger and E.R. Mucciolo, Phys. Rev. Lett. **97**, 126601 (2006).

[12] C. Timm, Phys. Rev. B **76**, 014421 (2007).

[13] F. Elste and C. Timm, Phys. Rev. B **75**, 195341 (2007).

[14] C. Romeike *et al.*, Phys. Rev. B **75**, 064404 (2007).

[15] G. Gonzalez, M. N. Leuenberger and E.R. Mucciolo, Phys. Rev. B **78**, 054445 (2008).

[16] J. Lehmann and D. Loss, Phys. Rev. Lett. **98**, 117203 (2007).

[17] S. Barraza-Lopez *et al.*, Phys. Rev. Lett. **102**, 246801 (2009).

[18] C. D. Pemmaraju, I. Rungger, and S. Sanvito, Phys. Rev. B **80**, 104422 (2009).

[19] Ł. Michalak, C. M. Canali, M. R. Pederson, M. Paulsson, and V. G. Benza, Phys. Rev. Lett. **104**, 017202 (2010).

[20] J. Kortus, C. S. Hellberg, and M. R. Pederson, Phys. Rev. Lett. **86**, 3400 (2001).

[21] K. Park, M. R. Pederson, and C. S. Hellberg, Phys. Rev. B **69**, 014416 (2004).

[22] O. Waldmann and H. U. Guedel, Phys. Rev. B, **72**, 094422 (2005).

[23] M. R. Pederson and S. N. Khanna, Phys. Rev. B **60**, 9566 (1999).

[24] K. Park and M. R. Pederson, Phys. Rev. B **70**, 054414 (2004).

[25] M. R. Pederson and A. Quong, Phys. Rev. B **46**, 13584 (1992).

[26] R. Skomski, *Simple Models of Magnetism* (Oxford University Press, 2008).

[27] N. Laouini and M. R. Pederson, Phys. Rev. B **48**, 2733 (1993).

[28] C. M. Canali and A. H. MacDonald, Phys. Rev. Lett. **85**, 5623 (2000).

[29] S. Datta, *Quantum Transport: Atom to Transistor* (Cambridge University Press, 2005).

[30] J. Martinek and J. Barnaś, Spin-dependent transport in single-electron devices, in: *Concepts in Spin Electronics*, Ed. S. Maekawa (Oxford University Press, 2006).

[31] J. E. Grose *et al.*, Nature Mater. **7**, 884 (2008).

[32] E. A. Osorio *et al.*, Nano Lett. **10**, 105 (2010).

Paper IV

NANO LETTERS

2007
Vol. 7, No. 1
81−85

Probing Spin Accumulation in Ni/Au/Ni Single-Electron Transistors with Efficient Spin Injection and Detection Electrodes

R. S. Liu,[†,‡] H. Pettersson,*[,†,‡] L. Michalak,[§] C. M. Canali,[§] and L. Samuelson[‡]

Center for Applied Mathematics and Physics, Halmstad University, Box 823, SE-301 18 Halmstad, Sweden, Solid State Physics/ the Nanometer Structure Consortium, Lund University, Box 118, SE-22100 Lund, Sweden, and Department of Chemistry and Biomedical Sciences, Kalmar University, 391 82 Kalmar, Sweden

Received September 11, 2006; Revised Manuscript Received November 14, 2006

ABSTRACT

We have investigated spin accumulation in Ni/Au/Ni single-electron transistors assembled by atomic force microscopy. The fabrication technique is unique in that unconventional hybrid devices can be realized with unprecedented control, including real-time tunable tunnel resistances. A grid of Au disks, 30 nm in diameter and 30 nm thick, is prepared on a SiO_2 surface by conventional e-beam writing. Subsequently, 30 nm thick ferromagnetic Ni source, drain, and side-gate electrodes are formed in similar process steps. The width and length of the source and drain electrodes were different to exhibit different coercive switching fields. Tunnel barriers of NiO are realized by sequential Ar and O_2 plasma treatment. By use of an atomic force microscope with specially designed software, a single nonmagnetic Au nanodisk is positioned into the 25 nm gap between the source and drain electrodes. The resistance of the device is monitored in real time while the Au disk is manipulated step-by-step with angstrom-level precision. Transport measurements in magnetic field at 1.7 K reveal no clear spin accumulation in the device, which can be attributed to fast spin relaxation in the Au disk. From numerical simulations using the rate-equation approach of orthodox Coulomb blockade theory, we can put an upper bound of a few nanoseconds on the spin-relaxation time for electrons in the Au disk. To confirm the magnetic switching characteristics and spin injection efficiency of the Ni electrodes, we fabricated a test structure consisting of a Ni/NiO/Ni magnetic tunnel junction with asymmetric dimensions of the electrodes similar to those of the single-electron transistors. Magnetoresistance measurements on the test device exhibited clear signs of magnetic reversal and a maximum tunneling magnetoresistance of 10%, from which we deduced a spin polarization of about 22% in the Ni electrodes.

Electron tunneling through ferromagnetic junctions is of current interest due to expected applications in magnetic random access memories (MRAM), in read/write heads in hard disks, and in other spintronic devices.[1] Most of the experimental and theoretical work published up to now focuses on tunnel magnetoresistance (TMR) behavior in simple planar junctions. In this context, TMR implies an increase in the junction resistance when the magnetic moments of the two leads change from parallel to antiparallel alignment. More recently, spin-dependent tunneling in more complex systems, e.g., ferromagnetic single-electron transistors (F-SETs), has become an attractive topic for both experimental and theoretical studies.[2] In these devices, novel phenomena are expected to occur due to the interplay between charging effects and spin-dependent transport. Indeed, several experiments on F-SETs, starting with the seminal work by Ono et al.,[3,4] have demonstrated enhanced TMR,[3,5] and magneto-Coulomb oscillations of the TMR[4,6] as a function of external magnetic field and bias voltage. On the other hand theoretical work,[7−13] besides clarifying some of these earlier experimental observations, predicts that spin accumulation on the central island of an F-SET should manifest itself in a variety of effects showing up in the magnetoresistance properties. Spin accumulation, together with spin injection, is a key concept in spintronics, and refers to a nonequilibrium spin population created in confined structures by external magnetic fields or spin-polarized currents. So far experimental verification of spin accumulation in F-SETs has been elusive. Only very recently two experiments[14,15] have shown indirect evidence of its occurrence, albeit the interpretation of one of them[14] has been controversial.[16]

In the following, we use the notation F/F/F and F/N/F for SETs with ferromagnetic leads and a ferromagnetic central island or nonmagnetic island, respectively. One fundamental difference between F/F/F and F/N/F SETs is the connection between spin accumulation and TMR. For F/F/F SETs, a nonzero TMR can exist even in the case of vanishing spin

* Corresponding author. E-mail: Hakan.Pettersson@ide.hh.se.
† Halmstad University.
‡ Lund University.
§ Kalmar University.

10.1021/nl062146n CCC: $37.00
Published on Web 12/10/2006

accumulation on the central island.[7] In this case, discrete charging effects lead to TMR oscillations as a function of the bias voltage.[7] In contrast, for F/N/F SETs a net spin accumulation on the central island is necessary to observe a nonzero TMR at all. In this case the intrinsic spin-relaxation time on the central island is sufficiently long compared to the time interval between two successive tunneling events, so that a spin-polarized current generates a finite magnetic moment. The landmark of the occurrence of spin accumulation in both devices is a periodic sign change of the TMR as a function of the bias voltage, with dips directly related to the Fermi level splitting for electrons with different spin.[9,11−13] Such features were indeed observed in the experiment by Yakushiji et al.[15] on F-SETs with one magnetic lead and a central island consisting of a Co nanoparticle.

One important conclusion from ref 15 is that the crucial parameter that controls spin accumulation, namely the spin-relaxation time, τ_{RE}, is apparently strongly enhanced in nanoparticles over bulk structures. For instance, τ_{RE} in Co nanoparticles is enhanced up to hundreds of nanoseconds in comparison with tens of picoseconds in ferromagnetic layers. Among the possible reasons for such long τ_{RE} is the suppression of the spin−orbit mediated spin−flip scattering caused by the discreteness of the nanoparticle energy levels or by the properties of the matrix in which the nanoparticle is embedded.[17,18] It is fair to say, however, that spin-relaxation mechanisms in metal nanoparticles are at present not well understood.

In this paper, we demonstrate a novel type of SET design suitable for studying spin accumulation in well-controlled, strongly confined nanoparticles. The nanoparticle is in our case attached to a SiO_2 surface and not embedded in a disturbing matrix. We have chosen to study nanoscaled Au disks since no conclusive reports on the dependence of confinement on the spin-relaxation mechanism have been reported. In addition, Au is inherently interesting due to its very strong spin−orbit interaction.

In the present work, F/N/F SETs are fabricated on top of a 100 nm thick SiO_2 layer grown on a Si substrate (shown in Figure 1A). A grid of Au disks, 30 nm in diameter and 30 nm thick, is prepared by conventional electron-beam lithography followed by thermal evaporation and subsequent lift-off. Ferromagnetic Ni source and drain electrodes, 30 nm thick, 220 and 80 nm wide, 300 nm and 1.5 μm long, respectively, are formed in subsequent similar process steps together with a 30 nm thick Ni side-gate. Tunnel barriers of NiO are fabricated by sequential Ar plasma etching at a pressure of about 1.0×10^{-4} mbar for 5 min and O_2 plasma etching at a pressure of about 1.0×10^{-1} mbar for 3 min.

The width (80 nm) of the drain electrode is comparable to the size of single Ni domains,[19,20] while the source electrode is considerably wider (220 nm) and shorter (300 nm). Because of this shape anisotropy, the two electrodes will undergo magnetic reversal at different magnetic fields, confirmed by performing micromagnetic simulations using the OOMMF code[21] which give the coercivity field of 40 and 90 mT for the source and drain electrodes, respectively.

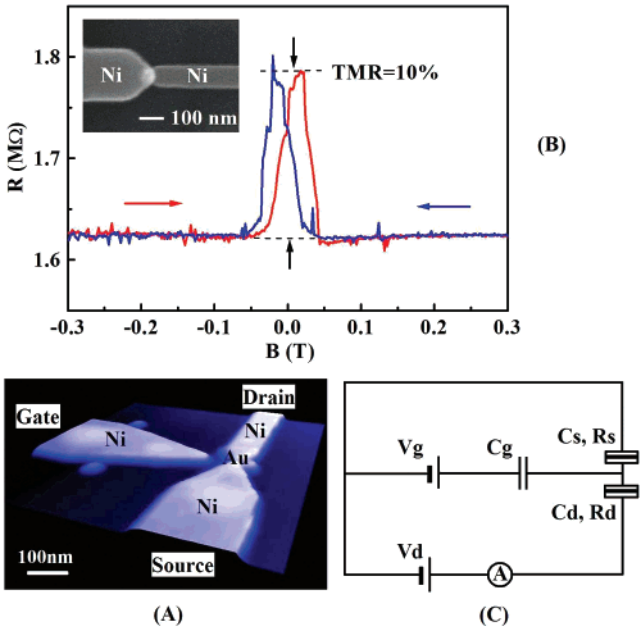

Figure 1. (A) Atomic force micrograph of the ferromagnetic SET studied in the present work. The device is fabricated on top of a 100 nm thick SiO_2 layer. (B) Switching behavior of a tunnel junction between two Ni electrodes separated by NiO as a function of magnetic field at 1.7 K. The inset shows a scanning electron micrograph of the device. (C) Schematic circuit diagram of the SET.

By sweeping the magnetic field, it should thus be possible to switch from parallel to antiparallel alignment of the magnetic moments in the two electrodes. The magnetic switching behavior and spin-injection efficiency of the electrodes is investigated in a test structure shown in the inset of Figure 1B. The test structure consists of a Ni/NiO/Ni magnetic tunnel junction with overlapping Ni electrodes of the same dimensions as those used for the SET. The junction was fabricated by first forming a Ni electrode using conventional methods. Following this, a sequence of plasma treatment steps forms the NiO tunnel barrier on top of the electrode. Subsequently, a second Ni top electrode is defined to overlap the bottom electrode with approximately 50 nm using a high-precision alignment procedure. Magnetoresistance measurements clearly show a maximum TMR signal of about 10% while sweeping the magnetic field (Figure 1B). This TMR signal provides strong support for that we can control the relative orientation of the magnetization of the two leads and, additionally, that the electrodes are efficient injectors of spin polarized current. Using Julliere's model,[22] $\mathrm{TMR} = (R_{AP} - R_P)/R_P = 2P^2/(1 - P^2)$, where R_P and R_{AP} are the resistances in parallel and antiparallel magnetic configurations, respectively, and P is the spin-polarization, we deduce a spin polarization of 22% in the Ni electrodes. This value is in good agreement with the tunneling spin polarization measured by Tedrow and Meservey in planar tunnel junction experiments.[23] It is noted that the magnetic switching occurs for slightly lower fields than expected from the OOMMF simulations, a discrepancy probably due to exchange bias introduced by the antiferromagnetic NiO.

After the real sample is mounted and bonded on a standard chip carrier, a Au nanodisk is positioned step-by-step with

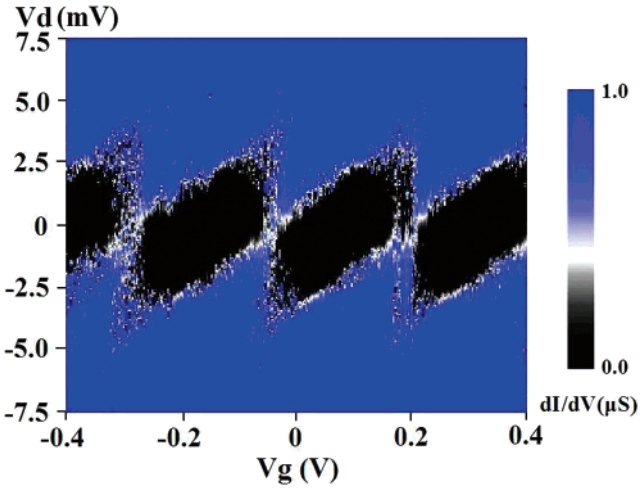

Figure 2. Color-coded plot of the differential conductance dI/dV as a function of drain−source voltage V_d and gate voltage V_g obtained at 4.2 K. The dark areas correspond to Coulomb blockade regions.

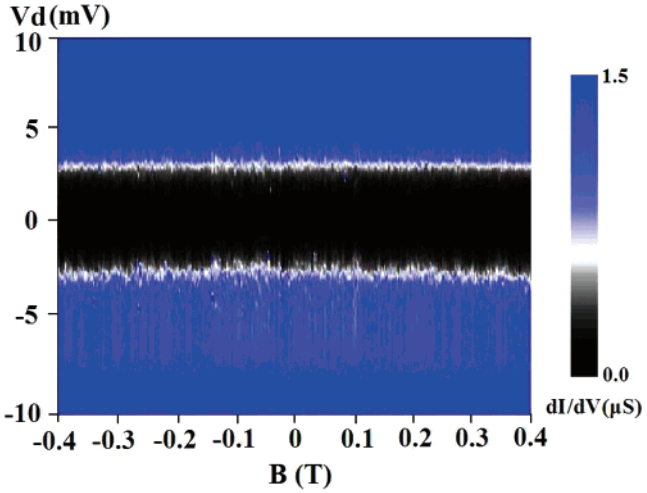

Figure 3. Color-coded plot of dI/dV obtained at 1.7 K as a function of the drain−source voltage V_d and magnetic field B at $V_g = 0$.

angstrom precision into the 25 nm gap between the drain and source electrodes using the atomic force microscopy (AFM) manipulation technique described in ref 24. The resistance of the device is monitored in real time, while the Au disk is manipulated, and the desired resistance (1 MΩ to 1 GΩ) for a good device can normally be obtained after merely a few attempts. For a given device, it is possible to tune the tunnel resistance by repositioning the Au disk. A fairly high fabrication yield of typically 10% is obtained. The present devices differ significantly from previously reported AFM-assembled devices in that the electrodes are ferromagnetic with plasma-processed NiO tunnel barriers and that only a single disk is used to bridge the gap between the source and drain electrodes. These substantial developments have resulted in well-controlled ferromagnetic SETs with long-term stability and a decreased fabrication complexity.[25] After the fabrication is completed, extensive conductance measurements are performed at 4.2 K in a liquid helium Dewar (schematic circuit diagram is shown in Figure 1C). Following these measurements, the sample is transferred to a cryostat housing a 6 T superconducting magnet where the magnetoresistance measurements were carried out at 1.7 K. The magnetic field is in the plane of the device with a tunable orientation with respect to the orientation of the electrodes.

Figure 2 shows a color-coded plot of the differential conductance dI/dV as a function of drain−source voltage V_d and gate voltage V_g. The dark areas correspond to Coulomb blockade regimes. The gate capacitance C_G is determined from the spacing between neighboring degeneracy points at $V_d = 0$ where dI/dV is nonzero, resulting in $C_G = e/(200\ \text{mV}) = 0.80$ aF. The asymmetry observed in the Coulomb diamonds with respect to $V_G = 0$ reflects the presence of a nonzero background charge. The drain−source threshold voltage required for tunneling of one electron through the device is given by $V_{th} = e/C_\Sigma$ and amounts to about 2.5 meV. From this we estimate a total capacitance $C_\Sigma = C_S + C_D + C_G$ of 64 aF, and a corresponding charging energy $E_C = e^2/2C_\Sigma$ of 1.25 meV. From the absence of any Coulomb staircase in the $I-V$ characteristics, it is evident that the rates with which electrons tunnel through the source and drain junctions are similar; hence $\Gamma_S = \Gamma_D$. The tunnel junctions can be regarded as plate capacitors with $C = \epsilon_r\epsilon_0 A/r$, where A is the area and r is the thickness of the tunnel barrier. Assuming similar capacitances for the source and drain $C = C_D = C_S = 31.6$ aF, $\epsilon_{NiO} = 10.31$, and $r = 1$ nm (estimated), we obtain an effective tunnel junction area of 346 nm^2 corresponding to 30 nm (height) × 11.5 nm (width).

Figure 3 shows a color-coded plot of dI/dV as a function of the drain−source voltage V_d and magnetic field B at $V_G = 0$. The in-plane magnetic field, swept from −0.4 to 0.4 T, was applied parallel to the source−drain electrodes. Evidently, no clear signs of TMR were observed when sweeping the magnetic field. In fact, an almost constant value of dI/dV was observed at the Coulomb blockade threshold voltage (white narrow strip), indicating the absence of spin accumulation. The same results were obtained when applying the magnetic field perpendicular to the source−drain electrodes. We have carried out magnetotransport measurements on four samples, and none of them gave any clear TMR signal. Clearly, some obvious causes for the lack of TMR, such as a poor quality of the magnetic tunneling junctions and poor spin injection efficiency of the Ni leads, can be ruled out from the observed 10% TMR of the test structure discussed above. To estimate the noise level of our device, we have calculated TMR values defined as TMR = $(I_{B_1} - I_{B_2})/I_{B_2}$ as a function of the bias voltage. Here B_1 was chosen to be −0.200 T in order to facilitate parallel magnetization of the electrodes, while different values of B_2 were selected in the interval −50 to 50 mT since the relative magnetization is expected to reverse in this region (see Figure 1B). The data look similar for different B_2 values, and we plot a typical TMR curve for $B_2 = 0$ T in Figure 4.

An estimate of the expected magnetoresistance ratio at large bias is given by the well-known expression TMR = $2(\tau_{RE}|P_1P_2|/e^2\rho\nu(R_S + R_D))$, where ρ is the density of states in the Au disk, ν is the disks' volume, and P_1 and P_2 denote the conduction electron spin polarization of the source and drain electrodes, respectively.[11] In our case the spin polariza-

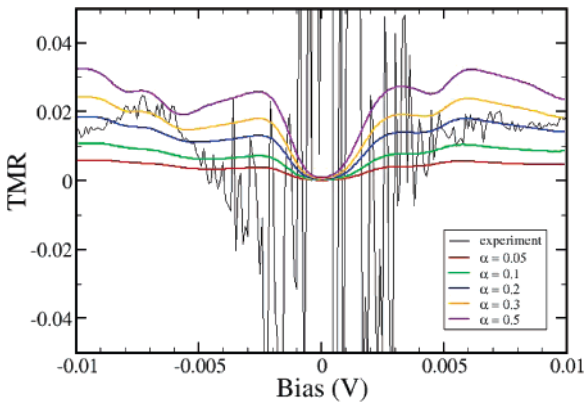

Figure 4. TMR as a function of the drain−source bias at $T = 1.7$ K. The solid curve is the experimentally obtained TMR signal. The other curves are theoretical TMR signals calculated within the orthodox theory for several values of the dimensionless spin relaxation time α.

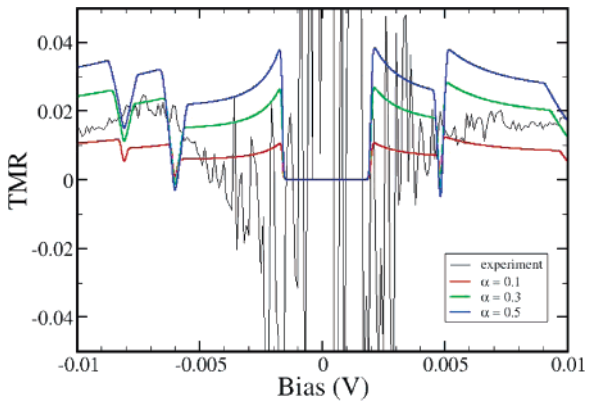

Figure 5. TMR as a function of the drain−source bias. A temperature of 0.1 K was chosen in the simulations. The solid curve is the experimentally obtained TMR signal, recorded at 1.7 K, adopted from Figure 4.

tion of the Ni electrodes is 22%. The denominator $e^2\rho\nu(R_S + R_D)$ can be identified as an effective dwell time τ_{dwell}. The spin-relaxation time τ_{RE}, which is the most crucial parameter of the TMR effect, depends on the island material and can also be considerably affected by the small size of the nanoparticle. In order to get a more accurate quantitative measure of the expected TMR, and its dependence on the bias voltage, we have performed detailed numerical simulations using the rate-equation approach of orthodox Coulomb blockade theory. In dealing with F-SETs with noncollinear configurations, it is often necessary to use a more sophisticated theoretical treatment in the spin transport.[26−29] In our device only the external electrodes are magnetic, and most likely their magnetization is parallel or antiparallel to the external magnetic field. Even in the case in which a certain degree of noncollinearity is present in the device, we believe that its effect is much more subtle than what we are after. It is plausible that a noncollinear configuration can to some extent modulate the TMR as a function of external field, but it will not completely suppress spin accumulation. In the following we thus consider only collinear configurations.

The parameters of the model, namely, tunnel resistances and capacitances, are adjusted to give the best fit of the experimental tunnel current and threshold voltage of the Coulomb blockade region. The capacitances are taken to be $C_S = 24$ aF, $C_D = 20$ aF, and $C_G = 0.8$ aF. The tunnel resistances are both $R_S = R_D = 0.34$ MΩ. We have also introduced an offset charge $Q_0 = -0.25e$ to correctly reproduce the asymmetry of the $I-V$ curve around zero gate bias. In Figure 4 we plot the theoretically predicted TMR at $T = 1.7$ K as a function of the bias voltage for a few values of the dimensionless relaxation time $\alpha = \tau_{RE}/\tau_{dwell}$, which enters the self-consistent equation for the splitting of the Fermi energy and thus controls the spin accumulation on the Au disk. Comparing the experimental and theoretical TMR in Figure 4, it is difficult to say if there is indeed any genuine TMR. The apparent sign change of the noisy experimental TMR at low biases is not reproduced in the simulations at this temperature and for this choice of SET parameters. In fact, from our calculations it is evident that devices with symmetrical tunnel junctions in general exhibit changes in the sign of TMR only at very low temperatures. In Figure 5 we show the calculated TMR at 0.1 K, which is the highest temperature for which negative dips in the TMR are observed outside the Coulomb blockade region. From Figure 4, we furthermore note the presence of an experimental TMR value of about 1−2% at larger bias. This signal could obviously be interpreted as a genuine TMR signal, but it could also simply reflect a spurious charging effect. The discrepancy between the experimental results and numerical simulations hence makes the interpretation of the data in terms of TMR uncertain, leading us to settle with a determination of an upper bound for the spin relaxation time. We note that for $\alpha \approx 0.2$ the value of the theoretical TMR is of the order of 2%, which is approximately equal to the experimental TMR at large bias. With the choice of the tunnel resistances made above and using bulk density of states for Au, we estimate $\tau_{dwell} \approx 20$ ns. Using $\alpha = 0.2$, we obtain an upper bound for τ_{RE} of 4 ns in an Au island with dimensions of a few tens of nanometers, which is several order of magnitudes larger than the spin-relaxation time previously reported in thin Au films.[30] Given the uncertainty in the interpretation of our TMR signal, we emphasize that this estimate is only an upper bound for τ_{RE}. Nevertheless this conclusion is still significant and complementary to other recent magnetotransport measurements on F-SETs with smaller Au nanoparticles, which report a τ_{RE} of the order of 1 ns.[29,31] It should also be noted that our deduced spin-relaxation time is much larger than the spin−orbit scattering time τ_{SO} estimated in Au nanoparticles of comparable size by investigating the individual g-factors of the noninteracting electron states.[32] The time τ_{SO} represents merely an average strength of the spin−orbit interaction and does not correspond to any real relaxation process. The difference between these two times clearly shows that the strong spin−orbit interaction, certainly present in noble metals[33,34] and responsible for a very short τ_{SO} in nanoparticles, is only one variable controlling τ_{RE}. The other crucial element leading to spin relaxation is the coupling of the electron spin to other degrees of freedom of the nanoparticle and the surrounding substrate, such as phonons and magnons. The microscopic mechanisms

of this coupling, and their dependence on the nanoparticle size, are important problems in spintronics which need to be unraveled by further theoretical and experimental studies.

In conclusion, we have studied spin accumulation in a Au nanodisk by performing magnetotransport measurements on a novel type of SET design assembled with an AFM. Ferromagnetic Ni source and drain electrodes are realized using conventional e-beam writing. In the same process we also produce the Ni side-gate electrode. Different widths and lengths of the source and drain electrodes facilitate magnetic reversal of the two electrodes at different magnetic fields. Tunnel barriers of NiO are realized by sequential Ar and O_2 plasma treatment. Using an AFM with specially designed software, a single nonmagnetic Au nanodisk is positioned into the 25 nm gap between the drain and source electrodes. From measurements of spin-polarized transport via the Au nanodisk, we conclude that no clear signatures of TMR are seen, indicating that spin accumulation in the Au island is not occurring due to fast spin relaxation in the Au island. From comparison with results of theoretical modeling we deduce an upper bound of 4 ns for the spin-relaxation time in an Au island with dimensions of a few tens of nanometers. To investigate the switching characteristics and spin-injection efficiency of the Ni electrodes, reference Ni/NiO/Ni tunnel junctions with dimensions of the electrodes similar to those employed in the SETs were fabricated. A maximum 10% TMR was observed from which we deduce a conduction electron spin-polarization of about 22% in the Ni electrodes in good agreement with theory.

Acknowledgment. The authors thank A. Fuhrer and D. Suyatin for help with setting up the experiments and for fruitful discussions. The authors furthermore acknowledge financial support from Halmstad University, the Faculty of Natural Sciences at Kalmar University, the Swedish Research Council under Grant No. 621-2004-4439, the Swedish National Board for Industrial and Technological Development, the Office of Naval Research, and the Swedish Foundation for Strategic Research.

References

(1) *Spin Electronics*; Ziese, M., Thornton M. J., Ed.; Springer: Berlin, Heidelberg, 2001.
(2) *Spin dependent transport in nanostructures*; Maekawa, S., Shinjo, T., Ed.; Taylor, Francis: London, 2002.
(3) Ono, K.; Shimada, H.; Ootuka, Y. *J. Phys. Soc. Jpn.* **1997**, *66*, 1261.
(4) Ono, K.; Shimada, H.; Ootuka, Y. *J. Phys. Soc. Jpn.* **1998**, *67*, 2852.
(5) Yakushiji, K.; et al. *Appl. Phys. Lett.* **2001**, *78*, 515.
(6) Yakushiji, K.; et al. *J. Appl. Phys.* **2002**, *91*, 7038.
(7) Barnas, J.; Fert, A. *Phys. Rev. Lett.* **1998**, *80*, 1058.
(8) Takahashi, S.; Maekawa, S. *Phys. Rev. Lett.* **1998**, *80*, 1758.
(9) Barnas, J.; Fert, A. *Europhys. Lett.* **1998**, *44*, 85.
(10) Brataas, A.; Nazarov, Y. V.; Inoue, J.; Bauer, G. E. W. *Phys. Rev. B* **1999**, *59*, 93.
(11) Korotkov, A. N.; Safarov, V. I. *Phys. Rev. B* **1999**, *59*, 89.
(12) Imamura, H.; Takahashi, S.; Maekawa, S. *Phys. Rev. B* **1999**, *59*, 6017.
(13) Weymann, I.; Barnas, *J. Phys. Status Solidi B* **2003**, *236*, 651.
(14) Chen, C. D.; Watson, K.; Chung, D. S.; Shyu, J. H.; Wu, C. S. *Phys. Rev. Lett.* **2002**, *88*, 047004.
(15) Yakushiji, K.; et al. *Nat. Mater*. **2005**, *4*, 57.
(16) Johansson, J.; Urech, M.; Haviland, D. B.; Korenivski, V. *Phys. Rev. Lett.* **2003**, *91*, 149701. Chen, C. D.; et al. *Phys. Rev. Lett.* **2003**, *91*, 149701.
(17) Khalliulin, G. G.; Khusainov, M. G. *Sov. Phys. JETP* **1988**, *67*, 524.
(18) Mitrikas, G.; Trapalis, C. C.; Kordas, G. *J. Chem. Phys.* **1999**, *111*, 8098.
(19) Jaccard, Y.; Guittienne, Ph.; Kelly, D.; Wegrowe, J-E.; Ansermet, J.-Ph. *Phys. Rev. B* **2000**, *62*, 1141.
(20) Chou, S. Y.; Krauss, P. R.; Kong, L. *J. Appl. Phys*. **1996**, 79, 6101.
(21) OOMMF is Object Oriented Micromagnetic Framework, a micromagnetic simulation code available free from NIST at http://math.nist.gov/oommf/.
(22) Julliere, M. *Phys. Lett. A* **1975**, *54*, 225.
(23) Meservey, R.; Tedrow, P. M. *Phys. Rep*. **1994**, *238*, 173.
(24) Junno, T.; Carlsson, S.-B.; Xu, H.; Montelius, L.; Samuelson, L. *Appl. Phys. Lett*. **1998**, *72*, 548.
(25) Liu, R. S.; Suyatin, D.; Pettersson, H.; Samuelson, L. Submitted to *Nanotechnology*.
(26) König, J.; Martinek, J. *Phys. Rev. Lett*. **2003**, *90*, 166602.
(27) Braun, M.; König, J.; Martinek, J.; et al. *Phys. Rev. B* **2004**, *70*, 195345.
(28) Braig, S.; Brouwer, P. W. *Phys. Rev. B.* **2005**, *71*, 195324.
(29) Wetzels, W.; Bauer, G. E. W.; Grifoni, M. *Phys. Rev. B.* **2005**, *72*, 020407.
(30) Elezzabi, A. Y.; Freeman, M. R.; Johnson, M. *Phys. Rev. Lett*. **1996**, *77*, 3220.
(31) Bernand-Mantel, A.; Seneor, P.; Lidgi, N.; Calvet, L.; Cros, V.; Bouzehouane, K.; Fusil, S.; Deranlot, C.; Vaures, A.; Petroff, F.; Fert, A. Spin dependent Coulomb Blockade in metallic nanoclusters. Poster presented at the conference: Spin-dependent transport through nanostructures—Spintronics '05, Poznan, September 2005.
(32) Petta, J. R.; Ralph, D. C. *Phys. Rev. Lett*. **2001**, 87, 266801.
(33) Yafet, Y. *Phys. Rev.* **1952**, *85*, 478.
(34) Elliott, R. *J. Phys. Rev.* **1954**, *96*, 266.

NL062146N

Paper V

Large magnetoresistance in Co/Ni/Co ferromagnetic single electron transistors

R. S. Liu and H. Pettersson[a)]
Center for Applied Mathematics and Physics, Halmstad University, Box 823, SE-301 18 Halmstad, Sweden

L. Michalak and C. M. Canali
Division of Physics, Department of Natural Sciences, Kalmar University, 391 82 Kalmar, Sweden

D. Suyatin and L. Samuelson
Solid State Physics/The Nanometer Structure Consortium, Lund University, Box 118, SE-22100 Lund, Sweden

(Received 20 December 2006; accepted 9 February 2007; published online 22 March 2007)

The authors report on magnetotransport investigations of nanoscaled ferromagnetic Co/Ni/Co single electron transistors. As a result of reduced size, the devices exhibit single electron transistor characteristics at 4.2 K. Magnetotransport measurements carried out at 1.8 K reveal tunneling magnetoresistance (TMR) traces with negative coercive fields, which the authors interpret in terms of a switching mechanism driven by the shape anisotropy of the central wirelike Ni island. A large TMR of about 18% is observed within a finite source-drain bias regime. The TMR decreases rapidly with increasing bias, which the authors tentatively attribute to excitation of magnons in the central island. © *2007 American Institute of Physics*. [DOI: 10.1063/1.2714289]

The tunneling magnetoresistance (TMR) observed in spintronic devices is usually defined as $\mathrm{TMR}=(R_{\mathrm{AP}}-R_{\mathrm{P}})/R_{\mathrm{P}}$, where R_A and R_{AP} are the device resistances in the parallel and antiparallel magnetization configurations, respectively. TMR has been extensively investigated both experimentally and theoretically because of promising applications, e.g., magnetic random access memories and read/write heads in hard disks as well as in various other spintronic devices.[1] More recently, a lot of research has focused on the dependence of TMR on the interplay between spin-dependent tunneling and the Coulomb blockade effect[2] in ferromagnetic single electron transistors (F-SETs).[3] Theoretical investigations of F-SETs predict exciting magnetoresistance properties connected to spin accumulation on the central island.[4–10] Indeed, several experiments on F-SETs, starting with the seminal work by Ono *et al.*, have demonstrated enhanced TMR and magneto-Coulomb oscillations of the TMR as a function of external magnetic field and bias voltage.[11,12] However, due to the relatively large size of their devices, a sample temperature in the range of tens of milliKelvins was required in order to observe any significant TMR signals. For future spintronic applications, it is obviously important to realize F-SETs with a considerably higher operating temperature.

In this letter, we present magnetotransport investigations of nanoscaled Co/Ni/Co F-SETs exhibiting single electron transistor characteristics at 4.2 K. The fabrication yield of the device is about 50%. The devices are fabricated on top of a 100 nm thick SiO_2 layer, thermally grown on a Si substrate (shown in Fig. 1). The wirelike Ni islands measure 150 nm in length, 20 nm in width, and 25 nm in thickness. The islands are prepared together with Ni side gates in one step employing electron-beam lithography, followed by thermal evaporation and lift-off. Tunnel barriers of NiO are subsequently formed by O_2 plasma etching at a pressure of about 5 mbars for 1 min. Ferromagnetic Co source and drain electrodes, 40 nm thick, are defined on top of the Ni islands using a high-precision alignment procedure during a second electron-beam lithography step. The area of the tunnel junctions amounts to only about 40×20 nm^2. The source electrode has a length of 1.5 μm and a width of 80 nm. The corresponding dimensions of the drain electrode are 800 and 280 nm, respectively. The separation between the parallel drain and source electrodes is approximately 55 nm. Because of shape anisotropy, the two electrodes are expected to undergo magnetic reversal at different magnetic fields.[13] After the fabrication, conductance measurements are carried out at 4.2 K in a liquid helium Dewar. The schematic circuit diagram is shown in Fig. 1(c). Following these measurements, the sample is transferred to a cryostat housing a 6 T superconducting magnet, where magnetoresistance measurements are carried out at 1.8 K. The magnetic field is in the plane of the device with a tunable orientation with respect to the orientation of the electrodes.

Figure 2 shows a typical nonlinear current-voltage (I-V) curve for the device at 4.2 K. From the absence of a Coulomb staircase in the I-V curve, we conclude that the device has two symmetric tunneling junctions with the same electron tunneling rates. The modulation of the current with gate

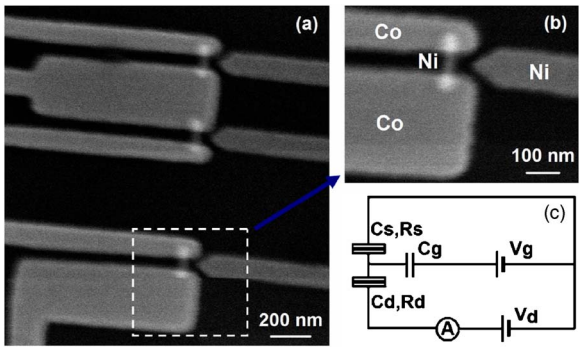

FIG. 1. (a) Top-view SEM image of the device geometry. (b) Expanded view of an isolated F-SET marked by a white short-dashed rectangle in (a). The Ni island has dimensions of 150 nm (length)$\times$20 nm (width) $\times$25 nm (thickness). (c) Circuit diagram of the connected device.

[a)]Author to whom correspondence should be addressed. Electronic mail: hakan.pettersson@ide.hh.se

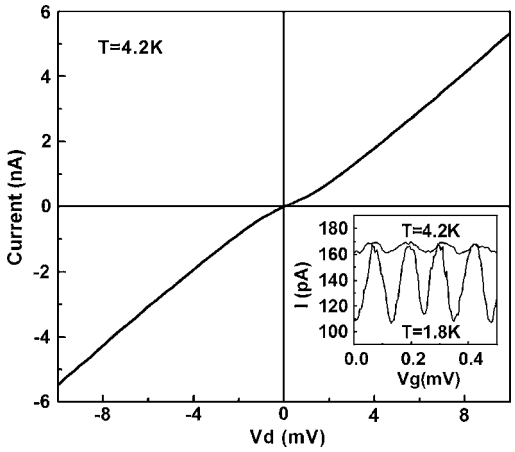

FIG. 2. Nonlinear current-voltage (I-V) characteristics at 4.2 K recorded at zero magnetic field with gate voltage V_g=0 V. Lower right inset: Gate modulated current curves at 4.2 K (upper) and 1.8 K (lower), respectively, at an applied drain-source bias of 0.4 mV.

bias is shown in the inset at 4.2 and 1.8 K, respectively, at a drain-source bias of 0.4 mV. Here each peak corresponds to addition of one electron to the island. The gate modulation of the current was visible up to a drain-source threshold voltage of about 2 mV at 1.8 K, from which we deduce a charging energy $E_C=e^2/2C_\Sigma$ of about 1 meV.

Figure 3 shows the dependence of the resistance on the magnetic field for two sweep directions. The measurements were performed at 1.8 K with an in-plane magnetic field applied parallel to the long axis of the electrodes. From this figure two obvious interesting results are readily observed: Firstly, as the magnetic field is swept from −1.5 to 1.5 T, a substantial TMR is observed with a largest magnitude reaching ~13% between −0.15 and 0.5 T. Secondly, the TMR trace displays negative coercive fields for the two sweep directions. The origin of this phenomenon can be attributed to the special design of our device. Since the central Ni island has a wirelike shape, a substantial shape anisotropy is expected, which favors a magnetic moment in the direction of the island (wire). This leads to noncollinear configurations and switching mechanisms for certain values of the external magnetic field. To explicitly clarify this point, we have performed micromagnetic modeling of the magnetization configurations of the device using the OOMMF code,[14] in conjunction with rate-equation simulations of the quantum transport with noncollinear magnetization vectors of the external leads and the central island. The quantum transport simulations, shown in Fig. 3, are an extension of the usual sequential tunneling calculations for a collinear F-SET in the spirit of Ref. 8. All the relevant magnetization configurations of the device used in the transport calculations, and the values of the external magnetic field at which transitions between two configurations occur, are obtained from micromagnetic simulations. At large negative external magnetic fields, the electrodes and the central Ni island (wire) are all magnetized along the field and no TMR is observed. At −0.1 T, the magnetic moment of the Ni island spontaneously relaxes to its easy magnetization axis and thus becomes perpendicular to the magnetic moments of the Co electrodes, resulting in a theoretical TMR of 8%. As the magnetic field goes through zero and subsequently increases, the two Co leads reverse their magnetization directions in a conventional manner at 0.13 T (wide one) and 0.21 T (narrow one), respectively, together with a progressive flip of the magnetization in the central Ni island. The theoretical value differs by a factor of ~2 from the experimentally observed TMR, which is acceptable in consideration of complex magnetization effects not included in our theoretical model. At 0.3 T, the shape anisotropy of the Ni island is completely overcome by the external field and all magnetic moments are aligned parallel to the external field, resulting in minimum resistance. The magnetization configurations and corresponding resistance changes are expected to occur in an analogous manner when decreasing the magnetic field from large positive values. From Fig. 3 it is evident that there is a shift of the experimental TMR curves towards positive magnetic field, especially for the reverse sweeping curve (red one), which could be due to an exchange bias caused by the antiferromagnetic oxides on top of both the Ni island and the Co electrodes.[15]

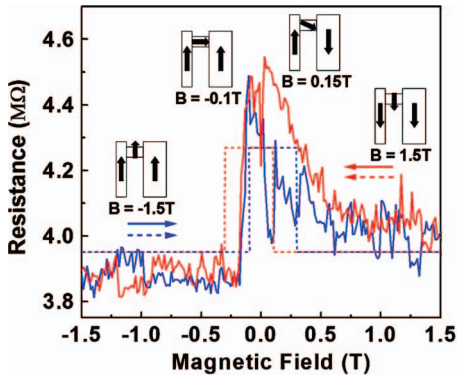

FIG. 3. (Color) Dependence of the resistance on the magnetic field at 1.8 K with an applied drain-source bias of 1.5 mV. The solid and dotted curves are experimental data and simulation results, respectively. The magnetic field sweep directions are denoted with horizontal arrows in different colors. The insets show schematic magnetization configurations of the device obtained from micromagnetic modeling, sweeping the magnetic field from −1.5 to +1.5 T.

Figure 4(a) shows the current-voltage (I-V) characteristics measured at T=1.8 K at B=0 T (black curve) and B=−1.5 T (red curve), respectively. In Fig. 4(b), we plot the TMR, normalized by its maximum, as a function of the drain-source bias voltage (blue curve). The TMR is derived from the two I-V curves in (a) according to TMR=$(I_{-1.5\ \mathrm{T}}-I_{0\ \mathrm{T}})/I_{0\ \mathrm{T}}$. Interestingly, the maximum TMR reaches 18% within the Coulomb blockade regime and decreases rapidly as the drain-source bias increases above E_C. This abrupt decrease of TMR is not reproduced in our numerical simulations in the sequential tunneling regime, even after taking into account the decrease of spin asymmetry of the tunneling electrons for energies larger than the Fermi energy (in the simulations we assume that the spin polarization of both external electrodes and central island decays exponentially for energies larger than their corresponding Fermi energy in units of E_C), as shown by the purple curve of Fig. 4(b). Such a dependence is meant to account, in a simplified way, for the bias dependence of the density of states (DOS), which is known to influence the TMR.[16,17] Modeling microscopically this effect is very difficult, particularly since the electrodes are thermally grown, which leaves no control over the crystal structure. Nevertheless, comparing our experimental results to those of Ref. 17, we note that the bias dependence of the TMR is much stronger in our case, and we therefore hesitate to primarily attribute our results to a bias-dependent DOS. The influence of the applied electric field (bias) on the tun-

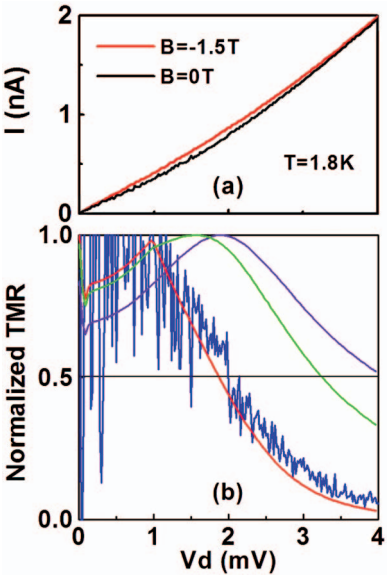

FIG. 4. (Color) (a) Current-voltage characteristics measured at 1.8 K at $B=0$ T (black curve) and $B=-1.5$ T (red curve), respectively. (b) The dependence of TMR$=(I_{B=-1.5\ \mathrm{T}}-I_{B=0\ \mathrm{T}})/I_{B=0\ \mathrm{T}}$, normalized by its maximum value, on drain-source voltage. The current values are taken from the two *I-V* curves in (a). The red, green, and purple solid curves are the results of numerical simulations in which the spin polarization $P(V)$ of the central island is assumed to decay exponentially for biases larger than the Coulomb blockade gap according to the expression $P(V)=P_0e^{[(E_C-eV)/\gamma E_C]}$. The three curves correspond to $\gamma=1,5,\infty$ (no decay), respectively.

neling barrier height does not explain the abrupt decrease either.[18,19] Cotunneling[5] can also be ruled out since it would result in rather a gentle decrease of the TMR with increasing bias for the relatively large ratio $k_BT/E_C\approx 0.15$ given in our case. Higher order tunneling processes can furthermore be excluded, since the tunneling resistances of the investigated junctions (≈ 1 MΩ) are much larger than the quantum resistance (≈ 26 kΩ).[20]

A more likely mechanism for the decrease in TMR with increasing bias is the excitation of spin waves or *magnons* by the spin-polarized tunneling current.[21–23] In our devices, electron spin injection orthogonal to the magnetization of the island can exert a torque acting like a transverse magnetic field which creates magnons. If many magnons are present, the island magnetization can be considerably disrupted, which results in a decrease of the magnetoresistance. The excitation of magnons is an inelastic process, whose energy is provided by the bias. The dispersion of low-energy spin waves in a ferromagnet is given by $\omega(q)=\Delta+D|\mathbf{q}|^2$, where D is the spin-wave stiffness constant which is of the order of 500 meV in Ni.[24] The energy gap Δ is proportional to the magnetic anisotropy of the system, including shape anisotropy, and amounts to a small fraction of 1 meV. The allowed wave vectors in our small islands are discrete and can be written as $q_n=2\pi n/L$, $n=0,1,2\ldots$, where L is the size of the island. From this we estimate that some of the lowest modes can, in principle, be present already at small biases where the F-SET is in the Coulomb blockade regime. However, their excitation is not very efficient because the current in the off state is small. In contrast, the current is finite in the on state, and for larger biases short wavelength magnons can be excited. A full microscopic implementation of this effect in transport is beyond the purpose of the present letter. Here we consider a phenomenological model in which the creation of spin waves causes an exponential decrease of the spin polarization of the island for biases above the Coulomb blockade gap. The effect of such a dependence on the normalized TMR is shown by the red curve in Fig. 4(b), which seems to capture the drastic decrease of TMR with increasing bias. This scenario would also explain the persistence of TMR for biases above the Coulomb blockade gap observed in other F-SET experiments,[25] where a smaller size of the grains and considerably larger tunneling resistances make the excitation of spin waves both more energetically costly and less efficient.

In summary, we have fabricated Co/Ni/Co F-SETs exhibiting single electron transistor characteristics at 4.2 K. Magnetotransport measurements at 1.8 K reveal TMR traces with negative coercive fields, which we interpret in terms of a switching mechanism driven by shape anisotropy in the central wirelike Ni island. A large TMR signal of a maximum magnitude of 18% has been observed within a small drain-source bias regime. The TMR decreases rapidly with increasing bias, which we tentatively attribute to an excitation of magnons in the central island.

The authors thank Arne Brataas and Allan MacDonald for fruitful discussions. The authors furthermore acknowledge financial support from Halmstad University, the Faculty of Natural Sciences at Kalmar University, the Swedish Research Council under Grant No. 621-2004-4439, the Swedish National Board for Industrial and Technological Development, the Office of Naval Research, and the Swedish Foundation for Strategic Research.

[1] *Spin Electronics*, edited by M. Ziese and M. J. Thornton (Springer, Berlin, 2001).
[2] *Single Charge Tunneling*, NATO Advanced Studies Institute B: Physics Series, Vol. 294, edited by H. Grabert and M. H. Devoret (Plenum, New York, 1992).
[3] *Spin Dependent Transport in Magnetic Nanostructures*, edited by S. Maekawa and T. Shinjo (Taylor & Francis, London, 2002).
[4] J. Barnas and A. Fert, Phys. Rev. Lett. **80**, 1058 (1998).
[5] S. Takahashi and S. Maekawa, Phys. Rev. Lett. **80**, 1758 (1998).
[6] J. Barnas and A. Fert, Europhys. Lett. **44**, 85 (1998).
[7] A. Brataas, Y. V. Nazarov, J. Inoue, and G. E. W. Bauer, Phys. Rev. B **59**, 93 (1999).
[8] A. N. Korotkov and V. I. Safarov, Phys. Rev. B **59**, 89 (1999).
[9] H. Imamura, S. Takahashi, and S. Maekawa, Phys. Rev. B **59**, 6017 (1999).
[10] I. Weymann and J. Barnas, Phys. Status Solidi B **236**, 651 (2003).
[11] K. Ono, H. Shimada, and Y. Ootuka, J. Phys. Soc. Jpn. **66**, 1261 (1997).
[12] K. Ono, H. Shimada, and Y. Ootuka, J. Phys. Soc. Jpn. **67**, 2852 (1998).
[13] S. Y. Chou, P. R. Krauss, and L. Kong, J. Appl. Phys. **79**, 6101 (1996).
[14] OOMMF (Object Oriented Micromagnetic Framework), a micromagnetic simulation code, NIST, http://math.nist.gov/oommf/
[15] For a review on exchange bias, see J. Nogues and I. K. Schuller, J. Magn. Magn. Mater. **192**, 203 (1999); A. E. Berkowitz and K. Takano, J. Magn. Magn. Mater. **200**, 552 (1999).
[16] P. LeClair, J. T. Kohlhepp, C. H. van de Vin, H. Wieldraaijer, H. J. M. Swagten, W. J. M. de Jonge, A. H. Davis, J. M. MacLaren, J. S. Moodera, and R. Jansen, Phys. Rev. Lett. **88**, 107201 (2002).
[17] X. H. Xiang, T. Zhu, J. Du, G. Landry, and J. Q. Xiao, Phys. Rev. B **66**, 174407 (2002).
[18] X. Zhang, B.-Z. Li, G. Sun, and F.-C. Pu, Phys. Rev. B **56**, 5484 (1997).
[19] A. M. Bratkovsky, Phys. Rev. B **56**, 2344 (1997).
[20] X. H. Wang and A. Brataas, Phys. Rev. Lett. **83**, 5138 (1999).
[21] L. Berger, Phys. Rev. B **54**, 9353 (1996).
[22] J. C. Slonczewski, J. Magn. Magn. Mater. **159**, L1 (1996).
[23] S. I. Kiselv, J. C. Sankey, I. N. Krivorotov, N. C. Emley, A. G. F. Garcia, R. A. Burhman, and D. C. Ralph, Phys. Rev. B **72**, 064430 (2005).
[24] J. Kubler, *The Theory of Itinerant Electron Magnetism* (Oxford University Press, Oxford, 2000).
[25] K. Yakushiji, F. Ernult, H. Imamura, K. Yamane, S. Mitani, K. Takanashi, S. Takahashi, S. Maekawa, and H. Fujimori, Nat. Mater. **4**, 57 (2005).